The Journal of Physiology

A detailed mathematical model of the human atrial cardiomyocyte: integration of electrophysiology and cardiomechanics

Fazeelat Mazhar[1], Chiara Bartolucci[1], Francesco Regazzoni[2], Michelangelo Paci[1,3], Luca Dedè[2], Alfio Quarteroni[2,4], Cristiana Corsi[1] and Stefano Severi[1]

[1]*Department of Electrical, Electronic and Information Engineering 'Guglielmo Marconi', University of Bologna, Cesena, Italy*
[2]*MOX - Dipartimento di Matematica, Politecnico di Milano, Milan, Italy*
[3]*BioMediTech, Faculty of Medicine and Health Technology, Tampere University, Tampere, Finland*
[4]*Mathematics Institute, École Polytechnique Fédérale de Lausanne, Lausanne, Switzerland*

Handling Editors: Natalia Trayanova & T. Alexander Quinn

The peer review history is available in the Supporting Information section of this article (https://doi.org/10.1113/JP283974#support-information-section).

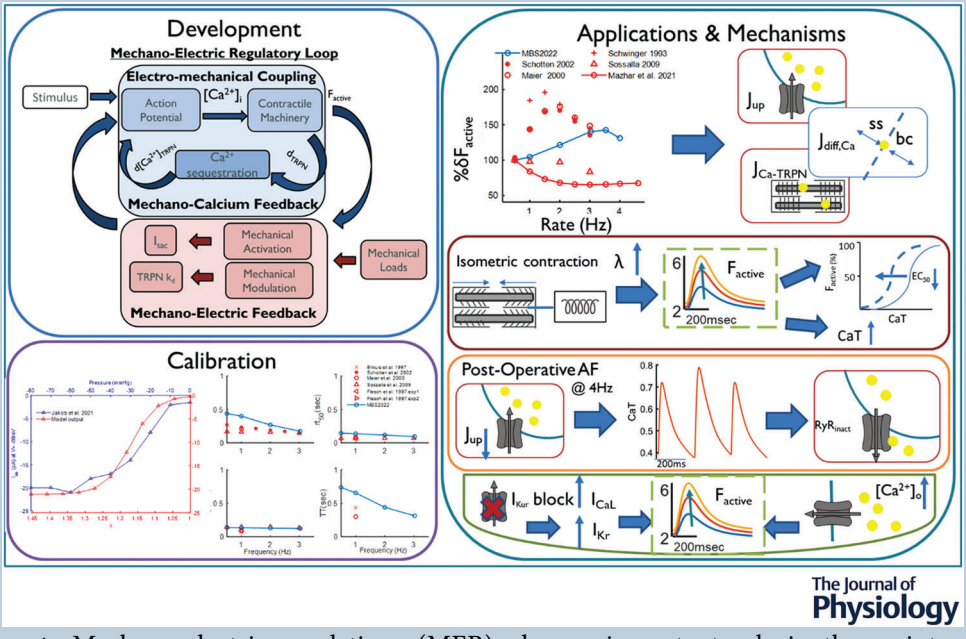

Abstract Mechano-electric regulations (MER) play an important role in the maintenance of cardiac performance. Mechano-calcium and mechano-electric feedback (MCF and MEF) pathways adjust the cardiomyocyte contractile force according to mechanical perturbations and affects electro-mechanical coupling. MER integrates all these regulations in one unit resulting in a complex

Fazeelat Mazhar has recently completed a PhD in biomedical engineering at University of Bologna, Italy. During her PhD, Fazeelat has worked on investigating, modelling, and coupling of electrophysiological and contraction related mechanisms under physiological and pathological conditions with focus on human atria. She is currently working as a Post-doctorate researcher in the same institute.

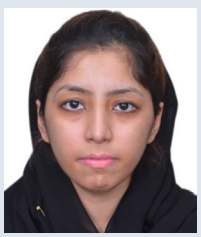

DOI: 10.1113/JP283974

phenomenon. Computational modelling is a useful tool to accelerate the mechanistic understanding of complex experimental phenomena. We have developed a novel model that integrates the MER loop for human atrial cardiomyocytes with proper consideration of feedforward and feedback pathways. The model couples a modified version of the action potential (AP) Koivumäki model with the contraction model by Quarteroni group. The model simulates iso-sarcometric and isometric twitches and the feedback effects on AP and Ca^{2+}-handling. The model showed a biphasic response of Ca^{2+} transient (CaT) peak to increasing pacing rates and highlights the possible mechanisms involved. The model has shown a shift of the threshold for AP and CaT alternans from 4.6 to 4 Hz under post-operative atrial fibrillation, induced by depressed SERCA activity. The alternans incidence was dependent on a chain of mechanisms including RyRs availability time, MCF coupling, CaMKII phosphorylation, and the stretch levels. As a result, the model predicted a 10% slowdown of conduction velocity for a 20% stretch, suggesting a role of stretch in creation of substrate formation for atrial fibrillation. Overall, we conclude that the developed model provides a physiological CaT followed by a physiological twitch. This model can open pathways for the future studies of human atrial electromechanics.

(Received 19 October 2022; accepted after revision 2 August 2023; first published online 24 August 2023)
Corresponding author S. Severi: Department of Electrical, Electronic and Information Engineering 'Guglielmo Marconi', University of Bologna, Cesena, Italy. Email: stefano.severi@unibo.it

Abstract figure legend Three phases of novel human atrial electromechanically coupled model, MBS2023. Phase 1 deals with model development, the conceptual background, and the coupling of forward and backward pathways. Phase 2 is based on calibration of parameters related to contraction, stretch activated channels, and Ca^{2+} handling. Phase 3 is about the testing and validation of the model based on applications like rate adaptation, isometric contraction, the post-operative atrial fibrillation (PoAF) condition, I_{Kur} block, and extracellular Ca^{2+} variations.

Key points

- With the availability of human atrial cellular data, interest in atrial-specific model integration has been enhanced.
- We have developed a detailed mathematical model of human atrial cardiomyocytes including the mechano-electric regulatory loop. The model has gone through calibration and evaluation phases against a wide collection of available human *in-vitro* data.
- The usefulness of the model for analysing clinical problems has been preliminaryly tested by simulating the increased incidence of Ca^{2+} transient and action potential alternans at high rates in post-operative atrial fibrillation condition.
- The model determines the possible role of mechano-electric feedback in alternans incidence, which can increase vulnerability to atrial arrhythmias by varying stretch levels.
- We found that our physiologically accurate description of Ca^{2+} handling can reproduce many experimental phenomena and can help to gain insights into the underlying pathophysiological mechanisms.

Introduction

At each heartbeat, dynamic changes in the heart activity, induced by the mechanical load, are intrinsically regulated (via Frank Starling and Anrep effects) to maintain the cardiac output. Likewise, at the cellular level these mechanical changes regulate the electrical activity (Peyronnet et al., 2016, Quinn & Kohl, 2021) and the Ca^{2+} handling (Calaghan et al., 1999, Neves et al., 2016) under both physiological and pathological conditions (Pfeiffer et al., 2014; Ravens, 2003; Taggart & Sutton, 1999; Varela et al., 2021). The strong coupling of electrophysiology and cardiomechanics within the cardiomyocytes (CMs) is called electro-mechanical coupling (EM). Figure 1 shows the feedforward and feedback pathways that connect together to form the mechano-electric regulatory (MER) loop. Within the loop, the dynamic response of Ca^{2+} sequestration by troponin (TRPN) on the electrophysiology is referred to as the mechano-calcium feedback (MCF) (Rice et al., 1999). The changing contractile force affects the action potential (AP) via mechano-electric

feedback (MEF) (Nazir et al., 1996; reviewed in Kohl et al., 2001).

EM coupling is a series of events triggered by membrane depolarization and the development of the AP, followed by Ca^{2+} release from the sarcoplasmic reticulum (SR) via the Ca^{2+}-induced-Ca^{2+}-release (CICR) mechanism. The Ca^{2+} release is responsible for initiating the CM contraction by the activation of thin filaments, i.e. the regulatory units (RUs) followed by the cooperativity of RU proteins, and eventually leading to cross-bridge cycling (XB_{cy}). This regulation hence depicts a complex phenomenon, making it challenging to understand and to quantify the role of individual components at the system level. The development of a sophisticated cardiac mathematical model can help to provide a better insight into these complex experimental phenomena (Vagos et al., 2018).

Several atrial computational models have been developed to improve the understanding of individual components of the EM coupling: the electrophysiology (reviewed in Heijman et al., 2021 and Wilhelms et al., 2013) and the Ca^{2+} handling (reviewed in Sutanto et al., 2020). However, in the literature, the focus of cardio-mechanics studies (reviewed in Niederer et al., 2019; Regazzoni et al., 2021) and models (reviewed in Lee et al., 2022; Trayanova et al., 2011; Varela et al., 2021) has been more on ventricular CMs (reviewed in Sutanto & Heijman, 2022). Similarly, MER integrated models were developed and were based either on ventricular electro-mechanics (Timmerman et al., 2017; Margara et al., 2021; Bartolucci et al., 2022) or on stem cell derived CMs (Forouzandehmehr et al., 2021). With the availability of human atrial cellular data, interest in atrial specific MER modelling has increased. The very first attempt to study the influence of human atrial mechanics during atrial fibrillation (AF) on the whole heart model was made by Land (Land et al., 2018). However, not every contraction parameter was re-tuned according to human atrial physiological contraction data. Relatively few atrial cellular MER integrated models have been developed; for instance, the integrated model by Zhan (Zhan et al., 2013; Zhan et al., 2019) is more focused on the impact of fibroblast on coupling and contraction. Another EM model was developed by Kuijpers (Kuijpers et al., 2007) and later by Brocklehurst (Brocklehurst et al., 2015); however, its cell level mechanisms were not validated quantitatively against any human atrial *in-vitro* data. Importantly, all the integrated models used the same human atrial AP model, i.e. the Courtemanche (CRN) model (Courtemanche et al., 1998).

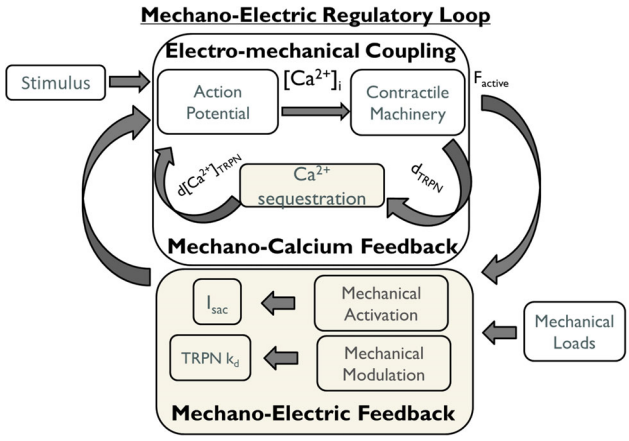

Figure 1. Mechano-electric regulatory loop along with feedforward (electro-mechanical coupling) and feedback (mechano-calcium and mechano-electric) pathways
The application of action potential produces a Ca^{2+} transient $[Ca^{2+}]_i$ that is fed as an input to the contractile machinery. The active force (F_{active}) generates a dynamic effect of troponin buffer (d_{TRPN}) and triggers the mechano-calcium feedback by the sequestration of $[Ca^{2+}]_i$ ($d[Ca^{2+}]_{TRPN}$). The varying mechanical length/loads induces change in mechanical activity either by mechanically activated channels (MACs) in the form of stretch activated current (I_{sac}) or mechanically modulated channels (MMCs) via the k_d factor of troponin, Ca^{2+} cytosolic buffer and is feedback to AP and Ca^{2+} handling by MEF pathway. [Colour figure can be viewed at wileyonlinelibrary.com]

Following the current MER modeling approach, in one of our previous studies (Mazhar et al., 2021), we developed an integrated model of human atrial CM by coupling the Courtemanche AP model and the contraction model developed by the Quarteroni group, the RDQ2020 model (Regazzoni et al., 2020). However, this coupled and calibrated model was not able to reproduce one important phenomenon: the force-frequency relationship for human atrial CMs. The reason for this discrepancy was identified as the Ca^{2+} -transient rate adaptation trend, which in turn probably depends on the atrial specific physiological phenomena of CICR propagation, from the membrane to the centre of the CM in a Ca^{2+} wave-like fashion by a 'fire-diffuse-fire-mechanism' (Blatter, 2017; Bootman et al., 2006). Hence, there is a need to have a model with calibrated Ca^{2+} handling dynamics that remains valid upon rate changes.

We aimed to develop a human atrial cellular model with MER integration that is computationally efficient and exhibits a detailed temporal Ca^{2+} handling description, valid over a physiological range of pacing rates. In addition, to our knowledge, this is the first human atrial model that includes the MER loop and is calibrated against a wide collection of available human *in-vitro* atrial data. The model was designed to present coupling and mechanical load effects on electrophysiology, on Ca^{2+} transient (CaT), and on the active force (F_{active}). In this way, it can be used to determine the possible role of feedbacks MCF and MEF in the initiation of atrial arrhythmias by varying stretch levels. The clinical utility of the model has been preliminaryly tested by simulating the increased incidence of CaT and AP alternans at high rates in post-operative atrial fibrillation (PoAF) conditions. Our model is named *Mazhar-Bartolucci-Severi 2023* (MBS2023).

Methods

With respect to the MER loop formation between AP and contraction modules, we identified as the components of the coupling a feedforwad and a feedback pathway. The former is the input of CaT to the contraction module, the latter is the sequestration of Ca^{2+} bound to troponin (MCF) from the free cytosolic Ca^{2+}. In this way, a strong bidirectional coupling was ensured in the MBS2023 model. The section 'Electro-mechanical coupling and mechano-calcium feedback' highlights this stepwise approach for introducing coupling and the MCF effect in the model. Moreover, the calibration of contraction and Ca^{2+} handling parameters was carried out to obtain a model in agreement with human atrial *in-vitro* data (references in Tables A2 and A3). MBS2023 is simulated in two operating modes: (1) iso-sarcometric, where the sarcomere length (SL) was fixed as is usually found *in-vitro* experiments, and (2) isometric, where for a given SL the preload effect was varied using the stretch ratio (λ). The model was switched to isometric operating mode in order to simulate the stretch-induced MEF response and also to determine its role in alternans vulnerability.

Cell structure of the model

In MBS2023, the bidirectional coupling was achieved with two modules: the AP module obtained from a considerable revision of the human atrial cell model Koivumäki 2011 (Koivumäki et al., 2011), KM2011; and a mean-field approximation-based contraction module, RDQ2020 (Regazzoni et al., 2020). The aim of the MBS2023 model was to combine the complex Ca^{2+} handling dynamics of atria (Blatter et al., 2003; Bootman et al., 2011; Hüser et al., 1996; Hatem et al., 1997) with a computationally efficient modelling approach for human atrial CM. Based on the KM2011 AP model, we reduced the multi-compartmental structure of cytosol and SR in KM2011 and we were left with two compartments only, i.e. the sub-space (ss) and the bulk cytosol (bc). A schematic representation of the updated compartmental organization of our model is shown in Fig. 2.

The cell dimensions for the parent AP model KM2011 were adopted from Nygren (Nygren et al., 1998). In comparison to the human atrial cell dimensions (Neef et al., 2010; $n = 115$), the model cell length was slightly longer (122.051 μm *vs.* 101.15 $\pm$ 1.5 μm) and the radius was shorter (6.5 μm *vs.* 7.4 $\pm$ 0.3 μm). The total cell capacitance (50 pF) seems to be lying near the lower bound of values reported in human atrial experiments (see Table A1). Interestingly, we found a very large variability in such data, ranging from 29.6 $\pm$ 1.8 pF, as reported by the Nattel lab (Wang et al., 1999) up to 114.8 $\pm$ 5.9 pF reported by Voigt et al. (Voigt et al., 2012). This variability in cell capacitance can be associated with the T-tubule density present in the cell, which affects the capacitance-to-longitudinal surface area (C/A), reported to range from 1% to 10% in human atrial cells ($n = 50$, Fakuade et al., 2021). The dimensions for the MBS2023 cell model were modified in accordance with the experimental values (Neef et al., 2010). Since there was a 12% increase in radius, with respect to KM2011, we made a similar increase in the capacitance, up to 56 pF. The low C/A ratio ($\cong$ 1%) implies an assumption of a low T-tubule density.

The cytosolic space was re-arranged in such a way that the ss compartment was at a distance of 0.02 μm from the membrane (as in KM2011) and the rest of the area in the bulk/centre was summed to form the *bc* compartment

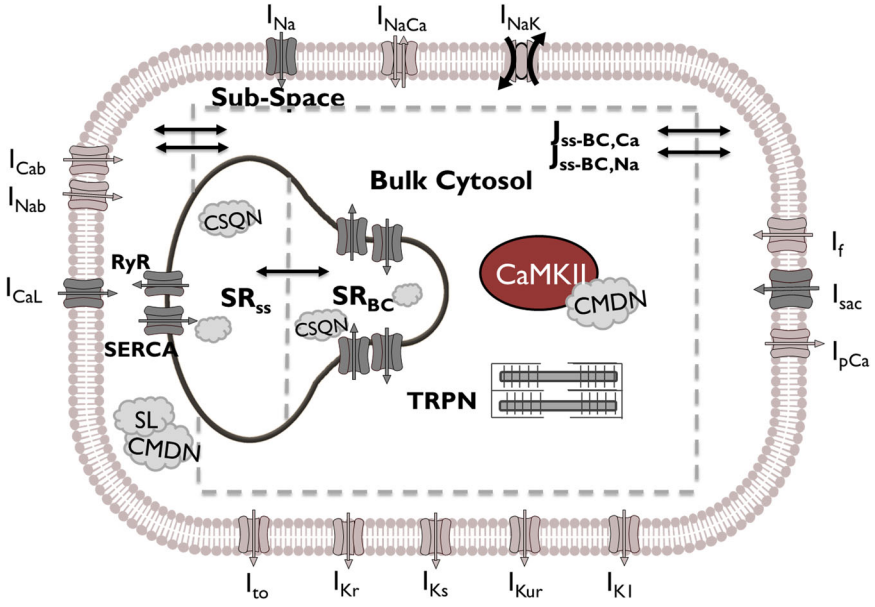

Figure 2. Schematic diagram of human atrial myocyte model
The figure shows two cytosolic compartments, the subspace (ss) and bulk cytosol (bc). The *bc* compartment is enclosed inside a grey dashed line box. The sarcoplasmic reticulum (SR) also includes two compartments SR_{ss} and SR_{bc} with their own release (RyR) and uptake (SERCA) units. The cytosolic buffers are troponin (TRPN), calmodulin (CMDN), and sarcolemmal phospholipids (SL). The sarcolemmal currents and fluxes in dark grey are modified/ reformulated/added in our novel model MBS2023. [Colour figure can be viewed at wileyonlinelibrary.com]

so that the *bc* compartment was located at a distance of 6.6 μm from the ss. In this way, the *bc* compartment volume (V_{bc}) was 163 times larger than the volume of ss compartment (V_{ss}). Similarly, SR was divided into two compartments, i.e. SR_{ss} lying near the membrane and SR_{bc} more towards the centre, each having its own release RyR and uptake SERCA units. The total volume of SR was kept the same as in KM2011 whereas the volume dedicated to ss (V_{SRss}) and *bc* (V_{SRbc}) was redefined. V_{SRbc} was then formed from $\frac{3}{4}$ of the cytosolic *bc* compartment and V_{SRss} was the sum of cytosolic subspace volume V_{ss} and $\frac{1}{4}$ of bc. Hence, the V_{SRbc} was 1.26 times larger than V_{SRss}. In this way, the contribution of Ca^{2+} storage in SR_{ss} was enhanced towards the formation of global cytosolic CaTs.

The diffusion of Ca^{2+} and Na^{+} in the cytosolic compartments is also shown in Fig. 2. In addition, all of the intracellular electrolyte concentrations were dynamic except $[K^{+}]_i$ which was fixed at 134 mM since it was necessary to have a steady-state stable value for the electrolyte concentrations (Barral et al., 2022).

Ca^{2+} in the cytosol

In KM2011, cytosolic Ca^{2+} diffusion from the ss to bc region was an analytical diffusion equation and the diffusion distance $x_{ss\text{-}bc}$ was from the centre of ss to the centre of the first bc compartment. Using the same definition of $x_{ss\text{-}bc}$ for the simplified bc compartment of MBS2023 results into a 4-fold increase in the diffusion distance, which yields a significant slowing of diffusion. In contrast, Ca^{2+} diffusion is faster in atria than in ventricles and therefore it cannot be a slow process physiologically (Tanaami et al., 2005). Hence, in our model $x_{ss\text{-}bc}$ was kept as it is in KM2011, i.e. 0.8125 μm to give a fast diffusion of Ca^{2+} in the cytosol. KM2011 has a single arbitrary cytosolic buffer whose dissociation coefficient K_d and concentration values correspond to the characteristics of calmodulin (CMDN). For bidirectional coupling, TRPN was included in the cytosol with the existing CMDN buffer (Ji et al., 2015). The bidirectional coupling of the AP and contraction modules has been described in detail in the section on 'Electromechanical coupling and mechano-calcium feedback'. Apart from this, the Ca^{2+} diffusion via mobile buffer in the bc compartment was no longer needed in our model since MBS2023 now has a single bc compartment. The absence of mobile buffers and functional T-tubules in the model makes Ca-SR release the main source of spatial spread of Ca^{2+} signal other than the diffusion seen in experiments (Walden et al., 2008). Hence, the differential equations for both free intracellular Ca^{2+} ($[Ca^{2+}]_i$) and Ca^{2+} in SR ($[Ca^{2+}]_{SR}$) were modified and are listed in Appendix 1.

Ca^{2+} transport in the SR

Within SR, the bidirectional SERCA pumping and buffering has the same formulation as the KM2011 model. Other than this, KM2011 adopted the numerical value of the SERCA buffer affinity from ventricular myocytes reported in Shannon et al. (2000). However, an increased SERCA activity with fast uptake dynamics was found in atria (Walden et al., 2009). In KM2011 model, the SERCA affinity formulation is based on the regulatory protein phospholamban (PLB) and SERCA expression levels (Koivumäki et al., 2009). A low level of SERCA inhibitory protein (PLB) along with high SERCA expression eventually leads to the raised affinity of SERCA buffer for human atria (Bokník et al., 1999). Moreover, less PLB inhibition of SERCA directly affects the SERCA dynamics too. Thus, in our model, the affinity of SERCA buffer was modified to meet human atrial SERCA activity levels (Koivumäki et al., 2014, Supplementary Section).

On the release side, the Ca^{2+} release from RyR channels has a Hodgkin-Huxley formulation in KM2011 that consists of activation, inactivation and an adaptation gate. The adaptation gate adapts the RyR open probability according to the intracellular Ca^{2+} environment. Since we have modified the intracellular Ca^{2+} levels, the RyR adaptation level was modified accordingly, to maintain a physiological Ca^{2+} concentration both in the cytosol and in the SR. In the bc compartment, MCF was introduced by the inclusion of troponin-like fast buffer and this resulted in a depressed Ca^{2+} peak and slower relaxation kinetics (Michailova et al., 2002; Smith et al., 2019). This lower Ca^{2+} peak was the consequence of less release flux, J_{rel}, from the RyR in the bc compartment. Hence, an adjustment of Ca^{2+} release was required to give a physiological level of CaT. For the systolic value, we modified adaptation parameters of the bc compartment, i.e. the saturation level and the sensitivity of adaptation. The saturation value was reduced so that the release gate activation can saturate at lower $[Ca^{2+}]_{bc}$ values and the adaptation sensitivity was increased. On the other hand, the relaxation kinetics were more dependent on the contraction dynamics modelled by RDQ2020. Therefore, an automatic optimization was carried out for the time related biomarkers relevant to contraction. This is elaborated in the section on 'Optimization of contraction parameters'.

At higher beating frequency, the incidence of CaT and AP alternans was observed in the model. In general, the vulnerability of Ca^{2+} induced alternans is often associated with steep non-linear $[Ca^{2+}]_{SR}$ dependence on J_{rel} (Díaz et al., 2004; Xie et al., 2008). However, cytosolic Ca^{2+} alternans were also observed without any significant concurrent oscillations in diastolic $[Ca^{2+}]_{SR}$ in single myocytes (Hüser et al., 2000; Picht et al., 2006). For

instance, Shkryl et al. (2012) observed experimentally in rabbit atrial myocytes that the inactivation kinetics and the refractoriness of RyR release was the key mechanism behind Ca^{2+} alternans generation. Similar results were observed in experiments in human atrial cells (Llach et al., 2011) where the mechanism proposed for alternans was the slow recovery of release. For this reason, we modified the refractoriness of RyR gate, both in ss and bc compartments by increasing the recovery from inactivation time from its standard value of 200 ms (Stern et al., 1999). This was achieved in the model by increasing the inactivation time constants for the recovery period from 15 to 450 ms and from 87.5 to 656 ms for ss and bc compartments, respectively. Moreover, the inactivation time constant for the ss compartment was also updated from 15 to 60 ms. In this way, the J_{rel} fluxes for ss and bc had a slow decay time and hence a comparable total time duration.

Alternans protocol

To characterize the AP and CaT alternans, MBS2023 requires faster rates under control condition. To quantify the role of potential parameters both from AP and contractility in the incidence of alternans at higher rates, we used a pacing protocol similar to the one used in a clinical study (Narayan et al., 2011) and in computational modelling (Zile & Trayanova, 2018). Under iso-sarcometric conditions, at a basic cycle length (BCL) of 750 ms, the model is paced for 1000 beats to reach the steady state condition. Using this steady state value as the initial condition, the model was paced further for 74 beats with BCL decreasing from 500 to 200 ms in 50 ms steps. From our literature study, the parameters that were analysed using this pacing protocol were Ca^{2+}-handling-related (the RyR inactivation time (tau_{inact}), SERCA pumping rate ($k_{4\text{-SERCA}}$), SERCA expression ([SERCA])), contraction-related (thin filament Ca^{2+} binding sensitivity ($k_{\text{d-TRPN}}$), thin filament rate constant (K_{off}), cross bridge cycling (XB_{cy}), rate constant (K_{basic})), the coupling effect, i.e. MCF, and CaMKII-related (expression of CaMKII ([CaMKII])). For the analysis, all the parameters were varied between a range of values obtained by increasing values up to 2-fold and reducing them 0.5-fold.

Based on a comprehensive alternans analysis (Zile & Trayanova, 2018), we defined a similar measure to quantify the magnitude of AP and CaT alternans. Alternans normalized magnitude (ANM) was calculated as the mean of change over the consecutive last 10 pairs of beats during a BCL divided by the mean value over the last 10 beats and is given as:

$$\text{ANM} = \frac{\sum_{b=63}^{73} |X_b - X_{b+1}|/10}{\text{avg}(X)_{b=64\ to\ 74}},$$

where X is AP or CaT biomarkers like APD_{90}, APD_{50}, and CaT_{peak}, thus giving the three alternans measures APD_{90}-ANM, APD_{50}-ANM and CaT-ANM. The threshold used for alternans to be considered significant was ANM > 5%.

Sarcolemmal ion currents

Few of the sarcolemmal currents were re-formulated, modified or newly included in comparison to the KM2011 model, as shown in dark grey in the schematic of Fig. 2. The inward sodium current (I_{Na}) was reformulated according to new experimental data as described in Skibsbye et al. (2016). The L-type Ca^{2+} current (I_{CaL}) gating was modified as explained in Koivumäki et al. (2014) (KM2014). In comparison to KM2014, steady state inactivation for the fast VDI gate was adopted from KM2011 to avoid irregular reactivation of I_{CaL} at the low frequency of 0.5 Hz. As a result, the I-V curves for both KM2011 and KM2014 versions were compared with data (Li et al., 1997) under voltage clamp protocol given in Fig. A1. Our modified formulation of I_{CaL} is in better agreement with the experimental data in comparison to KM2014. Apart from this, all other minor modifications in conductance values have been listed in Table A5, section A.

The mechano-activated channels (MACs) allow the stretch-activated currents (I_{sac}) to flow. On the cellular scale, MACs are the stretch activated gates that are classified according to the stimulus type by which they are activated, i.e. either by using mechanical stimulus alone or by a combination of different stimuli. However, in this work, we have considered those channels that are activated by mechanical stimulus alone.Very often, I_{sac} is subdivided into K^+ selective (I_{K0}) and non-selective (I_{ns}) cations channels. I_{ns} allows Na^+, Ca^{2+} and K^+ to enter the cells and its reversal potential, based on the relative permeability of ion channels, is halfway between the resting membrane potential (RMP) and the plateau potential, i.e. 0 and −50 mV, and has a near-linear voltage dependence (Kim, 1993). Therefore, the activation of I_{ns} can depolarize the cells, but during the plateau phase can cause the repolarization of the AP. In contrast, the reversal potential of I_{K0} is close to RMP; therefore it can modulate the repolarization phase more than the RMP of the AP. In the model, the I_{ns} current is permeable to Na^+, K^+ and Ca^{2+} and it is defined as:

$$I_{ns} = I_{ns,Na} + I_{ns,K} + I_{ns,Ca}.$$

where I_{ns} is the ion-specific contribution of Na^+, K^+ or Ca^{2+}. The driving force of each $I_{ns,X}$ (where X refers to

ion contribution of Na^+, K^+ or Ca^{2+}) is modelled by the Goldman-Hodgin-Katz (GHK) based formulation:

$$I_{ns,X} = P_X \; g_{ns} \frac{z_X^2 \, F^2 V_m}{RT} \; \frac{[X]_i - [X]_o \exp\left(-\frac{z_X F \, V_m}{RT}\right)}{1 - \exp\left(-\frac{z_X F \, V_m}{RT}\right)},$$

where P_X is the permeability of X ion Na^+, K^+ and Ca^{2+}, z_X is the ion valency for each ion, and the rest of the constants are defined as in KM2011. For our model the permeability ratio $P_{Na} : P_{Ca} : P_K$ was fixed as 1:1:1, which gives a linear *I-V* relationship for I_{ns} current with a reversal potential near 0 mV (Fig. A7, red triangles) as was shown for rat atrial myocytes (Kim, 1993). A sensitivity analysis, based on a 3-fold increment of each ion permeability at a time, predicted that changes in P_{Na} and P_K can increase (25 mV) and reduce (−25 mV) the reversal potential of I_{ns}, respectively, as shown in Fig. A7 (yellow plus marks and blue squares, respectively). Moreover, Kim suggested the P_{Ca}/P_K ratio to be equal to 0.9 (Kim, 1993) and we have adopted this ratio from Kuijper et al. as 1 (Kuijper et al., 2007). Thus, we opted for an equal permeability ratio for all the three ion channels in our model. The effect of stretch change was introduced in the I_{ns} current by a conductance g_{ns} equation, given as,

$$g_{ns} = \frac{g_{ns,max}}{1 + K_{ns} \exp\left[-\alpha_{ns}\left(\lambda - 1\right)\right]},$$

where $g_{ns,max}$ is the maximal conductance, K_{ns} is the parameter that sets the amount of current in the absence of stretch ($\lambda = 1$), and α_{ns} is the sensitivity to stretch. All the parameter values are listed in Table A5, section C in Appendix 3. Furthermore, the I_{ns} current formulation was included in electrolyte equations as:

$$\frac{d\left[Na^+\right]_i}{dt} = \frac{-(I_{Na} + I_{Nab} + 3I_{NaK} + 3I_{NaCa} + I_{fNa} + I_{ns,Na})}{V_{ss} \, F}$$

$$\frac{d\left[K^+\right]}{dt} = 0,$$

$$\frac{d\left[Ca^{2+}\right]_{ss}}{dt} = \frac{-I_{CaL} - I_{Cab} - I_{CaP} + 2I_{NaCa} - I_{ns,Ca}}{2V_{ss}F},$$

where V_{ss} is the volume occupied by the ss compartment, and the rest of the constants are the same as the original model. For I_{K0} current, we have considered the formulation for rat ventricular myocytes by Niederer and Smith (Niederer & Smith, 2007) with a change in offset for γ_{K0} that is the measure of strain dependence for conductance. A small offset was included to nullify the effect of I_{ns} current at basal rate when CMs were not in a stretched state. Briefly, the conductance is a function of strain and is modeled as:

$$\gamma_{K0} = \beta_{K0} \; (\lambda - 1) + 0.001,$$

and I_{K0} becomes

$$I_{K0} = g_{K0} \; \frac{\gamma_{K0}}{1 + \exp -\frac{10+V}{45}} \left(V - E_K\right).$$

All the other constants were the same as in Niederer & Smith (2007).

Parameter validation for I_{ns}. We have validated the I_{ns} current parameters based on the average current values on negative pressure ranging from 0 to 80 mmHg extracted from Jakob et al. (2021). The measurements are obtained from 11 tissue donors and 110 cells. The model output for the I_{ns} (red line) fit to the experimental data is shown in Fig. A5 (blue line), and it increases up to $\lambda = 1.25$ followed by a plateau that fits qualitatively with the experimental average current values, i.e. −20 pA. The calibrated set of parameters thus obtained are listed in Table A5, section C, which shows a high sensitivity towards stretch, i.e. $\alpha_{ns} = 30$ and a maximum conductance of $g_{nsmax} = 0.461$e-6 nS. The permeability ratio is made the same for all three ion channels. Using these calibrated parameters of I_{ns}, we evaluated the effect of increasing stretch level on the MBS2023 model in the Results section.

Electro-mechanical coupling and mechano-calcium feedback

Using our modified version of KM2011 as the AP module and RDQ2020 as the contraction module, we built a coupled model of human atrial CMs with MER loop. The CaT from the AP module served as an input to the contraction module in a feedforward manner and the dynamic effect of Ca^{2+} bound to TRPN ($\frac{d[Ca^{2+}]_{TRPN}}{dt}$) from the contraction module was the feedback to the free CaT in the AP module, i.e. the MCF. In this way, a bidirectional strong electro-mechanical coupling was ensured. Mathematically, the integration of the AP and contraction modules was performed in accordance with Ji et al. (2015) and later by Timmermann et al. (2017). We defined the amount of calcium bound to TRPN ($[Ca^{2+}]_{TRPN}$) as the fraction of TRPN units with Ca^{2+} bound to its regulatory binding site (Ca_{TRPN}) multiplied by a constant maximum concentration of Ca^{2+} that can bind to TRPN ($[Ca^{2+}]_{TRPN,max} = 0.56$ mM), leading to:

$$\frac{d\left[Ca^{2+}\right]_{TRPN}}{dt} = \left[Ca^{2+}\right]_{TRPN,max} \frac{dCa_{TRPN}}{dt}, \qquad (1)$$

where the $[Ca^{2+}]_{TRPN,max}$ was set to the minimum concentration allowed for 50% of accessible volume (Fabiato et al., 1983; Robertson et al., 1981). The differential equation for $[Ca^{2+}]$ was modified after adding the troponin feedback from the contraction module.

Ca_{TRPN} from Eqn (1) is computed from RDQ2020 as follows:

$$Ca_{TRPN} = B_{so}X_{SO}\,(SL) + B_{nso}\,(1 - X_{SO}\,(SL))\,, \qquad (2)$$

where B_{so} and B_{nso} are the ratio of bounded TRPN units in the single-overlap zone (SO) and in the non-single-overlap zone (NSO), respectively, and $X_{so}(SL)$ is the function of the size of the single overlap zone that models the effect of SL changes. On the one hand, B_{so} was already modelled in the original RDQ2020 model as:

$$B_{so} = \sum_{\alpha,\beta,\delta} \pi\,(\alpha, \beta, \delta, \mathrm{B})$$

where $\pi\,(\alpha, \beta, \delta, \mathrm{B})$ is the ratio of TRPN being permissive, regardless of the state of the tropomyosin (Tm) triplet α, β, δ. On the other hand, we introduced the variable B_{nso}, whose dynamic is modelled as:

$$\frac{dB_{nso}}{dt} = k_{off}\frac{\left[Ca^{2+}\right]_i}{k_D\,(SL)}\,(1 - B_{nso}) - k_{off}B_{nso}.$$

Experimental data. The contraction parameters in the RDQ2020 model were calibrated according to ventricular human data recorded at body temperature (see Table 3, Regazzoni et al., 2020). Hence, to adopt human atrial-like physiology, a re-calibration of contraction parameters was required. This calibration was based on a few biomarkers extracted from the *in-vitro* experimental data available for human atrial trabeculae, summarized in Table A2. Instead of employing the *in-vitro* data from single cardiac myocytes, the calibration data for our model was based on tissue level preparations. The removal of CM from its normal environment has a significant impact on its electrical and mechanical functionality because of its loss of interaction with several other cells (Pfeiffer et al., 2014). Therefore, tissue level data allow the myocytes to be studied in an environment that more closely mimics *in-vivo* conditions.

Optimization of contraction parameters. The major difference between atrial and ventricular contraction lies in the contractile protein myosin and its iso-enzymatic variety (Reiser et al., 2001; Narolska et al., 2005; Morano et al., 1988). Contractile protein myosin is the major determinant of contractility since it can modulate the ATPase activity and maximum shortening velocity (v_{max}). Accordingly, the contraction and relaxation kinetics are faster in atria than ventricles (Piroddi et al., 2007). Moreover, the Ca^{2+} sensitivity of atrial fibre is also less than ventricles (Morano et al., 1988).

Based on these observations, the contraction dynamics of regulatory unit (RU), i.e. the TRPN and Tm units were modified. The dynamics were based on transition rates (k_{off} and k_{basic}), the cooperativity (γ) and the Ca^{2+} sensitivity (k_d). The optimized set of parameters was obtained on the basis of time-related biomarkers of F_{active}, i.e. relaxation time at 50% and 90% of peak values ($rt_{50Factive}$, $rt_{90Factive}$), time to F_{max} ($ttp_{Factive}$), and twitch time ($TT_{Factive}$). This optimization was carried out at basal frequency of 1 Hz and then the optimized model parameters were used for simulations at other frequencies (see the comparison of model output with experimental data normalized by 1 Hz in Fig. A2). The late relaxation phase of F_{active}, i.e. $rt_{90Factive}$ demonstrates rate dependency and the model has reproduced it. In contrast, the $ttp_{Factive}$ and $rt_{50Factive}$ shows a flat behaviour with respect to rate and it should be noted that the only available experimental data (Sossalla et al., 2010) shows a flat rate dependency for overall relaxation phases of F_{active}. The model output for $rt_{50Factive}$ shows a contrasting behaviour with respect to the data and this was a expected result after looking into the rate dependent shortening of $rt_{90Factive}$. The human *in-vitro* data collection used for this calibration is listed in Table A2. Similarly, biomarkers were also computed for the CaT – the diastolic level (CaT_{min}), the systolic value (CaT_{max}), the amplitude (CaT_{amp}) relaxation time at 50% of CaT_{max} (rt_{50Ca}), time to CaT_{max} (ttp_{Ca}), total time duration (TT_{Ca}), and the decay time (τ) – and compared with a small set of data from Table A2. The calibration was performed using the Matlab (The MathWorks, Natick, MA) *fminsearch* optimization function to find local minima. In this way, the model parameters were tuned in accordance with the human atrial *in-vitro* data to adopt atrial-like physiology.

Other parameters based on cross-bridge cycling (XB_{cy}), i.e. $\mu^0_{f_p}$, $\mu^1_{f_p}$, α, and r_0 were also calibrated by following the procedure presented in Regazzoni et al. (2021). This calibration was based on difference in v_{max} of XB_{cy} for human atria from ventricles (Kuijpers et al., 2007). Using the new v_{max} value, based on the best fit with force-velocity hyperbolic curve we re-calibrated the XB_{cy} parameters (Table A2).

Modelling mechano-electric feedback

The model simulates MEF-based phenomena by including mechanical activity of the CMs. MEF was modelled by using a three-element rheological scheme (Solovyova et al., 2002) also shown in Fig. 3. The contractile element (CE) is responsible for generating F_{active} and is the one produced by RDQ2020. The element has a length of SL and a resting length, SL_r, i.e. the length when the segment is relaxed and no force is applied. The force developed by CE unit is given as:

$$F_{CE} = f_{CE}\,F_{norm}\left(SL, Ca^{2+}, v\right), \qquad (3)$$

where f_{CE} is a scaling factor and F_{norm} is the normalized active force generated by RDQ2020 that is dependent

on SL, Ca^{2+} dynamics, and the shortening velocity v of the XBs. The MEF-based mechanical modulation of Ca^{2+} was already modelled in RDQ2020, since Ca-TRPN sensitivity k_d was a function of SL. The passive elastic effect is introduced in two forms, i.e. by the series (SE) and parallel (PE) elements. Mathematically, the passive forces developed by SE and PE were modelled as non-linearly related to lengths l_{PE} and l_{SE}:

$$F_{SE} = f_{SE} \left\{ \exp\left[k_{SE}\left(l_{SE} - l_{SEr}\right)\right] - 1 \right\} \quad (4)$$

and

$$F_{PE} = f_{PE} \left\{ \exp\left[k_{SE}\left(l_{PE} - l_{PEr}\right)\right] - 1 \right\}, \quad (5)$$

where f_{SE} and f_{PE} are the scaling factors, k_{SE} and k_{PE} are the spring constants, and l_{SEr} and l_{PEr} are the resting lengths for each element. Under mechanical equilibrium, the total force of the mechanical segment ($F_{segment}$) is computed as $F_{segment} = F_{PE} + F_{SE}$; length of the segment as $l_{PE} = l_{SE} + SL$; and the series forces as $F_{SE} = F_{CE}$.

The three-element mechanical model equations were solved by using the numerical scheme described in Solovyova et al. (2002). Two new state variables were integrated into the model, i.e. $l_1 = SL - SL_r$ and $l_2 = l_{PE} - l_{PEr}$ and eqns (4) and (5), were modified accordingly. Moreover, an assumption on resting lengths was made, $l_{PEr} = SL_r$, and, as a consequence, $l_{SEr} = 0$. Based on this, the mechanical state of each element is defined by l_1, l_2, v, $\frac{dl_1}{dt}$, $\frac{dl_2}{dt}$, $\frac{dv}{dt}$. Under iso-sarcometric condition for $\lambda = 1$, the lengths of contractile and parallel elements were held constant, i.e. $\frac{dl_1}{dt}, \frac{dl_2}{dt}, \frac{dv}{dt} = 0$ whereas, for isometric simulations $\frac{dl_2}{dt} = 0$, $\frac{dl_1}{dt} = -v$, and the sarcomere shortening velocity v was modelled as:

$$\frac{dv}{dt} = \frac{F_{CE} - F_{SE}}{Ir} \quad (6)$$

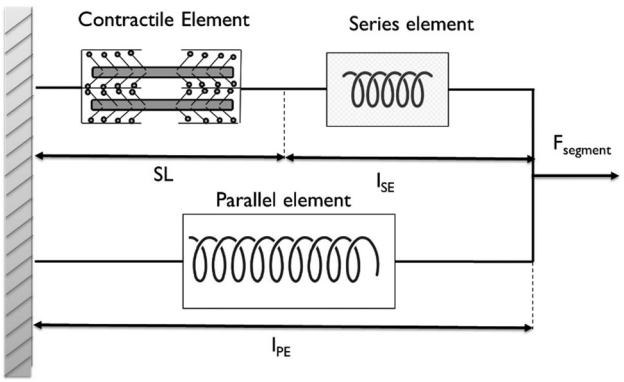

Figure 3. Three element rheological scheme for modelling the mechanical activity of the cell in MBS2023 model
The scheme consists of a contractile element of length SL from RDQ2020 module, responsible for active force development and two passive elements, the series (SE), and the parallel element (PE) of length l_{SE} and l_{PE}, respectively.

where Ir is the inertial parameter, and all other constant parameter values are listed in Table A5, part C.

CaMKII based phosphorylation of ionic currents and Ca^{2+} handling

Ca^{2+}/CMDN-dependent kinase II (CaMKII) is a multifunctional serine/threonine kinase expressed ubiquitously in the CMs (reviewed in Bers & Grandi, 2009). CaMKII plays an important role in regulating cardiac excitability and contractility. Ca^{2+} mediated modulation of ion channels is carried out either through direct Ca^{2+}-CMDN binding or by the activation of CaMKII. CaMKII can phosphorylate numerous targets involved in ion channel gating, Ca^{2+} handling, and in regulatory proteins. In the literature, many studies have been performed on the biochemically detailed models of CaMKII signalling but the focus of these studies was on ventricular electrophysiology (Soltis & Saurceman 2010; Morotti et al., 2021). As the MEF integration differs among the atrial and ventricular CMs because of differences in ultrastructure and Ca^{2+} homeostasis, therefore it is crucial to study the atrial model integrated with CaMKII modulated targets, based on atrial physiology and pathophysiology. For atrial CMs, Zhao et al. have developed an atrial cell model including CaMKII activation to explore the mechanism induced by atrial arrhythmia under oxidative stress (Zhao et al., 2020). Another model by Ni et al. integrates electrophysiology and Ca^{2+} handling with a biochemically detailed systems model of upstream signalling pathways, i.e. protein kinase A (PKA) and CaMKII in human atria (Ni et al., 2023).

In human atrial CMs, CaMKII acts on diverse targets in ion channels and Ca^{2+} handling as listed in Table 1. The CaMKII model was adopted from O'Hara ventricular model formulation (O'Hara et al., 2011), where each target T is divided into two parts,

$$T = (1 - \phi_{CAMK})\ T_{NP} + \phi_{CAMK} T_{CaMK},$$

where T_{NP} is the non-phosphorylated part of the target, T_{CaMK} is the CaMKII modulated part of the target, and the ϕ_{CAMK} is the proportion affected by CaMKII and is given as:

$$\phi_{CaMK} = \frac{1}{1 + \frac{K_{m,CaMK}}{CaMK_{active}}}$$

where $CaMK_{active}$ is the fraction of active CaMKII binding sites, $K_{m,CaMK}$ is the half-saturation coefficient, which was the same as the O'Hara CaMKII model. $CaMKII_{active}$ is given as:

$$\text{CaM K}_{active} = \text{CaMK}_{bound} + \text{CaMK}_{trap},$$

Table 1. Effect of CaMKII based phosphorylation of the cellular targets of human atrial cardiomyocytes

Target	Effect of CaMKII-dependent phosphorylation	Reference
Fast I_{Na}	Slow inactivation gate slowed by 1.46 times	(Zhang et al., 2015)
I_{CaL}	1. Current increased by 40% 2. Voltage dependent inactivation gate slowed by 1.5	(Christ et al., 2004)
I_t	1. Current reduced by 10% 2. Inactivation time slowed by 1.56 times	(Tessier et al., 1999)
I_{Kur}	Current increased by 57%	
RyR	Opening probability increased and leak current increased by 2.5 times.	(Neef et al., 2010; Voigt et al., 2012)
SERCA	Pumping activity increased by 27% by a direct effect and reduction in PLB inhibition, an indirect enhancement, of forward pumping rate by 70%.	(Koivumaki et al., 2009)

where $CaMK_{bound}$ and $CaMK_{trap}$ are the fractions of CaMKII binding sites bound to Ca^{2+}/CMDN and with trapped CMDN respectively and are given as:

$$\text{CaM K}_{\text{bound}} = \text{CaMK}_0 \frac{1 - \text{CaMK}_{\text{trap}}}{1 + \frac{K_{\text{m,CaM}}}{[\text{Ca}^{2+}]_{\text{ss}}}}.$$

Here $CaMK_0$ is the fraction of active CaMKII binding sites at equilibrium, $K_{m,CaM}$ is the sensitivity factor of CaMKII bound to Ca^{2+}/CMDN. Hence, $CaMK_{bound}$ quantifies the dependence on $[Ca^{2+}]_{ss}$. $CaMK_{trap}$ is a dynamic quantity and is given as:

$$\frac{\text{dCaMK}_{\text{trap}}}{\text{dt}} = \alpha_{\text{CaMK}}\,\text{CaMK}_{\text{bound}}\left(\text{CaMK}_{\text{bound}} + \text{CaMK}_{\text{trap}}\right) - \beta_{\text{CaMK}}\text{CaMK}_{\text{trap}},$$

where α_{CaMK} and β_{CaMK} are the transition rates. All the values used for CaMKII model constants are listed in Table A5, section B.

The model presented is based upon an ordinary set of differential equations implemented in Matlab using a stiff ordinary differential equation solver method (ode15s). Under the basal conditions, the model was simulated at 1 Hz frequency and 800 beats to reach the steady state. The simplification made in the AP module made it more computationally efficient so that it was now defined by considering 30 state variables in comparison to 43 variables of the parent model. Consequently, this simplified description of intracellular Ca^{2+} dynamics reduced the computational load of the AP module by 15% than the parent model for a 10-s simulation and at 1 Hz pacing takes about 1.7 s to run on a desktop PC (AMD Ryzen 7 CPU, 1.90 GHz, 16 GB of RAM). All the modifications introduced for the formulation of the model are shown in Appendix 1.

Results

AP, Ca^{2+} transient and active force characteristics and biomarkers

The simulated steady state characteristics of the AP waveform, Ca^{2+} transient in ss and bc compartments, and F_{active} are shown in Fig. 4. The modifications with respect to the parent model, KM2011, resulted in a type-3 human atria AP morphology, i.e. triangular AP with no dome (Dawodu et al., 1996) (Fig. 4*A*). The model shows a prominent plateau phase with respect to the parent model that was achieved by the slow inactivation of I_{CaL}. The role of the modified formulation of I_{CaL} (as explained in the Methods section) in producing the AP shape of MBS2023 is assessed in Fig. 5 where the modified I_{CaL} led to a prominent lengthening of the plateau, early and late repolarization phase of the AP (dashed line in red *vs.* dotted-dashed line in purple). The CaT produced by the model is presented in Fig. 4*B*. As expected, the amplitude is greater in the ss than in the bc compartment (0.678 *vs.* 0.22 μM), with similar diastolic levels (0.179 *vs.* 0.187 μM). A temporal heterogeneity is also evident in the dynamics of the transient; moving to the centre, CaT is slowed and delayed, as quantified by the differences in biomarker values between ss and bc: δttp_{Ca} 61 ms, δrt_{50Ca} 100 ms, and δTT_{Ca} 256 ms. The mean CaT (that is the weighted average between cytosolic compartments, to be compared with experimental measurements) was computed and its time course was substantially equal to that of the Ca^{2+} transient in the bulk cytosol (not shown). The Ca^{2+} handling behaviour for MBS2023 can be analysed using the $[Ca^{2+}]_{SR}$ traces from ss and bc compartments in Fig. 4*D*. In the ss compartment, a prominently large Ca^{2+} release can be seen from the SR into the ss compartment, with fast release flux dynamics (Fig. A4*D vs. H*, red continuous line). Conversely, in the bulk cytosol, the Ca^{2+} release is smaller (Fig. A4*G*, red continuous line), slower, and slightly delayed, resulting in more Ca^{2+} SR load. The force developed (F_{active}) in the bulk cytosol because of the coupling is shown in Fig. 4*E*.

A quantitative comparison of AP, CaT and F_{active} biomarkers with *in-vitro* human atrial data ranges is presented in Fig. 4 and Table 2. The simulated biomarkers are plotted using biomarker-specific markers and colour bars representing their *in-vitro* variability ranges. The dashed lines represent the *in-vitro* biomarker mean values, also reported in Table 2. Most of the biomarkers are within the range of the experimental ones. In particular, the APs simulated by MBS2023 (in blue) and KM2011 (in red) are compared in Fig. 4*A*, together with their APD_{50} and APD_{90} biomarkers. Our AP model has a more dominant plateau than KM2011 and is more in agreement with the mean APD_{50} reported by the *in-vitro* data range. For late repolarization, APD_{90} seems comparable for both models and lies on the mean value of the data. The MBS2023 CaT upstroke is faster compared to KM2011 (Fig. 4*C*), while its decay is slower (within the experimental range, Fig. 4*C*). The dynamics of F_{active} have been compared with the mean CaT of each model along with their ttp and rt50 biomarkers (Fig. 4*F*). The CaT arises earlier and decays more slowly than F_{active}, as also shown by the light and dark data range colours, respectively (Fig. 4*F*). The rising part of the CaT and F_{active} curves are compared using ttp, where a ttp_{Ca} smaller than $ttp_{Factive}$ can be observed. The ttp_{Ca} is slightly longer than the data range but $ttp_{Factive}$ is within the lower data bound (Fig. 4*F*). The comparison of the relaxation phase was carried out in Fig. 4*F* inset, where both curve peaks were aligned to highlight that rt_{50Ca} is longer than $rt_{50Factive}$. Moreover, $rt_{50Factive}$ lies quite close to the lower bound of the data range.

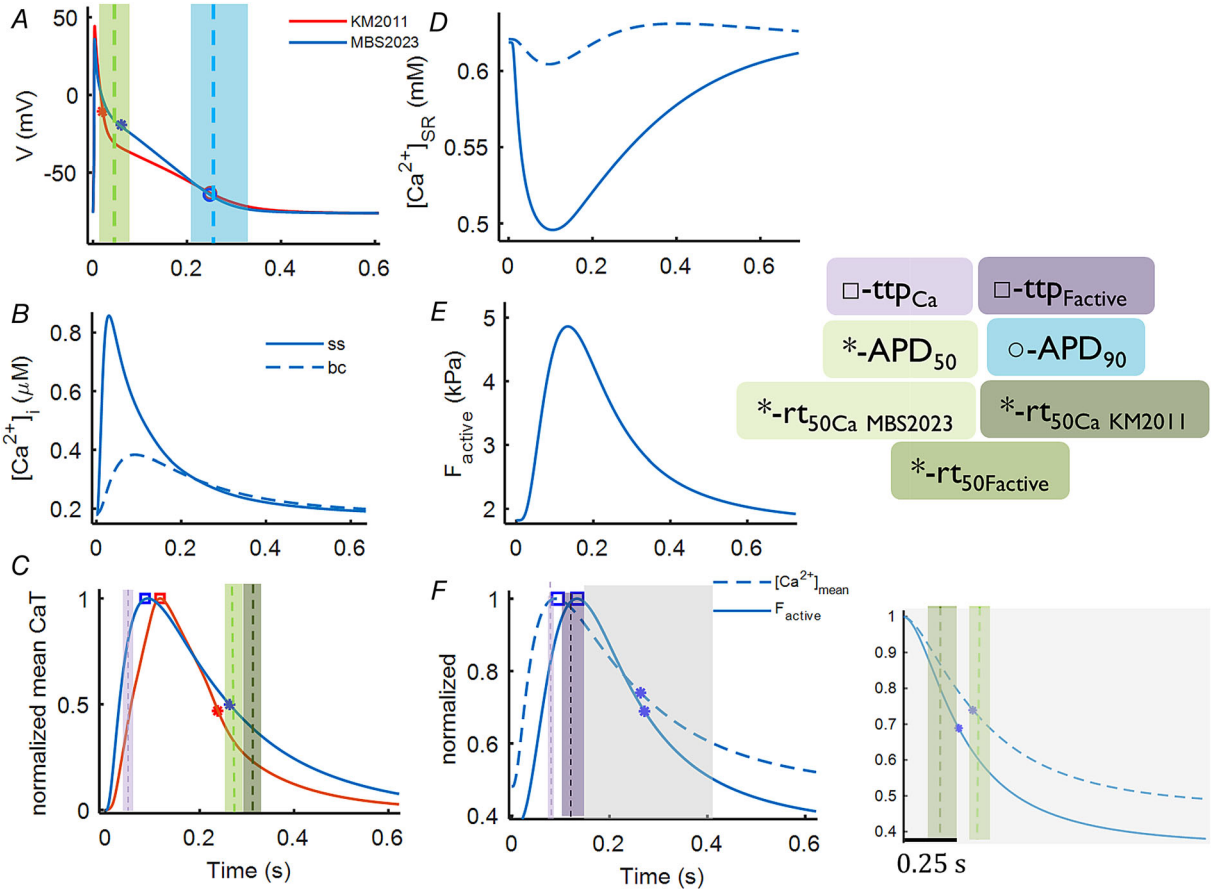

Figure 4. AP, Ca^{2+} handling and F_{active} characteristics obtained with the MBS2023 model compared to those obtained with the KM2011 model and experimental human atrial data
A few selected biomarkers are also plotted using various marker labels like ttp_{Ca} or $ttp_{Factive}$ with open squares, APD_{50} or rt_{50Ca} or $rt_{50Factive}$ with asterisks, and APD_{90} with open circles. The colour for each shaded area corresponds to the data range of a biomarker as also reported in Table 2. *A*, comparison of AP traces for MBS2023 (in blue) with KM2011 (in red) and with experimental APD_{50} and APD_{90}. *B*, Ca^{2+} transients for subspace (continuous), and bulk cytosol (dashed line). *C*, comparison of normalized mean (i.e. weighted average between cytosolic compartments) Ca^{2+} transient from MSB2022 (in blue) and KM2011 (in red) and with experimental ttp_{Ca} and rt_{50Ca}. *D*, Ca^{2+} concentration inside the SR for both ss and bc subcompartments. *E*, F_{active} produced by the EM coupling in MBS2023 model. *F*, comparison of normalized mean Ca^{2+} transient and F_{active} time course in the MBS2023 model (inset: alignment of the same curve with respect to their time to peaks for the sake of comparing the relaxation dynamics of the Ca^{2+} transient (dashed line) and F_{active} (continuous line)).

Table 2. Comparison of AP, Ca^{2+} transient, and F_{active} biomarkers obtained with the model and the values (lower and upper bounds along with their mean values) from *in-vitro* human atrial data extracted from references in Table A2 and A4

Action potential			Ca^{2+} transient			Active force		
Biomarker	Mean value range [LB, UB]	Model output	Biomarker	Mean value range [LB, UB]	Model output	Biomarker	Mean value Range [LB, UB]	Model output
APD_{90} (ms)	263.05 [202, 332]	248	Ca_{amp} (μM)	0.268 [0.18, 0.4]	0.221	F_{active} (kPa)	5.92 [3.14, 9.5]	4.7
APD_{50} (ms)	50.02 [25, 94.14]	60.2	Ca_{dias} (μM)	0.223 [0.2, 0.25]	0.187	$ttp_{Factive}$ (ms)	104.98 [79.5, 161]	135.7
APD_{30} (ms)	7.725 [5, 13.9]	13.4	ttp_{Ca} (ms)	52.5 [49.4, 55.6]	93.7	$rt_{50Factive}$ (ms)	80.92 [60.2, 118.6]	140
V_{amp} (mV)	103.266 [83, 130]	111.7	rt_{50Ca} (ms)	177.5 [168.5, 186.5]	176	$rt_{90Factive}$ (ms)	200 [153, 235.9]	406
V_{diast} (mV)	−75.1 [−68, −75.1]	−75.7	TT_{Ca} (ms)	539.1 [508.1, 570.1]	690	$TT_{Factive}$ (ms)	433.3 [413.1, 453.5]	663
dV/dt_{max} (mV/ms)	179.23 [159, 231.9]	177	τ (s^{-1})	335 [220, 450]	288			

Effect of CaMKII inhibition on MBS2023 model characteristics

All the major currents for the MBS2023 model at the basal frequency of 1 Hz are shown in Fig. A3 (red continuous line). The effect of CaMKII inhibition (blue dashed line) on the AP is compared with the basal condition of the model where shortening of the mid-repolarization phase is observed, as shown in Fig. A3A. Two of the AP biomarkers, i.e. dV/dt_{max} and V_{amp} are compared with the experimental data (Leberk et al., 2018) where a qualitative equivalence can be observed. Among the ionic currents, I_{Na} shows a increase (Fig. A3B), and the I_K current shows slightly fast inactivation (Fig. A3F and G). The Ca^{2+}-transient and all the incoming and outgoing fluxes are shown in Fig. A4 (red continuous line) along with the effect of CaMKII inhibition (blue dashed line). The CaT in *ss* (Fig. A4A) rises instantly and decay is also fast in comparison to CaT in bc (Fig. A4E). This is evident with fast release and uptake flux dynamics of the ss compartment (Fig. A4D and C). The CaT propagates towards the bc compartment via diffusion (J_{diff}) (Fig. A4B). In the bc compartment, the release flux is quite small whereas the uptake is very large in magnitude (Fig. A4H and G) in comparison to ss. CaMKII inhibition has reduced the J_{up} flux and has reduced F_{active} (Fig. A4F), as was observed by Lebek et al. (2018).

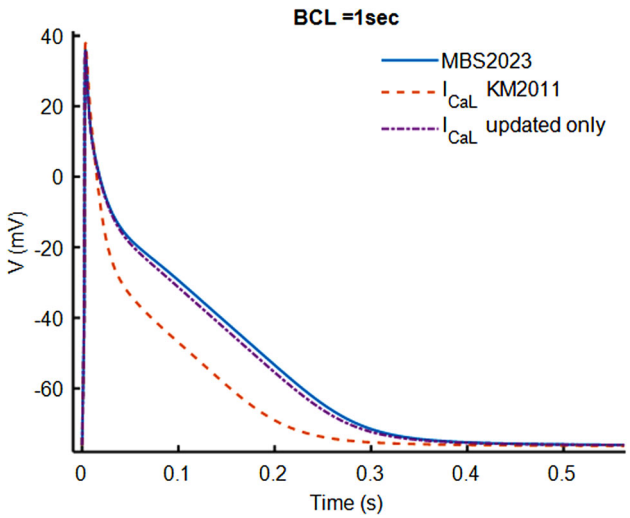

Figure 5. Role of membrane current I_{CaL} in producing action potential for MBS2023 model (blue continuous line) at 1 Hz frequency
Steady-state action potential (AP) for basal model (blue continuous line) compared with AP using KM2011 formulation of I_{CaL} (red dashed line) and AP using updated I_{CaL} current only (in purple dotted-dashed line). [Colour figure can be viewed at wileyonlinelibrary.com]

Mechano-calcium feedback effects

The model characteristics were analysed by keeping SL fixed, in an iso-sarcometric condition as usual in *in-vitro* experiments (referred to in Table A2). The consequence of coupling on AP, CaT and F_{active} for the novel MBS2023 model was analysed by comparing the model output under basal conditions, i.e. bidirectional coupling (continuous line), with noMCF condition (dashed lines), i.e. by removing the dynamic effect of the Ca^{2+} bound to troponin ($d[Ca^{2+}]_{TRPN}/dt$ as shown in eqn (1)). The MBS2023 AP waveform is compared with AP under the noMCF condition in Fig. 6*A*. The AP curve and its kinetics are only slightly affected by MCF and this is demonstrated

by the early repolarization phase. Accordingly, I_{CaL} (Fig 6*B*) shows more inactivation during the plateau of the curve under the noMCF condition. Similarly, under the noMCF condition, we observed an enhanced systolic level of Ca^{2+} in the bulk cytosol (Fig. 6*D*) due to the elevated amount of Ca^{2+} bound to TRPN (Fig. 6*F*), which is not sequestered from the cytoplasm. Moreover, in comparison to the basal state of the model, the CaT peak arrives earlier, and the decay is faster when the MCF effect is switched off. In particular, under the basal state the rt_{50Ca} for the model was within the data range; however, it went completely out of range under the noMCF condition. Although the model in the basal state produces a TT_{Ca} that is longer than the experimental range, under noMCF the TT_{Ca} is far too short, showing a large difference from the experimental range (reported in Table 2). Because of raised Ca^{2+} levels in the bc under the noMCF condition, the exchanger I_{NaCa} shows enhanced inward current followed by a reduction in the latter phase of time, as shown in Fig. 6*C*. Similarly, the F_{active} curve with fast relaxation dynamics was also observed under the noMCF condition, as shown in Fig. 6*E*. Overall, the kinetics of CaT is fully dependent on the dynamics of MCF, i.e. the concentration of Ca^{2+} bound to TRPN.

Quantifying SR Ca^{2+} activity

SR Ca^{2+} content is a major modulator of CaT. Therefore, we simulated the caffeine effect to quantify the SERCA activity by measuring SR Ca^{2+} content and its pumping rate. In experiments, atrial myocytes are preconditioned with an I_{CaL} activation voltage clamp protocol for 1 min. Caffeine (10 mM) causes a large rise in CaT, as a result of SR Ca^{2+} release. The slow decay of CaT is mainly through the I_{NaCa} exchanger, and the integral of the current is a measure of SR Ca^{2+} content.

Following the experiment, Ca^{2+} current and transient were simulated (Fig. 7*A*) following the voltage clamp protocol presented in Grandi et al. (2011) and Voigt et al. (2014) at 0.5 Hz, as shown in Fig. 7*A* (inset). In detail, the protocol starts with a 100 ms ramp from −80 mV (holding potential) to −40 mV to inactivate I_{Na}, followed by a step pulse to +10 mV for 100 ms (Grandi et al., 2011; Voigt et al., 2014). The resultant CaT_{bc} decay phase was fitted on a mono-exponential equation (Voigt et al., 2014 Supplementary information).

The voltage clamp protocol resulted in $CaT_{sys} = 0.41\ \mu M$ (Fig. 7*C*, middle), $Ca_{diast} = 0.179\ \mu M$ (Fig. 7*C*, left), and decay time constant of 288 ms (Fig. 7*D*), corresponding to a decay rate $k_{sys} = 3.47\ s^{-1}$. In comparison to the experiments in Fig. 7*C*, the CaT amplitude matches well with data from Fakuade et al. (2021) and Voigt et al. (2012, 2014), and it is slightly smaller than the value reported by Heijman et al. (2020). The decay rate for CaT (Fig. 7*D*) is in between the reported data, i.e. smaller than Fakuade et al. and Heijman et al. but greater than Voigt et al.

The caffeine induced Ca^{2+} transient (cCaT) experiment was replicated by switching the membrane voltage to holding potential (−80 mV) and running the simulation in the RyRs open state, i.e. both the activation, inactivation and Ca^{2+} SR-dependent activation gates were set to 1, to allow for the maximum release flux to the cytosol. The cCaT is shown in Fig. 7*B* (bottom panel) where the cCaT has a slow decay phase with high amplitude (2.6 times greater than CaT, Fig. 7*E*). The cCaT amplitude is quite equivalent to Fakuade et al.'s data and is smaller than Voigt et al.'s data. The resulting inward current flowing through I_{NaCa} is shown in Fig. 7*B* (top panel), while the integral of I_{NaCa}, representing the measure of SR-Ca^{2+} content, is shown in Fig. 7*F*. The model has a SR Ca^{2+} load equivalent to Voigt et al.'s data but is smaller than the data bar plots

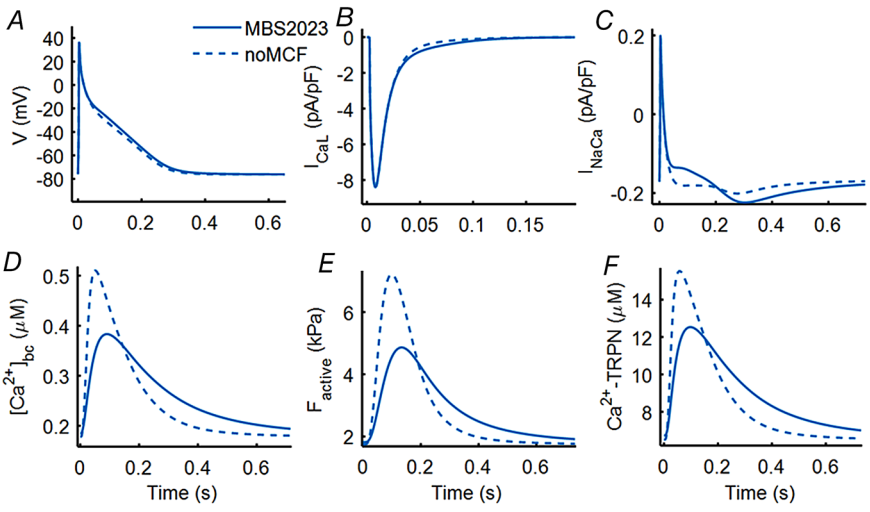

Figure 6. Effect of mechano-calcium feedback on MBS2023
Consequences of coupling on MBS2023 AP (continuous line) in comparison to noMCF (dashed line) condition (*A*), ionic currents I_{CaL} and I_{NaCa} plots with respect to noMCF condition (*B* and *C*), Ca^{2+} transient in bulk cytosol with respect to noMCF condition (*D*), comparison of F_{active} time course with noMCF condition (*E*), and concentration of Ca^{2+} bound to TRPN with and without MCF (*F*). [Colour figure can be viewed at wileyonlinelibrary.com]

from Heijman and Fakuade et al. The SERCA pumping rate (k_{SERCA}) is estimated as:

$$k_{SERCA} = k_{sys} - k_{caff},$$

where k_{caff} is given as:

$$k_{caff} = k_{NaCa} + k_{PCa},$$

where k_{PCa} is a small contribution of sarcolemma Ca^{+} current. Using monoexponential equation with $cCaT_{amP} = 0.9\ \mu M$, and $cCaT_{dias} = 0.163\ \mu M$ we obtained $k_{caff} = 1.8\ s^{-1}$ yielding $k_{SERCA} = 1.9\ s^{-1}$ (Fig. 7*G*). Thus, the comparison shows that the model has a SR Ca^{2+} content in between the experimental data ranges whereas the SERCA pumping time is slower than most of the experimental values (Fig. 7*F*) but not too far from Voigt et al. and Fakuade et al.

Effect of stretch variation on AP and contractility

Using the MBS2023 model, we simulated the effect of stretch variations on AP, CaT and F_{active} characteristics under isometric conditions, where for a given SL the preload effect was varied using λ. We simulated the I_{sac} current, which is the combination of I_{ns} and I_{K0}, and varied λ from 1 (blue continuous line), 1.1 (red dashed line), 1.2 (yellow dotted line) to 1.3 (purple dotted-dashed line) as shown in Fig. 8. The raised preload effect elevates the SL (Fig. 8*A*) and demonstrates positive inotropic effect (Fig. 8*B*), which is the key depiction of the Frank-Starling law of the heart. In line with the observation of Tavi et al. (1998) for λ = 1.1, the rise in F_{active} was not due to the increased CaT in the bulk (as shown by red dashed line Fig. 8*D*) but is caused by the increased sensitivity of the contractile element to Ca^{2+} (red dashed line Fig. 8*C*). For λ = 1.2 and onwards, the relatively large rise in sensitivity of Ca^{2+}-TRPN bound results into an even more prominent rise in F_{active}. An elevated diastolic CaT level is also observed for λ = 1.2 onwards, which can be related to raised SR Ca^{2+} content with varying preload (not shown). For CaT and F_{active} biomarkers, a rise in systolic and diastolic levels is observed with a slight lengthening of time duration (T_{Ca} and TT). The stretch-induced rise in Na^{+} concentration modulates the inward I_{NaCa} component (as shown in Fig. 10*C*) in the early phase of the AP followed by a reduction in the later phase. The I_{sac} current shown in Fig. 8*E* demonstrates a combined effect of inward I_{ns} and outward I_{K0} currents. For λ = 1.1 (red dashed line, Fig. 8*E*), the I_{sac} current has more outward component and therefore the I_{K0} current affect on AP is dominant, i.e. shortening of APD (Fig. 8*F*, red dashed line). On the other hand, for higher λ (λ = 1.2,

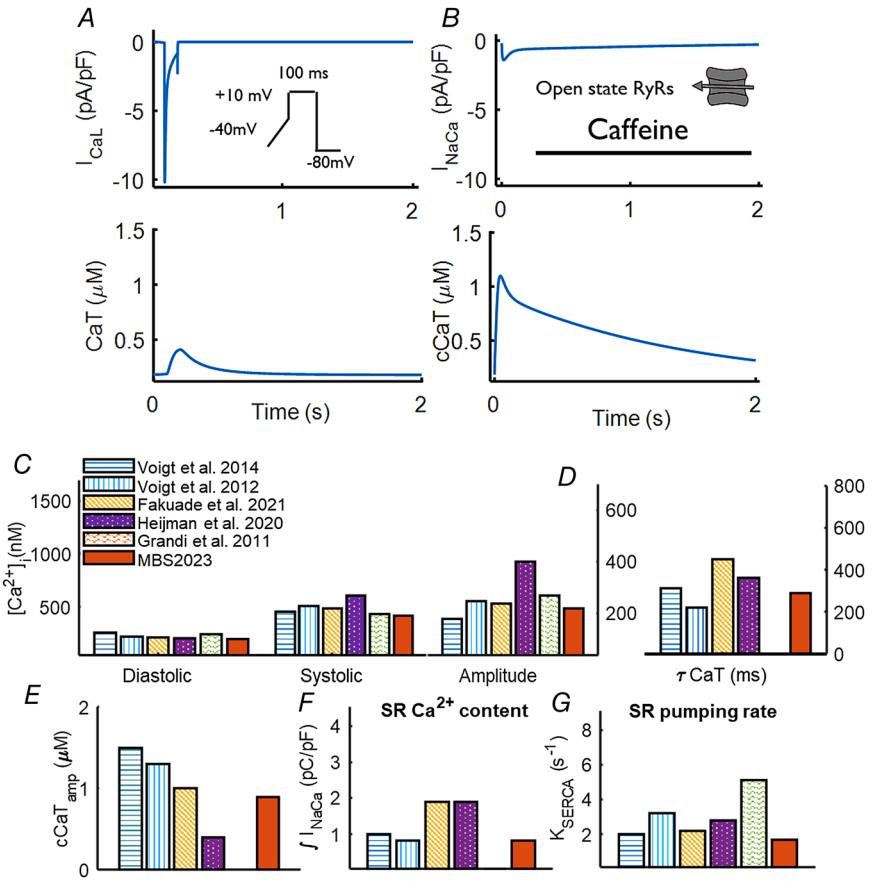

Figure 7. Validation of SR Ca^{2+} content and pumping rate in the MBS2023 model
A, the voltage clamp protocol (inset) resulting in I_{CaL} current (top) and I_{CaL} triggered Ca^{2+} transient (CaT) (bottom). *B*, the caffeine induced inward I_{NaCa} current (top) with CaT (cCaT) (bottom). The experimental data from bar plots extracted from Voigt et al. (2014) (blue horizontal lines), Voigt et al. (2012) (blue vertical lines), Fakuade et al. (2021) (yellow diagonal lines), Heijman et al. (2020) (purple dots), Grandi et al. (2011) (green curvy lines), and MBS2023 output (filled red bars). *C* shows the characteristics of I_{CaL} triggered CaT diastolic (left), systolic (middle), and amplitude (right). *D* shows the decay time constant for the CaT. *E*, the caffeine induced CaT amplitude. *F* and *G*, SR Ca^{2+} content is the integral of I_{NaCa} current under caffeine application and the k_{SERCA} is the measure of SERCA pump rate and is compared for the simulated output with the experimental data in panels *F* and *G*, respectively. [Colour figure can be viewed at wileyonlinelibrary.com]

yellow dotted line, and $\lambda = 1.3$, purple dotted-dashed line) the effect of I_{ns} predominates, as can be seen by the inward current and slow kinetics of I_{sac} current (Fig. 8*E*). As expected, for large λ ($\lambda = 1.2, 1.3$), the depolarization of RMP is more pronounced.

The reversal potential of I_{ns} lies near 0 mV (as shown in Fig. A7, red triangles) whereas the I_{K0} current has a potential quite close to the RMP. This can also be depicted from the time course for each current shown in Fig. A9E. Consequently, I_{ns} depolarizes the RMP of the AP with lengthening of late repolarization (APD_{90}) and no effect on the mid-repolarization phase (APD_{50}) (Fig. A9F on left). In contrast, I_{K0} has a slight shortening effect on the late repolarization phase of the AP (Fig. A9F on right). The combined effect of I_{sac} on AP is shown in Fig. 8*F*, where the shortening effect is predominant for smaller preload ($\lambda = 1.1$), and the depolarized RMP is observed for higher λ. Consequently, the depolarized RMP causes a 30% slowing of dV/dt_{max} at $\lambda = 1.2$ and will be discussed in detail in the Discussion section. The depolarization of RMP gets strengthened by increased conductance of g_{nsmax}, as shown in Fig. A10F where the basal state of the model (in yellow) at $\lambda = 1.2$ demonstrates another 41% slowing of dV/dt_{max} for a 50% rise in g_{nsmax} (in red). This conduction slowdown is usually found to be a consequence of acute atrial dilatation that can be considered vulnerable to AF (Ravelli et al., 2011).

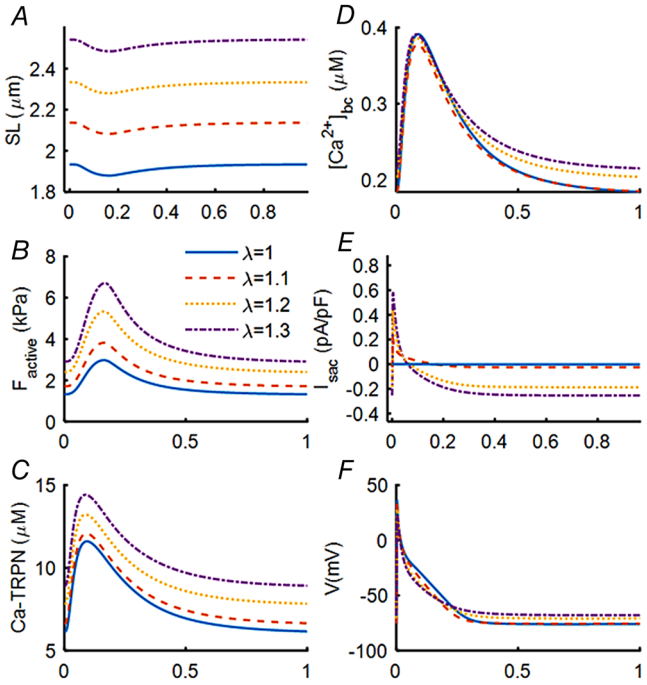

Figure 8. MBS2023 model characteristics for stretch variations λ from 1 (continuous blue line), 1.1 (red dashed line), 1.2 (yellow dotted line), and 1.3 (purple dotted-dashed line)
A, the raised level of contractile element length (SL). *B*, active contractile force (F_{active}). *C*, the concentration of Ca^{2+} bound to troponin (TRPN). *D*, Ca^{2+} transient in bulk cytoplasm (bc). *E*, stretch activated current I_{sac}, which is the sum of I_{ns} and I_{K0}, *F*, the action potential (AP). [Colour figure can be viewed at wileyonlinelibrary.com]

Rate adaptation of AP and contractility

An increase in pacing rate causes a physiological shortening of APD of atrial myocytes as quantified in various experimental studies (referred to in Table A4). We simulated the rate dependent behaviour of our model by running the model for a physiological range of BCLs (2, 1, 0.5, 0.33 and 0.283 s). AP curve rate dependence is shown in Fig. 9*A*. In addition, the APD_{90} shortening trend with BCL for a sparse set of *in-vitro* data is shown in Fig. 9*B* (continuous line). The relative change in APD_{90} for BCLs [2, 0.3] is −20% for the MBS2023 model and that gets increased to −28.8% under CaMKII inhibition (dashed line). Hence, the monotonically increasing activity of $CaMKII_{active}$ for the physiological range of frequency (0.5–3 Hz) plays its part in steep APD_{90} rate dependent shortening. Given the sparsity of the experimental data, we compared the data with the APD_{90} output normalized with respect to BCL = 1 s, as shown in Fig. 9*C* where the model output is quite within the range of the data spread.

The mechanism behind the APD_{90} shortening with rate is explained with the help of the ionic currents, which show substantial rate dependence, as shown in Fig. 9*D*–*H*: the inactivation of I_{CaL} reduces the plateau of the current (Fig. 9*D*) and has a time dependent recovery property that results in significant rate dependence and hence contributes to APD_{90} shortening which is pronounced only for longer BCLs (2–0.5 s) (Li et al., 1997). A parallel phenomenon of rate dependent Na^+ accumulation in the cytosol occurs in ventricular CMs (Harrison et al., 1995; Verdonck et al., 2004) and in atrial guinea-pig (Wang et al., 1993). The model shows a similar Na^+ accumulation (Fig. 9*G*, inset) which causes the enhanced pumping activity of Na^+/K^+ pump with rate. This increased pumping results in an increased outward current I_{NaK} (Fig. 9*E*) that links to APD_{90} shortening. Since I_{Kur} block can contribute to the positive inotropic effect, the rate dependent trend of I_{Kur} integral is analysed in Fig. 9*H* (lower panel), which showed a rate dependent reduction mainly because of the later decay phase of the current (Fig. 9*F*). Thus, reducing outward I_{Kur} is contributing to the accumulation of Ca^{2+} in the cytosol (Fig. 9*J*). During fast pacing, a combination of both Na^+ and Ca^{2+} (Fig. 9*G* and 9*I*) increases in the cytosol contributes to making the I_{NaCa} exchanger work more in reverse mode. In the model output, this is shown by the integral of I_{NaCa} normalized to BCL with the rate (Fig. 9*H*, top) decreasing or becoming more positive for shorter BCLs (after 330 ms) (Fig. 9*G*). The CaMKII inhibition effect on the integral of currents (Fig. 9*H*, dashed lines) reduces the I_{CaL} and I_{Kur} currents

for longer BCLs. For the I_{NaCa} integral, CaMKII inhibition shows a slight reduction in the overall current. Hence, a combined increase in outward I_{NaK} and I_{NaCa}, and a reduction in inward I_{CaL} currents is the major contributor of APD_{90} rate dependent shortening for the physiological range of BCLs.

The rate dependent behaviour of CaT in bulk cytosol and the F_{active} for our model is shown in Fig. 9*I–M*. The positive inotropic effect with a parallel rise in CaT with rate is observed in the *in-silico* model, as shown in Fig. 9*I*. Likewise, CaT time course shows a rise in both systolic and diastolic levels. The biphasic

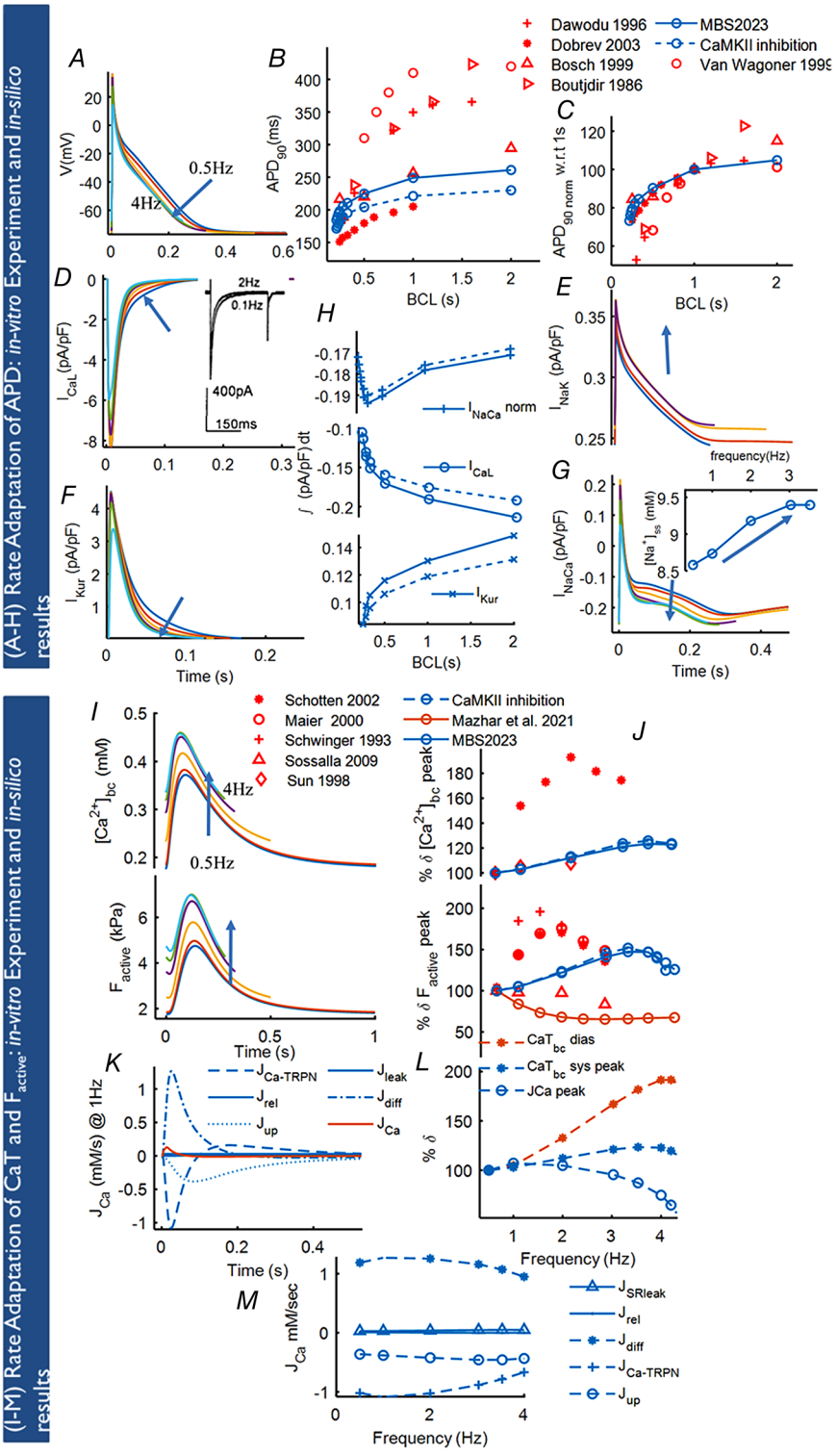

Figure 9. Rate adaptation response of MBS2023 and its dependence on CaMKII activity
A–H, rate dependence of AP and the cellular mechanism behind it. *A*, *in-silico* results of AP time course for each rate. *B*, APD_{90} shortening trend for the model (continuous line) with BCL compared to experimental data listed in Table A4 and CaMKII inhibition (dashed line). *C*, APD_{90} rate dependence normalized with respect to BCL = 1 s. *D*, I_{CaL} rate dependence in experiments (Li et al., 1997) (inset) compared with *in-silico* results. *E–H*, the mechanism of APD_{90} shortening. *E*, increasing I_{NaK} traces with rate. *F*, rate dependency of I_{Kur} current. *G*, increasing inward I_{NaCa} current traces with inset showing rate dependent Na^+ accumulation in the cytosol. *H*, rate dependent trend of the integral of I_{NaCa} (top) normalized with respect to the BCL, I_{CaL} (middle), and I_{Kur} (bottom) is shown. *I–M*, rate dependence of F_{active} and CaT and its cellular mechanism. *I, J, in-silico* results of CaT and F_{active} rate dependence as percentage change of CaT peak (top) and F_{active} peak values produced by the model in comparison to experimental data (references in Table A3) and CaMKII inhibition effect (dashed lines). *K–M*, the mechanism of CaT rate dependence. *K*, the comparison of magnitude and dynamics of inward fluxes to bc, diffusion from ss to bc compartment (J_{diff}) (dotted-dashed line), the SR release (J_{rel}) and leak (J_{SRleak}); and outward fluxes, SR uptake (J_{up}) (dotted line), $J_{Ca\text{-}TRPN}$ (dashed line) at 1 Hz frequency. The sum of all fluxes is J_{Ca} in red. *L*, rate dependence trend of CaT systolic (asterisks), diastolic (cross) and J_{Ca} (open circles). *M*, rate dependency of peak values of each flux using various markers, J_{diff} (asterisk), J_{up} (open circles), $J_{Ca\text{-}TRPN}$ (crosses), J_{SRleak} (triangles), J_{rel} (dotted).

percentage change of CaT peak in the bc compartment is compared with limited available data (Fig. 9*J*). Similarly, the percentage change of F_{active} is compared with human experimental data (references in Table A2) in Fig. 9*J* (bottom panel). The rate dependent shortening of F_{active} biomarkers normalized with respect to 1 Hz is shown in Fig. A2. Among the biomarkers, the late relaxation phase, i.e. rt_{90} shows a prominent rate dependency and model output is quite in line with the experimental data, as shown in Fig. A2. In contrast, the rt_{50} and ttp show a flat rate dependency. The cellular mechanism behind the rate dependence of CaT is explained in Fig. 9*K*–*M*). Following this, all the inward and outward fluxes in the bc compartment are compared (Fig. 9*K*) under steady state conditions and 1 Hz frequency. Hence, a difference in dynamics and amplitude of the inward fluxes, i.e. diffusion from ss to bc (J_{diff}), SR release in the bc (J_{rel}), and the SR leak (J_{SRleak}); and outward fluxes, i.e. SR uptake (J_{up}) from the bulk, Ca^{2+} bound to TRPN ($J_{Ca\text{-}TRPN}$) can be observed. J_{diff} shows a large peak comparable with $J_{Ca\text{-}TRPN}$ and followed by J_{up} whereas, minimum contribution is observed by J_{rel} and J_{SRleak}. In addition, flux $J_{Ca\text{-}TRPN}$ is the fastest followed by J_{diff} and J_{up}. The sum of all the fluxes is shown by J_{Ca} (in red) in Fig. 9*K*. J_{Ca} has fast dynamics and a depressed systolic level. The rate dependence of CaT systolic and diastolic values can be appreciated in Fig. 9*I* and is quantified, in terms of percentage in Fig. 9*L*. The progressive increase in diastolic $[Ca^{2+}]_{bc}$ is the main determinant for a consequent increase in the systolic $[Ca^{2+}]_{bc}$; however, a concurrent progressive decrease with rate of the net Ca^{2+} influx into the bulk cytoplasm, J_{Ca} (peak values) takes place, resulting in the overall biphasic rate dependence of the CaT systolic peaks. A further investigation behind this decreasing rate dependence of J_{Ca} is carried out by plotting the peak values of each flux with frequency as shown in Fig. 9*M*. The J_{diff} peak (asterisk) increases slightly at lower rates (up to 1 Hz) and then reduces progressively with the rate. On the other hand, the outward flux, J_{up} (open circle) shows a slight increase with rate till 4 Hz then a minute decrease, whereas a prominent decrease in $J_{Ca\text{-}TPRN}$ (plus) is observed with rate. Hence, the declining trend of diffusion with a parallel reduced amount of Ca^{2+} bound to TRPN at higher rate (after 3.5 Hz) gives rise to the biphasic decline of CaT in the bulk cytosol.

Effect of mechano-electric feedback on rate adaptation. We have analysed the effect of stretch variation via I_{sac} current, under isometric condition, on rate adaptation of APD and CaT where the rate varies from BCL = 2 to 0.283 s (Fig. 10). APD_{90} rate dependent shortening for varying λ from1 to 1.3 is shown in Fig. 10*A*. For λ = 1, the rate adaptation of APD_{90} (red dashed line) is quite overlapping with the basal state of the model (MBS2023, blue continuous line, Fig. 10*A*). When the stretch is increased, for λ = 1.1 (yellow dotted line, Fig. 10*A*), the APD_{90} demonstrates an overall shortening with a no sharp change in rate adaptation trend. With another rise in λ = 1.2, the APD_{90} rate dependence is flattened first for longer BCLs (from 2 to 1 s) and the

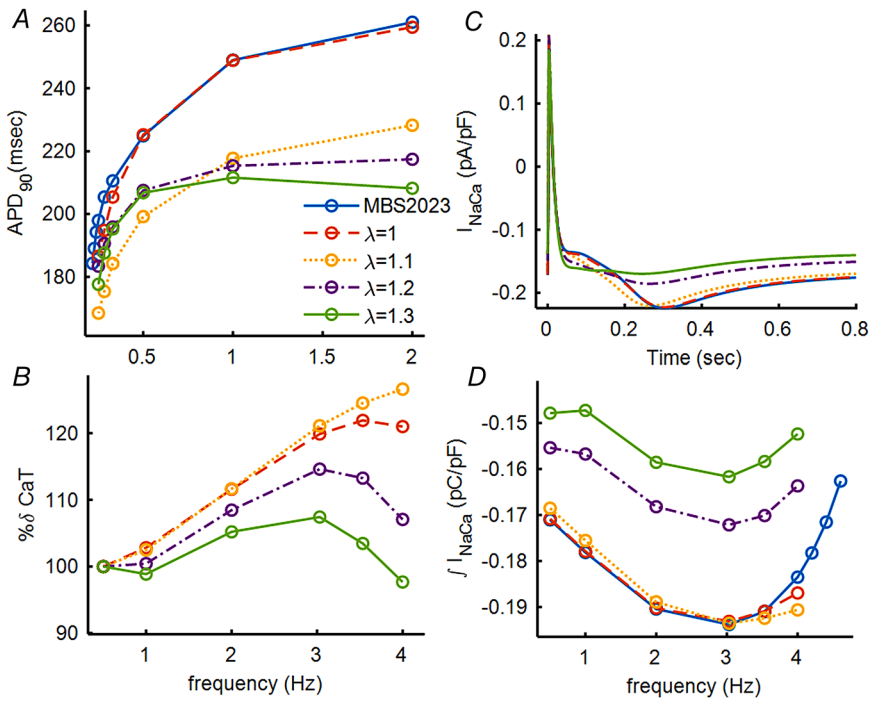

Figure 10. Stretch variation response on rate adaptation of APD and CaT
The model was compared under four different simulation settings: control condition as MBS2023 (blue continuous line), λ = 1 (red dashed line), λ = 1.1 (yellow dotted line), λ = 1.2 (purple dotted-dashed line), and λ = 1.3 (in green continuous line). *A*, the rate adaptation of APD_{90}; *B*, the rate dependence of percentage change of CaT systolic peaks; *C*, the time course of I_{NaCa} current; *D*, integral of I_{NaCa} current trend with rate normalized with respect to each BCL. [Colour figure can be viewed at wileyonlinelibrary.com]

trend gets reversed for higher stretch levels ($\lambda = 1.3$). In addition, the slope of APD_{90} rate dependence for shorter BCLs (0.5 onwards) was reduced equally for both $\lambda = 1.2$ and 1.3 (Fig. 10*A*). This can be a consequence of the exponentially rising I_{ns} current with λ. Hence, the overall depression of APD_{90} magnitude with rate is potentially due to the rise in the I_{K0} contribution to AP for lower λ ($\lambda = 1.1$ in Fig. 10*A*) and the change in slope of APD is because of the increasing role of I_{ns} with rising λ. Apart from this, the mechanical stretch increases the inward flow of Na^+ ions in the myocytes and, hence, can affect the operating modes of the Na^+/Ca^{2+} exchanger (I_{NaCa}). Accordingly, we analysed the time course of the I_{NaCa} current for a basal rate of 1 Hz (Fig. 10*C*) and the rate dependence of integral of I_{NaCa} current normalized with respect to its BCL (Fig. 10*D*) for all the conditions. Under basal conditions, the rate dependent Na^+ accumulation in the cytosol increases the inward flow of current up to BCL = 0.33 s (3 Hz in Fig. 10*D*) and then there is a shift to outward mode. For varying λ, the integral of I_{NaCa} trend shows a decrease in overall magnitude of the current with no striking change in the rate adaptation trend.

The rise in CaT systolic level can be related to the enhanced sensitivity of Ca^{2+}-TRPN binding, as was already shown in Fig. 8*C*. The rate dependent biphasic behaviour of percentage change in CaT_{peak} is shown in Fig. 10*B* (right) where under isometric mode of the model, it shows a rise in $[Ca^{2+}]_i$ up to 3.5 Hz and then a decline. The rate dependency of percentage change in CaT loses its biphasic trend for $\lambda = 1.1$, i.e. it always increases; however, with a rise in λ (1.2 and 1.3), the biphasic relation is restored at higher frequencies with a trade-off of some decrease in current at lower frequency (at 1 Hz). This trend can be related to the area of I_{NaCa} current normalized with respect to the BCL, as shown in Fig. 10*D*. The integral of I_{NaCa} at higher frequencies (from 3 Hz and onwards) showing a transition from the inward to the outward mode of the I_{NaCa} current at higher frequencies corresponds to the biphasic relation of CaT. The outward mode of I_{NaCa} allows the influx of Ca^{2+} that via diffusion enters the bc and enhances the SR Ca^{2+} storage, which can be shown by the elevated diastolic level of CaT at $\lambda = 1.2$ and onwards (as shown in Fig. 8*D*).

Effect of $[Ca^{2+}]_o$ variations

The evaluation of the Ca^{2+} handling mechanism underlying the intracellular Ca^{2+} homeostasis of the model was carried out by simulating the elevation of the extracellular Ca^{2+} concentration $[Ca^{2+}]_o$ from 0.9 to 3.2 mM. In line with experiments (Brixius et al., 1997) reported in Fig. 11*A* (left), the model reproduced the elevation of CaT and F_{active} systolic and diastolic levels, as shown in Fig. 11*B* (right top and bottom panels, respectively). The percentage change trend of systolic (triangles) and diastolic (open circles) for CaT (in red) and F_{active} (in blue) is shown in Fig. 11*B* (bottom). The diastolic rise is equivalent for both CaT and F_{active} whereas, the systolic level elevation is more pronounced than CaT for all $[Ca^{2+}]_o$ values. The comparison of the percentage rise in systolic peaks of CaT and F_{active} with experimental data is quantified in panel *C* (left panel). Consistent with experimental evidence, the model shows a significant percentage rise in F_{active} and CaT throughout the varying $[Ca^{2+}]_o$ and this increased more at 3.2 mM, where a 172% rise in F_{active} and 140% in CaT was achieved. Similarly, we compared the percentage change of kinetics of F_{active} using biomarkers $ttp_{Factive}$, $rt_{50Factive}$ and $TT_{Factive}$ for varying $[Ca^{2+}]_o$ in Fig. 11*C* (right panel): there is no substantial difference in the percentage changes of biomarkers for F_{active}, as can be seen in the experimental values.

The diastolic rise of CaT with elevated $[Ca^{2+}]_o$ can be speculated to be the result of more Ca^{2+} influx via Ca^{2+} channels in the subspace and less efflux either via SERCA activity or the I_{NaCa} exchanger current. Since the model lacks T-tubules, inside the bulk cytoplasm, the rise in Ca^{2+} influx is mainly due to a 175% increase in diffusion flux (J_{diff}) and slightly to a release flux (J_{relbc}), whereas, the extrusion of Ca^{2+} is dependent on SERCA uptake. Under $[Ca^{2+}]_o$ elevation, the model showed a 123% rise in SR Ca^{2+} content (not shown), thus also resulting in more Ca^{2+} bound to TRPN. Hence, these changes of intracellular CaT with varying $[Ca^{2+}]_o$ were accompanied by a rise in diastolic and systolic values of F_{active}.

Enhanced contractility by I_{Kur} blocking

The block of I_{Kur} is expected to prolong the AP plateau that will eventually lead to an increase in contractility. Accordingly, we analysed the blocking effect of I_{Kur} by setting the current conductance g_{Kur} to 100%, 80% and 20% of its regular value. In accordance with the experiments (Wettwer et al., 2004), the *in-silico* model reproduced a prolongation of the plateau phase, as shown in Fig. 12*A*. Moreover, a change of AP morphology from type 3 to type 4 (Dawodu et al., 1996) for human atria is also observed at a higher percentage (80%) of I_{Kur} block. The AP biomarker's response to I_{Kur} blocking is shown in Fig. 12 (right). AP biomarkers included APD at 20% and 30% of repolarization (APD_{20}, APD_{30}) and the plateau potential (PP) calculated as a mean voltage amplitude within a time window of 20–80 ms after the upstroke. In line with experiments (Wettwer et al., 2004), APD_{30} is prolonged from 8 to 105 ms and the plateau potential rises from −16 to +10 mV with the increasing block percentage of I_{Kur}. In contrast, we observed a lengthening of APD_{90}

in the model instead of a shortening as reported in the experiments (Wettwer et al., 2004).

The model also demonstrated the secondary effect of I_{Kur} blockage on AP. As a result, an increased amplitude of I_{CaL} current was observed at more positive AP potentials (Fig. 12*B*). Consequently, a large I_{CaL} activated more outward repolarizing currents like I_{Kr} (Fig. 12*C*) and I_{Ks} (not shown). The reduced activation of Na^+ channels results in a decreasing steady state Na^+ concentration in the cytosol. Similarly, we analysed the prolongation of the APD_{90} effect on I_{NaCa} current, as shown in Fig. 12*D*. The decrease in inward I_{NaCa} current during the early repolarization phase of AP (most dominant in the yellow line) is compensated by the increased current during the later AP phase. In other words, the integral of I_{NaCa} current (inset) does not show a large change even for a high percentage of I_{Kur} block, i.e. 80%. The positive inotropic response of our model is in line with human experimental results (Schotten et al., 2007) (Fig. 12*E*). The concentration dependent effect of I_{Kur} block (Kv1.5) by AVE0118 is modelled using the formulation by Decher et al. (2006). Based on this relation, our model showed good agreement (open circles) with the elevation of contractility caused by the various degrees of I_{Kur} block (Fig. 12*F*), as reported in experiments (open squares).

Simulation of impaired SERCA activity as a mechanism for post-operative AF

The simulation of PoAF associated pro-arrhythmogenic abnormalities can be analysed in the form of beat-to-beat oscillations in CaT and AP, i.e. alternans. The PoAF arrhythmogenic substrate was simulated by the depression of SERCA activity, expression and pumping rate (Fakuade et al., 2021). Following the experimental protocols, we simulated the model from 0.5 to 5 Hz of frequency and analysed the mechanism behind the incidence of CaT and AP alternans under control conditions and the shift in alternans threshold in the PoAF condition. Following the experimental results, the PoAF condition was simulated in the model by reducing the SERCA activity, i.e. the pumping rate to 70% and the expression levels, to 80%.

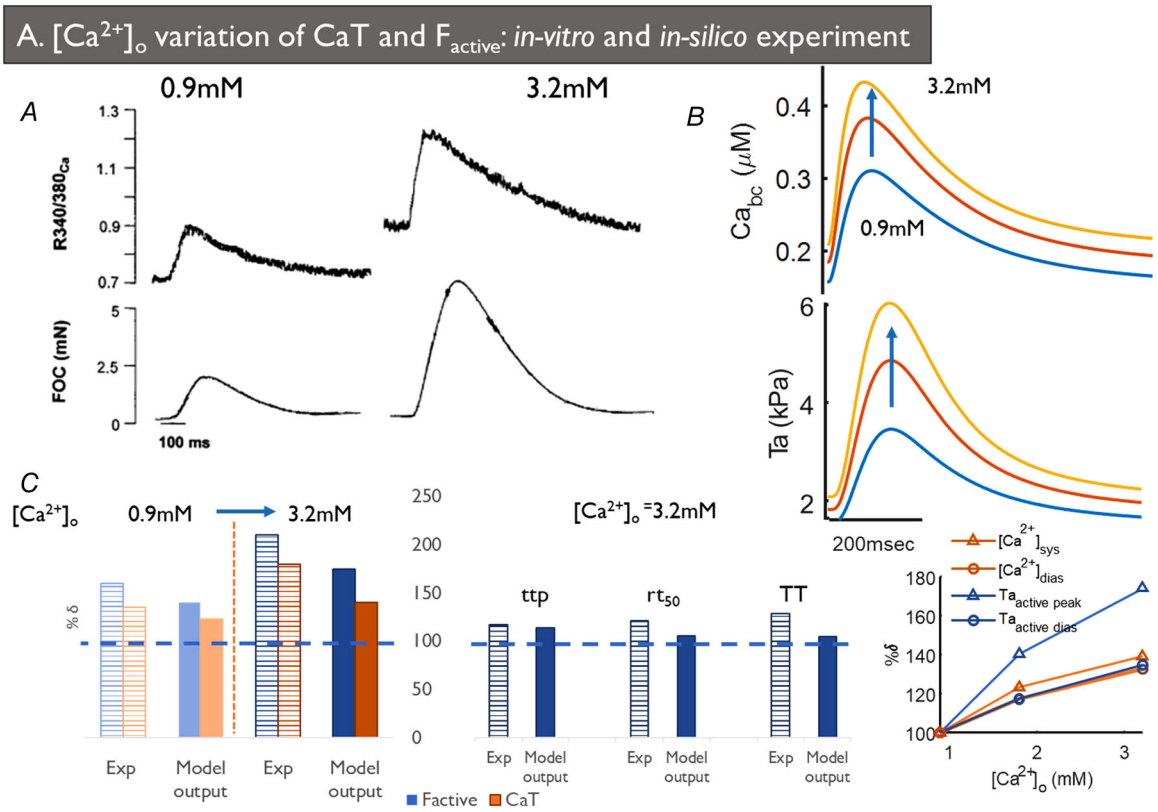

Figure 11. Extracellular Ca^{2+} ($[Ca^{2+}]_o$) variation effect on MBS2023
A, experimental data (Brixius et al., 1997) for CaT (fura-2 ratio) (top) and F_{active} elevation (bottom) with $[Ca^{2+}]_o$ compared with *in-silico* results of CaT (top) and F_{active} (bottom) time course. *B*, F_{active} and CaT biomarker response to $[Ca^{2+}]_o$ variations reproduced with MBS2023 model. *C*, left percentage change of systolic peaks of F_{active} (red bars) and CaT_{bc} (blue bars) compared with the experimental data for varying $[Ca^{2+}]_o$ from 0.9mM to 3.2mM. *C*, right, percentage change in the kinetics of F_{active} using biomarkers ttp, rt_{50}, and TT with same experimental data.

The onset of AP and CaT alternans at high frequency is observed by the biomarker bifurcation diagram, where the divergence point is the key indicator of alternans initiation, as shown in Fig. 13*A* and *B*. The biomarkers for AP are APD_{50} and APD_{90} (Fig. 13*A*), and for CaT the amplitude of CaT peaks at consecutive beats in bc (Fig. 13*B*, left) and ss (Fig. 13*B*, right) compartments. Hence, under control conditions (100% SERCA activity) (in blue), alternans both in AP and CaT appeared at a frequency of 4.6 Hz. In experiments (Fakuade et al., 2021), the threshold for AP and CaT alternans was shifted down to a lower frequency in the PoAF group. This alternans threshold shifting was demonstrated qualitatively by the model under the PoAF condition (in red). Hence, a higher susceptibility to AP and CaT alternans was found under PoAF, as the alternans threshold was shifted to 4 Hz. Furthermore, under PoAF, a reduced Ca^{2+} level is seen in the ss compartment (Fig. 13*B*, right) with respect to control (red *vs.* blue) with no change in bc CaT levels (Fig. 13*B*, left). The consecutive three beats, in terms of AP (first panel), CaT in ss (continuous line) and bc (dashed line) (second panel) and $[Ca^{2+}]_{SR}$ time course (third panel) evoked at 4.4 Hz under control conditions are shown in Fig. 13*C* and *D*. A similar plot of AP, CaT and $[Ca^{2+}]_{SR}$ under PoAF (Fig. 13*C* and *E*, in red) illustrates the beat-to-beat alternations in CaT systolic and diastolic levels both in ss and bc compartments (second panel) and in $[Ca^{2+}]_{SR}$ release and end diastolic value (third panel).

The mechanism for the onset of CaT alternans is investigated in Fig. 13*F* by plotting the three consecutive beats of RyR steady state inactivation gate for the ss compartment at 4.4 Hz for control (top panel, blue traces) and PoAF conditions (bottom panel, red traces). Under control conditions (Fig. 13*F*, top panel), the peak availability of RyR gate is about 14%, it is uniform all along the consecutive beats, and this gives a stable CaT in the subsequent beats (in light shading). In contrast, in PoAF (bottom panel), the model demonstrates

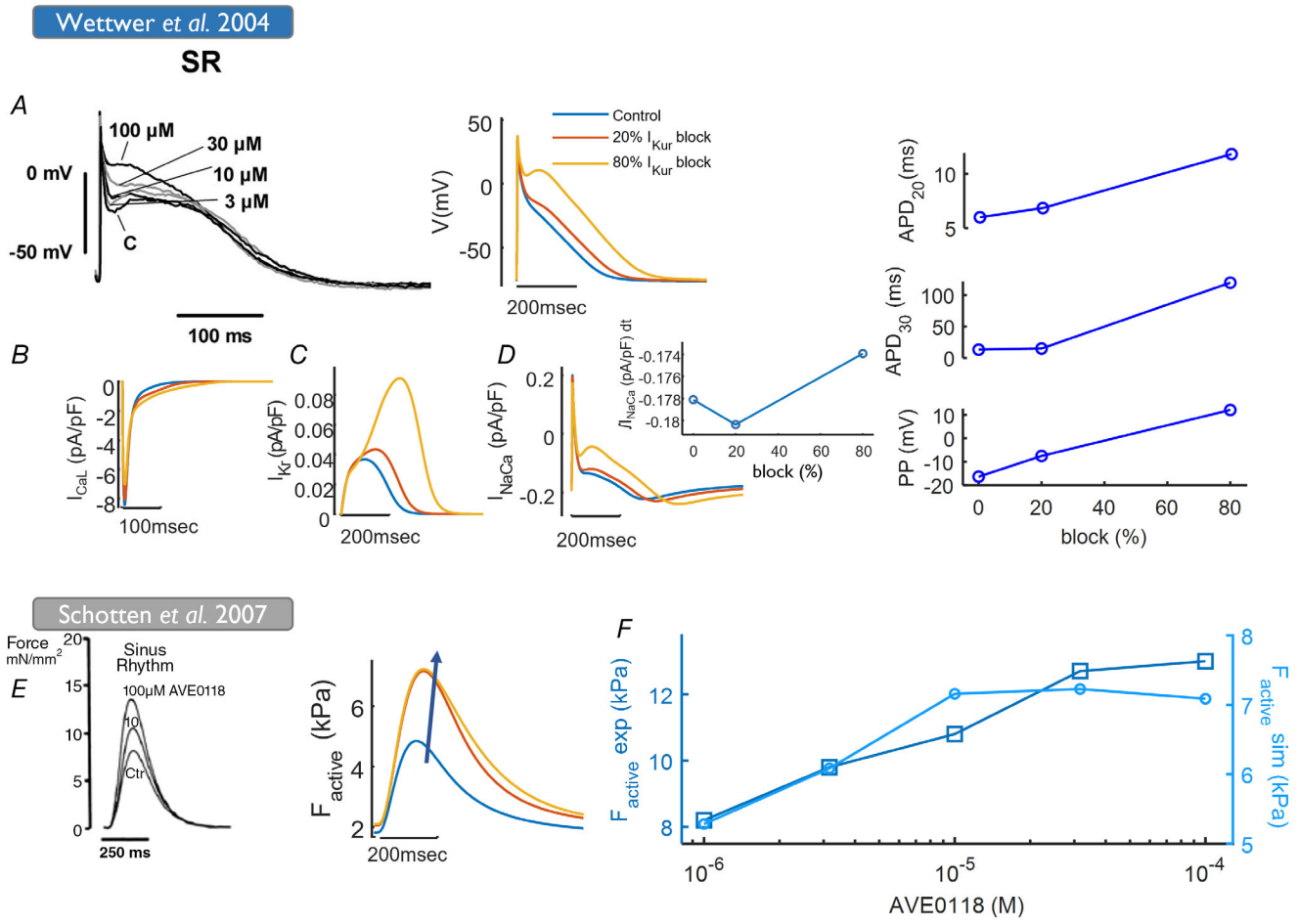

Figure 12. Effect of I_{Kur} blocker on MBS2023
A, *in-silico* results of I_{Kur} blocking on AP time course compared with *in-vitro* experiments (Wettwer et al., 2004). The AP biomarkers were shown, plateau potential (PP), $APD_{30,}$ and APD_{20} trend. Secondary effect of I_{Kur} blocking on I_{CaL} current (*B*), I_{Kr} current (*C*), and I_{NaCa} (*D*) with the integral (in the inset). *E* and *F*, the drug concentration dependent inotropic response of the model compared with experimental data (Schotten et al., 2007).

beat-to-beat alternations in RyR inactivation and recovery from inactivation time. The recovery from inactivation is not uniform from beat to beat, and as a consequence the availability of RyR gate alternates between 4% and 14%, resulting in short and long CaTs, respectively. Hence, the refractoriness of RyRs in the ss compartment is one of the mechanism of alternans incidence in the model under PoAF conditions.

Dissecting parameters involved in alternans development. With the help of a dynamic alternans pacing protocol, we have investigated the role of contraction, Ca^{2+} handling, and the CaMKII based phosphorylation effect on the model that can be appreciated by APD_{90}-ANM and CaT-ANM scores, as shown in Fig. 14, where the ANM threshold is set to 5% and is shown by the red dashed line. Under basal conditions, MBS model has a propensity to alternans incidence at a BCL of 200 ms where Ca alternans are stronger than APD, as shown by the ANM score (7.34% *vs*. 5.9% in red bars). Among the contraction related parameters, the slowing of transition rates K_{off} and K_{basic} did not play a significant role in strengthening the alternans magnitude. On the other hand, the reduced sensitivity of thin filament, i.e. increasing $k_{d\text{-}TRPN}$ results in enhancement of alternans more for CaT than APD (ANM scores: 12% *vs*. 9%) and the alternans completely vanished on decreasing $k_{d\text{-}TRPN}$. The parameter that has the greatest impact on CaT alternans magnitude is the coupling effect, i.e. MCF feedback as shown in Fig. 14. On reducing the Ca-TRPN binding (by 0.5 times), i.e. a weak MCF effect, the model demonstrated alternans with greater sensitivity to CaT oscillations than APD (ANM score: 13% *vs*. 10.01%). This major rise in ANM score is a consequence of the enhanced level of free CaT in the cytosol that is achieved because of the reduced concentration of Ca-TRPN bound in the model. Ca-TRPN has a dampening effect on the beat-to-beat oscillations that is even enhanced by increasing the Ca-TRPN binding affinity, as was seen already by reducing the $k_{d\text{-}TRPN}$ parameter.

Among the Ca^{2+} handling parameters, the slow inactivation of RyR release gates has slightly reversed the trend, i.e. this parameter is more vulnerable to APD alternans than CaT with ANM score of 9.2% *vs*. 8.78%. The enhanced SERCA activity is favourable for alternans vulnerability, as demonstrated by enhanced SERCA expression and pumping rate. The enhanced CaMKII effect protects the MBS2023 model against the

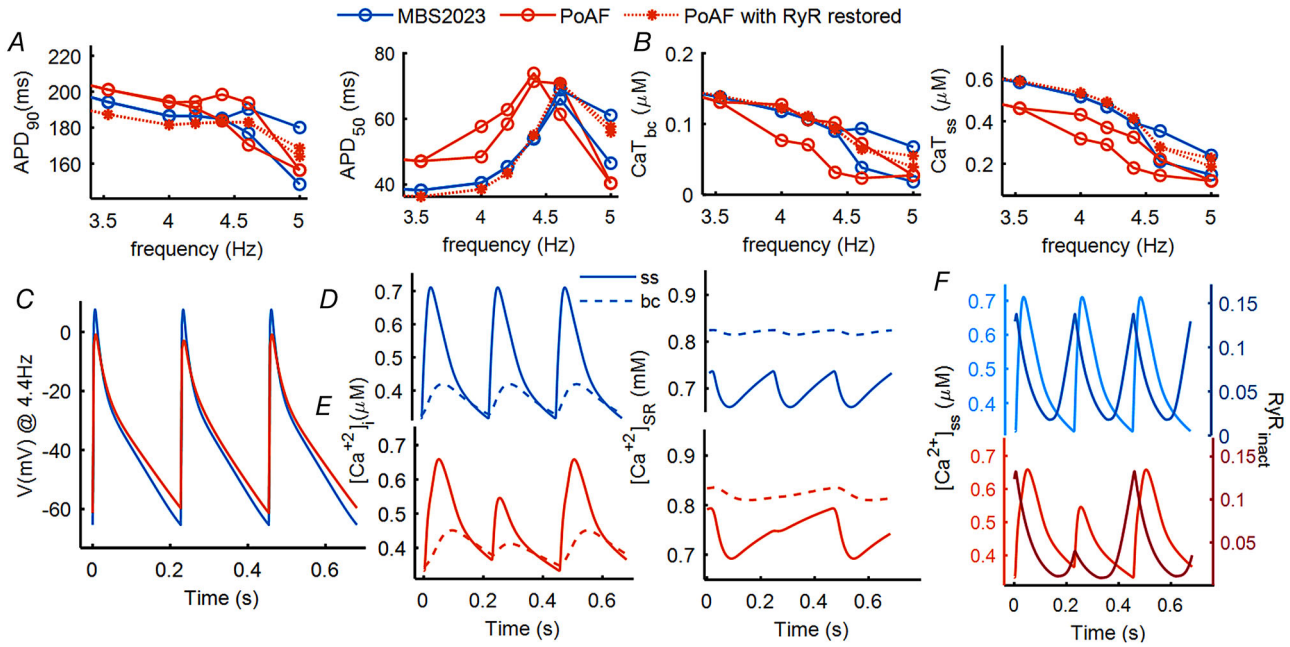

Figure 13. Effect of SERCA activity variation as a measure of PoAF condition on MBS2023 model
The SERCA activity was reduced from 100% (control in blue) to the PoAF condition induced by depressed SERCA, i.e. 80% reduced SERCA expression and 70% reduced pumping rate (PoAF in red), and under same PoAF conditions with RyR inactivation kinetics restored as was in KM2011 (in red asterisks). *A*, bifurcation diagram of AP biomarker (APD_{50}) (left panel), and APD_{90} (right panel). *B*, difference of CaT amplitude on the consecutive beats of CaT in bc (left panel) and ss (right panel) compartments at different frequencies. *C*, consecutive APs at 4.4 Hz under control (blue continuous line) and PoAF (red dashed line) conditions. *D* and *E*, consecutive CaTs in both compartments (left panels) and Ca^{2+} concentration in SR, $[Ca^{2+}]_{SR}$ (right panels) at 4.4 Hz in control (*D*) and PoAF (*E*) conditions. *F*, consecutive beats of RyR steady-state inactivation gate in comparison with CaT from ss compartment at 4.4 Hz under control and PoAF conditions.

incidence of alternans. The CaMKII expression reduction induces very strong alternans in APD with ANM 12.16% that is even greater than the CaT ANM magnitude (11.05%). Overall, the presence of a coupling MCF effect reduces the alternans induced vulnerability in the model, where the sensitivity of the thin filament is the key modulator of alternans development. In Ca^{2+} handling, enhanced SERCA activity and RyR slow inactivation times can play a role in increasing the alternans incidence probability in our model. The role of each parameter discloses some insight into mechanisms behind the alternans vulnerability, as will be explained further in the Discussion section.

Stretch strengthens the alternans susceptibility. Under isometric conditions, the MBS2023 model demonstrates increased vulnerability to alternans incidence when paced for higher rates, as shown by the bifurcation diagram in Fig. 15. The diagram demonstrates biomarkers for AP, APD_{90} (top left), and APD_{50} (bottom left) and for CaT amplitude both in bc and ss compartments. The stretch condition at $\lambda = 1.2$ under I_{sac} (red triangles) protects the model from both AP and CaT alternans development as was seen under control conditions (in blue). In contrast, the exclusion of outward I_{K0} from I_{sac} current resulted in an enhanced vulnerability to alternans development, as shown by the yellow cross in Fig. 10. This shifts the alternans threshold from 4.6 to 3.5 Hz and strengthens the magnitude of oscillations (shown by increased opening of the branches) for both AP and CaT biomarkers. The exclusion of I_{K0} removes the shortening effect of APD and, hence, susceptibility to alternans incidence.

The mechanism behind the stretch induced alternans incidence at BCL 0.283 s (3.5 Hz) can be seen in Fig. 16 under $\lambda = 1.2$ with I_{sac} (continuous blue line) and with I_{ns} only (red dashed line). In the basal state of the model, one of the mechanisms of alternans incidence was the time constant of the RyR inactivation gate which determines the availability of the RyRs. Here, the alternans appeared at 3.5 Hz (instead of 4.6 Hz as in the basal model), hence resulting into more availability (18%) of RyRs for $\lambda = 1$ (Fig. 16*G*). On increasing the preload $\lambda = 1.2$, the recovery from inactivation is not uniform from beat to beat, and consequently the availability of RyR gate alternates between 24% and 11%, resulting in short and long CaTs, respectively (Fig. 16*E*). Other than this, the stretch induced rise in alternans magnitude can be associated with Ca^{2+}-TRPN concentration (Fig. 16*D*). As shown before, I_{ns} current increases the binding affinity of Ca^{2+}-TRPN which gets amplified by the I_{ns} only condition

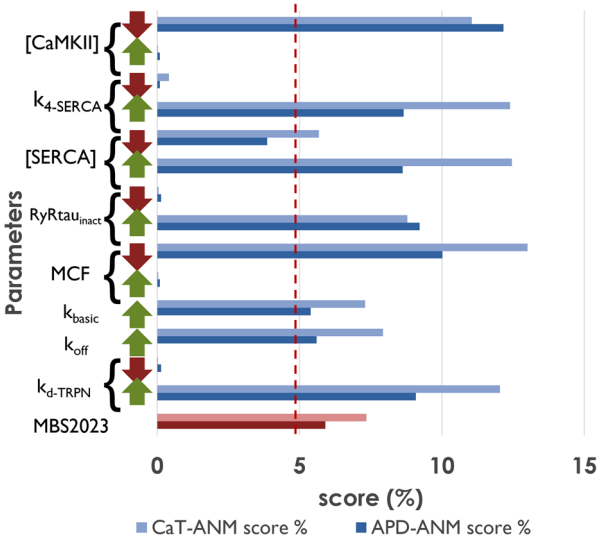

Figure 14. Effect of parameter variations on alternans normalized magnitude (ANM) for CaT_{peak} (CaT-ANM) (in light shading) and APD_{90} (APD-ANM) (in dark shading)
All the parameter values were varied by increasing 2-folds and reducing 0.5-fold. Parameters related to Ca^{2+} handling: RyR inactivation time ($RyR_{tauinact}$), SERCA activity, i.e. expression level ([SERCA]), pumping rate ($k_{4\text{-SERCA}}$); the feedback: mechano-calcium feedback (MCF) induced by Ca^{2+}-TRPN binding; Contraction: thin filament transition rate (K_{off}), sensitivity ($k_{d\text{-TRPN}}$), and cross-bridge cycling (XBcy) rate (K_{basic}); CaMKII: expression ([CaMKII]). [Colour figure can be viewed at wileyonlinelibrary.com]

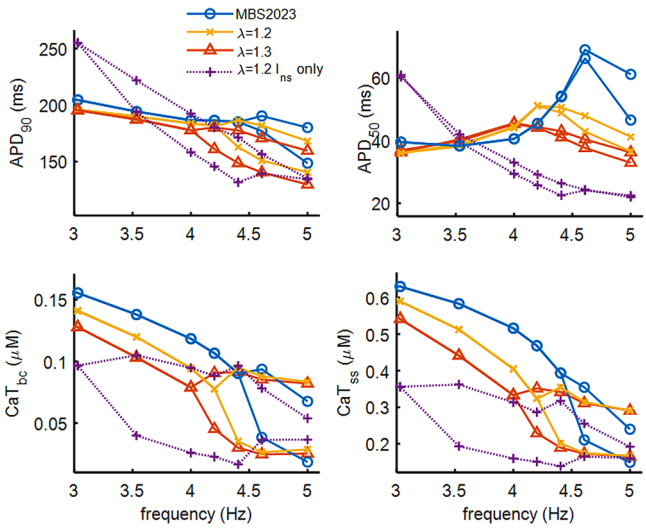

Figure 15. Bifurcation diagram illustrating the comparison of the basal condition of the model MBS2023 (in blue), with conditions under $\lambda = 1.2$ I_{sac} current (yellow crosses), $\lambda = 1.3$ (red triangles), and $\lambda = 1.2$ for I_{ns} only (purple crosses)
The divergence of the bifurcation branch is a key indicator of alternans incidence in AP biomarkers, APD_{90} (top left), APD_{50} (bottom left), and CaT amplitude in bulk cytosol (bc) (top right) and the subspace (ss) compartments (bottom right). The alternans magnitude is increasing with increased level of stretch. [Colour figure can be viewed at wileyonlinelibrary.com]

(Fig. 16*B* and *C*). For the $\lambda = 1.2$ I_{ns} only condition, for the long beat (Fig. 16*B*, red dashed line), the raised diastolic level of Ca^{2+}-TRPN concentration at the end of the BCL indicates that not all the Ca^{2+} is released from the TRPN buffer, showing that the sarcomere was not fully relaxed during the diastole. This increased activation of TRPN buffer during the subsequent short beat increases the fraction of bound Ca^{2+}-TRPN, which strengthens the cooperative activation of neighbouring regulatory units resulting in a stronger binding affinity. Thus, an increased Ca^{2+}-TRPN fraction will release a small CaT, resulting in a relative beat-to-beat oscillatory mechanism.

Discussion

We have developed a novel mathematical model that integrates the MER loop with feedforward, the EM coupling and the feedback pathways, via the MCF and MEF. The model couples one AP module, the modified KM2011 (Koivumäki et al., 2011), with a contractility module, RDQ2020 (Regazzoni et al., 2020). Despite the simplification induced in the AP module, the model is capable of preserving the characteristics of centripetal Ca^{2+} diffusion from the membrane to the bulk.

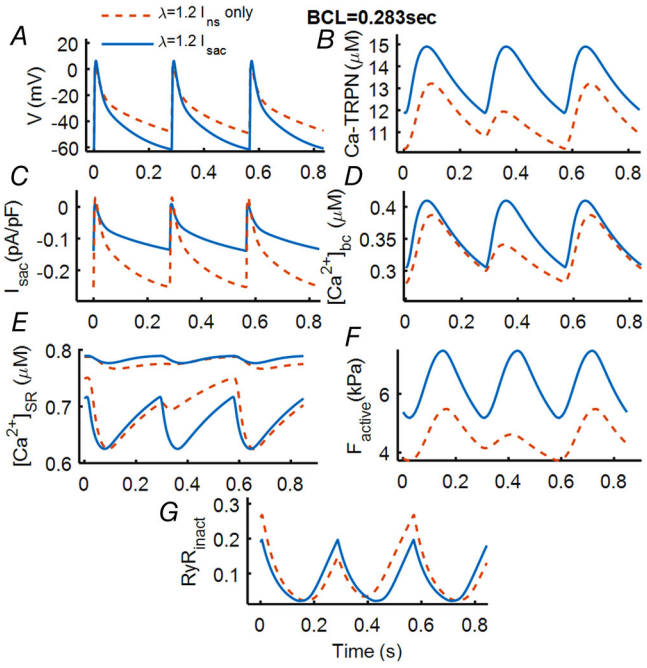

Figure 16. Beat-to-beat oscillations appeared at BCL = 0.238 s under no preload λ = 1 (continuous blue lines) and with preload λ = 1.2 (dashed red lines) conditions
A, action potential (AP); *B*, non-selective cation stretch activated current (I_{ns}); *C*, SR Ca^{2+} content; *D*, amount of Ca^{2+} bound to troponin (TRPN); *E*, Ca^{2+} transient in subspace ss (large amplitude) *vs*. in bulk cytosol (bc) (small amplitude); *F*, active force (F_{active}); *G*, the steady state inactivation gating variable of RyR_{ss}. [Colour figure can be viewed at wileyonlinelibrary.com]

AP and CaT characteristics of the model and the *in-vitro* data

The modifications introduced into the KM2011 model resulted in a type-3 AP morphology of human atria, which has a more prominent plateau phase than the parent model. In other words, we achieved an APD_{50} that is more in agreement with the mean human *in-vitro* data; nevertheless, a high level of AP shape heterogeneity has been reported in human atria (Colman et al., 2013; Feng et al., 1998) as reflected in our data collection in Table 2. Of note, the APD_{50} obtained from the model is in close agreement with the value for type-3 AP morphology reported by Dawodu (Dawodu et al., 1996). Likewise, the model was able to reproduce faster systolic Ca^{2+} rise and longer Ca^{2+} decay (in the bc compartment) than those of the contraction force, hence having a longer time course than the twitch time (Fig. 4*F* (inset)), in agreement with the observation made by Brixius (Brixius et al., 1997). Moreover, a quantitative analysis of this phenomenon based on the biomarkers ttp and rt_{50} for F_{active} and and rt_{50} for CaT_{bc} resulted in agreement with their experimental data ranges (Table 2). In particular, the CaT produced by the model has slower dynamics than the parent model (Fig. 4*C*) and than the defined experimental data range. On dissecting the decay phases, the model produced a CaT characterized by an early decay phase (rt_{50Ca}) within the physiological data range (Table 2 and Fig. 4) followed by a slower later decay phase (TT_{Ca} in Table 2). The slow dynamics of decay in the later phase usually depend more on the kinetics of Ca^{2+} removal from the cytosol than the buffering effect (Smith et al., 2019). In our model, the efflux of Ca^{2+} from the bc compartment is carried out by SR Ca^{2+} uptake since the exchanger and sarcolemmal pump are localized in the ss compartment. The uptake flux (J_{up}) dynamics in bc compartment was quite slow and small in magnitude (Fig. 8*L*). This was also evident when comparing the SR pumping rate (K_{SERCA}) with experimental data, as shown in Fig. 7*G*. This demonstrates a need for for further investigation of the Ca^{2+} efflux mechanism in the bc of the developed model.

Atrial stretch enhances the vulnerability to arrhythmias

Experimental evidence indicates that I_{ns} current plays a role in promoting arrhythmias in intact human atrium (Bode et al., 2000), in rat atrial tissue (Tavi et al., 1996), and in human atrial myocytes (Kamkin et al., 2003). Consistently, at basal frequency of 1 Hz, the rise in stretch (for I_{ns} only) lengthens the AP with a depolarized RMP in our model (Fig. A9, left panels). In the rat atria, a similar lengthening of APD was demonstrated under the moderate level of stretch applied during the AP diastole (Tavi et al., 1998). In contrast, a

shortening of APD was also reported in guinea-pig atria, although the mechanical stimulus was applied during the mid-repolarization phase (Nazir & Lab, 1996). In experiments, the electrophysiological response to stretch is dependent on timing of the stretch with respect to the AP dynamics. In our model the reversal potential of the I_{ns} current is near 0 mV and hence the model showed a lengthening effect. The depolarization of RMP resulted in decreased membrane upstroke velocity (dV/dt_{max}) that was slowed down by 30% for $\lambda = 1.2$. The sensitivity analysis of g_{ns} current shows an additional 41% slowdown of dV/dt_{max} for a 50% rise in g_{ns} (red line, Fig. A10). The reduction of cell excitability is associated with the macroscopic mechanism of reduced conduction velocity (CV) observed in acutely dilated human atrium (Ravelli et al., 2011). Accordingly, to have a better connection between micro-scale stretch ratio variation effect and macro-scale cell excitability, we simulated a 1D-discrete tissue level experiment for varying λ as shown in Fig. A6. For a 20% stretch rise ($\lambda = 1.2$), the 30% percentage change in dV/dt_{max} in an isolated cell (red asterisk) can be translated into 10% slowing of CV in the 1D-tissue (blue asterisk, Fig. A6). These results qualitatively agree with the findings of Ravelli et al., where for a 23% increase in atrial volume a 17% slowing of CV was found (Ravelli et al., 2011).

At basal rate, the varying length elevated the systolic and diastolic levels of the CaT with slight lengthening of the total transient duration. The systolic peak of CaT is highly dependent on the amount of Ca^{2+}-TRPN bound. Increasing length induces small increments in the CaT amplitude and more substantial ones in the amount of Ca^{2+} bound to TRPN. Moreover, the role of individual I_{sac} currents means that I_{ns} current formulation is more sensitive to changing λ than I_{K0} current (Fig. A9D). In other words, given no rise in CaT peak for I_{K0} current (right panels) for $\lambda = 1.3$ in purple dotted-dashed line, the rise in F_{active} (Fig. A9B) is because of increased sensitivity of the thin filament. In contrast, in the presence of I_{ns} current (left panels), the increased CaT peak (for $\lambda = 1.2$, yellow dotted line) combines with an increased affinity for bound Ca-TRPN (Fig. A9C) to elevate F_{active} (Fig. A9B). This result is consistent with experiments by Tavi et al. in rat atrial myocytes (Tavi et al., 1998) highlighting Ca^{2+} systolic rise and Ca^{2+} buffering by TRPN as the major modulators of the contractile force. The enhanced sensitivity of Ca^{2+}-TRPN binding can be explained by the length-dependent increase of contraction (Lookin et al., 2021). The study relates the extent of the length dependent activation with both peak systolic CaT and its decaying kinetics. At higher rates (3.5 Hz and above), the stretched sarcomeres reduced the alternans incidence threshold under control conditions from 4.6 to 3.5 Hz. These findings are quite similar to those from Tsai et al. (2011), who showed increased alternans vulnerability at BCL 250–67 ms for a longer SL. Therefore, atrial stretch is a important modulator of alternans development and can be considered as a potential therapeutic target to reduce the propensity for arrhythmia in patients with AF.

In our contraction module, as in experiments, the EC_{50} value of force-pCa curve is a linear inverse function of increasing SL while varying the SL within the physiological range. Hence, the length dependent decrease in EC_{50} (or increased sensitivity of Ca^{2+} binding to TRPN) results in increased bound Ca^{2+} in the cytosol in spite of quite similar levels of free Ca^{2+}. This length dependent rise in Ca^{2+} bound to TRPN is further amplified once translated into active force (Fig. 8). The model was also able to predict the secondary effects of MEF. First, the decrease of I_{CaL} in both peak and plateau phases (not shown); the increasing calcium dependent inactivation (CDI) effect, because of increasing J_{relss} peak (not shown), is the main modulator of I_{CaL} inactivation with stretch. On the other hand, Na^+ accumulation due to stretch increased the inward I_{NaCa} current at basal rate (Fig. 10*C*). Under increasing stretch, the combination of increased inward I_{sac}, reduced I_{CaL} and increased I_{NaCa} inward component resulted in the lengthening of APD_{90}.

Rate dependent modulation of MBS2023 and comparison with *in-silico* studies

Computational modelling and simulation are powerful tools for accelerating the mechanistic understanding of ionic mechanisms of the heart and eventually the whole heart. For human atrial myocytes, the CRN (Courtemanche et al. 1998) and Nygren (Nygren et al., 1998) models were the pioneer *in-silico* models, with a detailed description of ionic membrane currents and different descriptions of CaT dynamics, as reviewed by Cherry (Cherry et al., 2008). However, neither model was able to reproduce slow Ca^{2+} wave-like diffusion towards the centre of the cell, and experimental phenomena like a correct rate dependence of CaT, as shown in our previous work using the CRN model (Mazhar et al., 2021) and in Fig. 9*J* (red line). The rate dependent trend of APD_{90} and CaT for the CRN model can be seen in Fig. A8 (blue dashed lines). Later, KM2011 was proposed as the model with a detailed Ca^{2+} wave 'fire-diffuse-fire-propagation' mechanism. However, the model showed quite different results for Ca^{2+} rate dependence when compared with the dome shaped experimental trend (Fig. A8, blue dotted lines). One explanation could be that the Ca^{2+} homeostasis validity of the model was confined to a basal frequency of 1 Hz only. Among the existing human atrial computational models, the one by Grandi et al. (2011) demonstrated a positive CaT rate dependency (Fig. A8, blue dotted-dashed line). However, the rate dependence trend for APD_{90} was compromised at lower BCL (also

reviewed in Dössel et al., 2012). In contrast, MBS2023 adapted the Ca^{2+} handling formulations from KM2011 and calibrated them for a set of physiological pacing rates, i.e. 0.5 to 3 Hz. Moreover, the inclusion of the MCF effect resulted in a more physiological shape of CaT and therefore of the F_{active} dynamics, as quantified by ttp and rt_{50} biomarkers.

Our model reproduces the APD_{90} rate dependence as shown by the APs within type-3 AP morphology (Fig. 9*B*). In line with experimental findings (Dawodu et al., 1996), for longer BCLs (2 to 1 s), our model shows a less steep APD_{90} rate dependence, whereas for shorter BCLs (0.5 s onwards) the trend gets steeper, with decreasing BCL increasing rate. We analysed the ionic rate dependent mechanisms underlying APD rate dependency. We observed that the rate dependence of I_{CaL} inactivation results in a decreasing inward current with BCL (Fig. 9*D*). The effect of rate dependent reduction in I_{CaL} current on APD_{90} was quantified by blocking the current by 50% as shown in Fig. 17 (blue dashed line on the left). Block of I_{CaL} results in a flat APD_{90} rate dependency for BCL [2,1] similar to what was observed by Wagoner et al. by the application of 10 μM nifedipine (Van Wagoner et al., 1999), as shown in Fig. 17 (left in green markers). This was further confirmed by the observation made by Li et al. on human atrial myocytes, where the reduction of I_{CaL} was dominant for higher BCLs (0.5 to 2 s) (Li et al., 1997). Another test was to clamp $[Na^+]_{ss}$ to its steady state value and quantify the impact on rate adaptation of APD_{90} and CaT_{bc} as shown in Fig. 17 (dotted line). $[Na^+]_{ss}$ clamp was similar to I_{CaL} block; however, its effect was dominant from BCL 2 to 0.5 s. Thus, a combination of 50% I_{CaL} block and $[Na^+]_{ss}$-clamp (dotted-dashed line) was simulated that reversed the shortening of APD_{90} for BCLs 2 to 0.33 s to give a lengthening effect. Since I_{Kur} demonstrates rate dependency for the physiological range (Fig. 9*F*), we therefore made a test by blocking 50% of the current (dashed red line). Block of I_{Kur} can enhance the plateau of the AP, hence resulting in more activation of I_{CaL} current, which eventually leads to a reverse rate dependent APD_{90} trend, i.e. lengthening effect with rate. This was also observed in experiments blocking I_{Kur} with Acatein (10 μM) (Li et al., 2008). I_{Kur} block gives a similar response to the 50% I_{CaL} block + $[Na^+]_{ss}$-clamp experiment though the latter reduced the overall APD_{90} magnitude whereas the former enhanced it considerably. In other words, the magnitude and rate dependency of the current integrals I_{CaL} and I_{NaCa} (Fig. 9*H*) were reduced for combined 50% I_{CaL} block + $[Na^+]_{ss}$-clamp simulation test, and were enhanced for the 50% I_{Kur} block test. For the 50% I_{Kur} block test, the increased activation of I_{CaL} results in a large I_{NaCa} current with its reverse operating mode switched at BCL 0.5 s, which is the major player behind the rate adaptation of the APD trend under I_{Kur} block. Overall, for longer BCLs, I_{CaL} reduction was a dominant mechanism of APD_{90} shortening, whereas for shorter BCLs a combined increase in outward I_{NaK} pump and reverse mode of the I_{NaCa} exchanger currents resulted in a steep APD_{90} rate dependence.

As a result, our model shows an increase in CaT and F_{active} peaks with rate (Fig. 9*J*) up to 3.5 Hz and then a small decline afterwards. Experimental data for this rate dependence are quite sparse, making a close fit between the experimental data and the model results meaningless. Rather our focus was to investigate the mechanisms that give rise to biphasic rate dependence of the CaT. Therefore, we performed a detailed analysis of the inward and outward Ca^{2+} fluxes to/from the bc compartment and their rate dependence and quantified the contribution of each flux at each increasing rate. The major source of Ca^{2+} accumulation with rate is the prominent rise of diastolic Ca^{2+} (see Fig. 9*M*) because less time is available for its complete removal from the bulk. The Ca^{2+} efflux is mainly dependent on J_{up}, whereas transient sequestration of Ca^{2+} by $J_{Ca\text{-}TRPN}$ during the systolic phase strongly modulates the CaT peak, as is also shown by simulations in which the MCF is absent (Fig. 6). An increasing Ca^{2+} content in SR with the rate (from 0.615 to 0.821 mM for frequencies

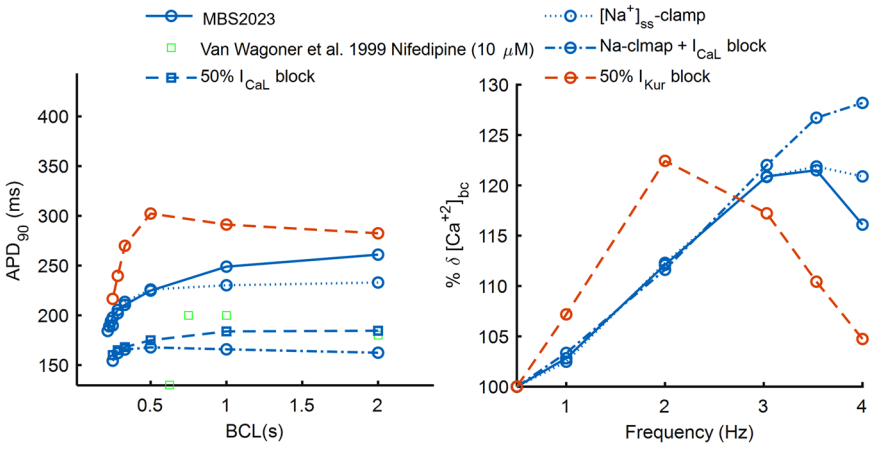

Figure 17. Effect of blocking each mechanism involved in APD (left) and percentage change of CaT_{bc} (right) rate dependency
MBS2023 original rate dependence (continuous line) is compared with I_{CaL} block by 50% (squares–dashed line), $[Na^+]_{ss}$-clamp (dotted line), combination of I_{CaL} block and $[Na^+]_{ss}$ clamp (dashed-dotted line), and I_{Kur} 50% block (red dashed line). The experimental data (Van Wagoner et al., 1999) depicts the APD_{90} rate dependency on applying the calcium channel blocker nifedipine (10 μM) (green open squares). [Colour figure can be viewed at wileyonlinelibrary.com]

of 1 to 4.5 Hz) is shown by the model and it qualitatively matches experimental evidence (Maier et al., 2000) from human atrial myocytes. An increasing $[Ca^{2+}]_{SR}$ might produce an increasing J_{rel}; however, the model produced a J_{relbc} with a very small amplitude that always decreased with rate. The main reason lies in the refractoriness of RyR gate that resulted in unavailability of fully activated RyR channels with increasing frequency. On the other hand, J_{relss} has faster dynamics then J_{relbc} and demonstrates a biphasic behaviour with increasing rate (not shown) that impacts on J_{diff} rate dependency. Consequently, J_{diff} peak increases slightly at lower rates (up to 2 Hz) and then reduces progressively with rate. On the other hand, after 2 Hz, a reduction in outward flux $J_{Ca\text{-}TPRN}$ (asterisks in Fig. 9*M*) was observed with a very slight contribution of J_{up} (open circle in Fig. 9*M*). Hence, this balancing of Ca^{2+} fluxes was observed at each frequency; therefore, inward flux was dominant till 3.5 Hz after which the outward flux dominated.

Inotropic effect of I_{Kur} blocking

I_{Kur} block enhances the atrial AP plateau, which can be therapeutically beneficial for treating atrial contractile dysfunction (Schotten et al., 2007), thus reducing the AF burden in persistent AF (Ford et al., 2016) and chronic AF (Wettwer et al., 2004) groups. In accordance with the experiments, the model can reproduce and explain the positive inotropic response on I_{Kur} block (Fig. 10). The elevated plateau potential and duration predicts secondary effects of I_{Kur} block on membrane currents like increases in I_{CaL} and I_K (I_{Ks} and I_{Kr}) currents. On the other hand, the model also produces a contradictory result, i.e. a lengthening of APD_{90} instead of a shortening as reported in human atrial myocytes (Wettwer et al., 2004). The reason for this discrepancy lies in the low maximal conductance value of I_{Kr} current present in our AP module, which was adopted from the parent model. Indeed, KM2011 inherited that conductance value from the Nygren model, which was shown to have a very small I_{Kr} with respect to CRN (Cherry et al., 2008). A detailed calibration of I_{Kr} formulation for human atrial myocytes will be the objective for future developments of our model. Therefore, the overall effect of I_{Kur} block was a prolongation of APD_{90}. In addition, the type-3 AP morphology has no substantial effect on APD_{90} with I_{Kur} block; it still produces an increase in contractility, as observed by Schotten in canine myocytes (Schotten et al., 2007). Based on these observations, the model predicted that a strong positive inotropic effect is not dependent on the late repolarization phase of the AP, whereas the AP plateau phase is crucial for this phenomenon.

Depressed SERCA activity can affect the alternans threshold

Reduced atrial contractile function is a predictor of PoAF (Fakuade et al., 2021). Based on this fact, it was observed experimentally that SERCA activity reduction was the only mechanism of impaired Ca^{2+} handling in a PoAF patient group. Based on this observation, we simulated the SERCA activity when reduced to 75% and analysed the set of mechanisms underlying the onset of alternans in the model (Fig. 11). The model produced alternans at 4 Hz under PoAF but not under control conditions. In our model, under PoAF conditions, due to SERCA depression, the removal of calcium from the cytoplasm and refilling of SR between two successive releases is slowed down (Fig. 11*D* and *E*). As a consequence, the diastolic value of Ca^{2+} in ss is relatively high, keeping it in a range for which recovery from inactivation of RyRs is very small. In this condition, the amount of available RyRs at the beginning of two successive releases can change a lot (more than doubled, from 0.024 to 0.058, in Fig. 11*E*). In other words, the 'gain' of the feedback loop into the intracellular calcium handling system is very high, and this gives rise to oscillations/alternans. Ca^{2+} dependent channels and transporters control the translation of beat-to-beat alternans in CaT into AP shape. Therefore, CaT is the driving mechanism of AP alternans, as demonstrated by comparing the APD_{50} as a measure of AP alternans. Hence, under PoAF, reduced SERCA activity results in the slowing of J_{up}, which can promote alternans even at modest SR loads and small release, consistent with the results found in rabbit atrial myocytes (Shkryl et al., 2012). Consequently, the slow uptake results in less Ca^{2+} J_{rel} flux and the small release with slow recovery kinetics contributed to moving the alternans threshold down to 4 Hz under PoAF conditions, which matches the findings of human atrial myocytes (Llach et al., 2011).

We have also observed, under MEF conditions, that alternans incidence was demonstrated at 3.5 Hz, as shown in Fig. 15 (yellow crosses). Similarly, the dynamic alternans protocol simulation results show that parameters like CaMKII overexpression, reduced SERCA pumping rate, fast $RyRtau_{inact}$, and the increased Ca^{2+}-TRPN sensitivity factor protect the model from alternans vulnerability, whereas the weak MCF condition can enhance it. In principle, CaMKII inhibition should suppress abnormal increases in activity of the RyR inactivation gate, providing a possible strategy to protect against alternans incidence. Nevertheless, the suppression of RyR activity can result in an increased propensity for Ca^{2+} alternans because of the prolongation of RyR refractoriness, as was seen experimentally in isolated mice

ventricular myocytes (Saderdini et al., 2021). Therefore, the development of alternans incidence in the model highlights the role of possible chains of mechanisms involved. In addition, the PoAF condition simulated in the model is based on one mechanism, i.e. depressed SERCA activity and we speculate that other mechanisms are also involved, as was observed by Van Wagoner et al. (1999), who showed that a g_{CaL} percentage raised to 50% was the main mechanism in the patients who developed PoAF condition. This point was also discussed in the work of Fakaude et al. and no clear reason for this discrepancy was found. Thus, we have observed alternans threshold shifting in the model that is a qualitative representation of Fakaude et al.'s experiments.

Limitations

We have presented a fully integrated human atrial model that highlights novel insights into various physiological mechanisms. For model parameterization and evaluation (Fig. 6), we utilized extensive human-specific independent atrial datasets to generate human-specific results and conclusions that are highly translatable. Nonetheless, lack of data availability or large variability in available datasets introduces some uncertainty. As a relevant example, the experimental data available on CaT biomarkers in humans show a high level of variability due to the differences in dyes and temperature used. In addition, the mechanical conditions under which the CMs are tested also differ substantially, and the available data for atrial human CMs are also quite limited. While the model captures the CaT characteristics, the systolic and diastolic levels and rt_{50Ca} well, it produces a slow TT_{Ca} and therefore a slow twitch time. A possible reason behind this could be the delayed efflux of Ca^{2+} from the bulk, which is solely based on J_{up}. However, the small amount of data on Ca^{2+} kinetics in human atrial myocytes limits the robustness of the comparison. The rate dependent trend for CaT and F_{active} fits qualitatively with the dome shaped experimental data shown. Potential parameters and mechanisms were highlighted; however, we were not able to obtain the right rate dependency for all the characteristics of the model since we have to deal with so many parameter calibrations at a time. In future, further optimization and validation of the presented biomarkers will be performed as new data becomes available.

It is known that T-tubules also exist in atrial myocytes (Richards et al., 2011) and the transverse-axial tubule system can play an important role in modulating intracellular calcium handling and, therefore, electro-mechanical coupling. The inclusion in the model of these aspects is beyond the scope of the present work and will be addressed in future developments focusing on pathological conditions.

Conclusions

In this work, we have presented a new electro-mechanical model for human atrial cardiomyocytes along with mechano-electric regulation. The model was developed, calibrated and evaluated against a wide range of *in-vitro* data. We found that our physiologically accurate description of Ca^{2+} handling can reproduce many experimental phenomena and help us to gain insights into the pathophysiological mechanisms. This computationally efficient and coupled model opens new pathways for future multi-scale modelling and investigation of human atrial electromechanics.

Appendix 1: Modified model equations

The model equations are based on KM2011 and RDQ2020 models. Here we list all those that have been modified or added.

Volume of cytosolic region

$$V_{\mathrm{bc_{Total}}} = \sum_{i=1\ to\ 4} V_{\mathrm{bc_i}},$$

where V_{bc1}-V_{bc4} refers to the volume of four bc compartments in KM2011 model and $V_{\mathrm{bc_{Total}}}$ is the total volume of the bc compartment in MBS2023.

Volume of SR compartment

$$V_{\mathrm{SRss}} = 2.25\% \left(V_{\mathrm{ss}} + V_{\mathrm{bc4}}\right),$$

$$V_{\mathrm{SRbc}} = 2.25\% \left(\mathrm{sum}\left(V_{\mathrm{bc1}} : V_{\mathrm{bc3}}\right)\right).$$

Intracellular free Ca^{2+} concentration

$$\frac{\mathrm{dCai_{bc}}}{dt} = \mathrm{beta_{nj}} \frac{JCa}{V_{\mathrm{bc_{Total}}}}.$$

Addition of dynamic troponin effect, $\frac{d[Ca^{2+}]_{TRPN}}{dt}$, in $[Ca^{2+}]_i$:

$$\frac{\mathrm{dCai_{bc}}}{dt} = \mathrm{beta_{bc}} \frac{JCa}{V_{\mathrm{bc_{Total}}}} - \frac{d\left[Ca^{2+}\right]_{\mathrm{TRPN}}}{dt}.$$

Free Ca^{2+} in SR

$$\frac{\mathrm{dCa_{SR_{ss}}}}{dt} = \mathrm{beta_{SR_{ss}}} \left(\mathrm{DCa_{SR}} \left(\frac{-\mathrm{Ca_{SR_{ss}}} + \mathrm{Ca_{SR_{bc}}}}{dx^2} + \frac{\mathrm{Ca_{SR_{ss}}} - \mathrm{Ca_{SR_{bc}}}}{2\left(4dx^2\right)}\right) + \frac{J_{\mathrm{SRCa_{ss}}}}{V_{\mathrm{SR_{ss}}}}\right),$$

$$\frac{\mathrm{dCa_{SR_{bc}}}}{dt} = \mathrm{beta_{SR_{bc}}} \left(\mathrm{DCa_{SR}} \left(\frac{\mathrm{Ca_{SR_{ss}}} - \mathrm{Ca_{SR_{bc}}}}{dx^2} + \frac{\mathrm{Ca_{SR_{ss}}} - \mathrm{Ca_{SR_{bc}}}}{2\left(3dx^2\right)}\right) + \frac{J_{\mathrm{SRCa_{bc}}}}{V_{\mathrm{SR_{bc}}}}\right).$$

I_{Na} current modified as shown,

$$E_{Na} = \frac{RT}{F}\ \log\left(\frac{Na_o}{Na_{ss}}\right),$$

$$m_\infty = \frac{1}{1+\exp((V+36.3)/-7.8)},$$

$$h_\infty = \frac{1}{1+\exp\left(\frac{V+67}{5.6}\right)},$$

$$m_{tau} = 0.00001 + 0.00013\exp\left(-\left(\frac{V+48}{15}\right)^2\right) + \frac{0.000045}{1+\exp((V+42)/-5)},$$

$$h\,1_{tau} = 0.00007 + \frac{0.034}{1+\exp((V+41)/5.5)} + \exp\left(-\frac{V+41}{14}\right) + \frac{0.0002}{1+\exp(-(V+79)/14)},$$

$$h\,2_{tau} = 0.0007 + \frac{0.15}{1+\exp((V+41)/5.5)} + \exp\left(-\frac{V+41}{14}\right) + \frac{0.002}{1+\exp(-(V+79)/14)},$$

$$I_{Na} = g_{Na}\ mh1h2\,(V - E_{Na}).$$

Appendix 2: Figures

L-type Ca^{2+} current reformulation

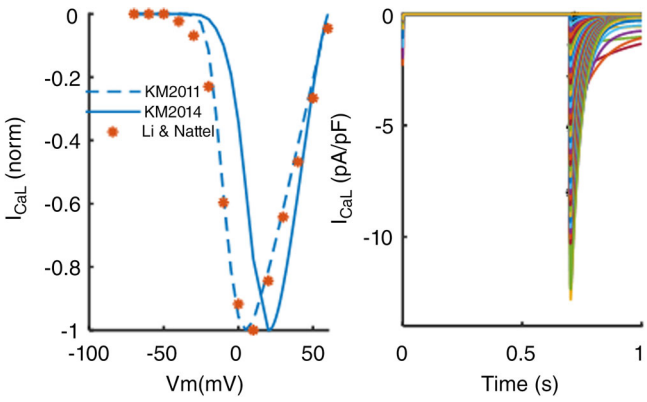

Figure A1. Voltage clamp protocol reproduced from Li & Nattel (1997)
Left panel shows *I-V* plot for two different formulations, i.e. the modified KM2011 used by MBS2023 (dashed line) and the KM2014 (continuous line) in comparison to the experimental data points. [Colour figure can be viewed at wileyonlinelibrary.com]

Rate dependent characteristics of contractility biomarkers

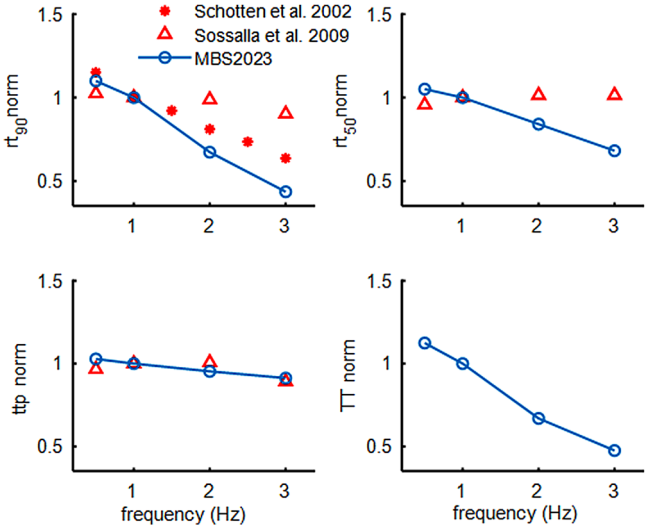

Figure A2. Rate dependent characteristics of F_{active} biomarkers
The experimental data reported are from Table A2 and are normalized with respect to 1 Hz frequency. Relaxation kinetics at 90% and 50% of the peak (rt_{90} and rt_{50}) are shown in top left and right panels, time to peak (ttp) in the bottom left panel and the twitch time TT is shown on the bottom right panel. [Colour figure can be viewed at wileyonlinelibrary.com]

MBS2023 model ionic currents, Ca^{2+} handling and CaMKII inhibition

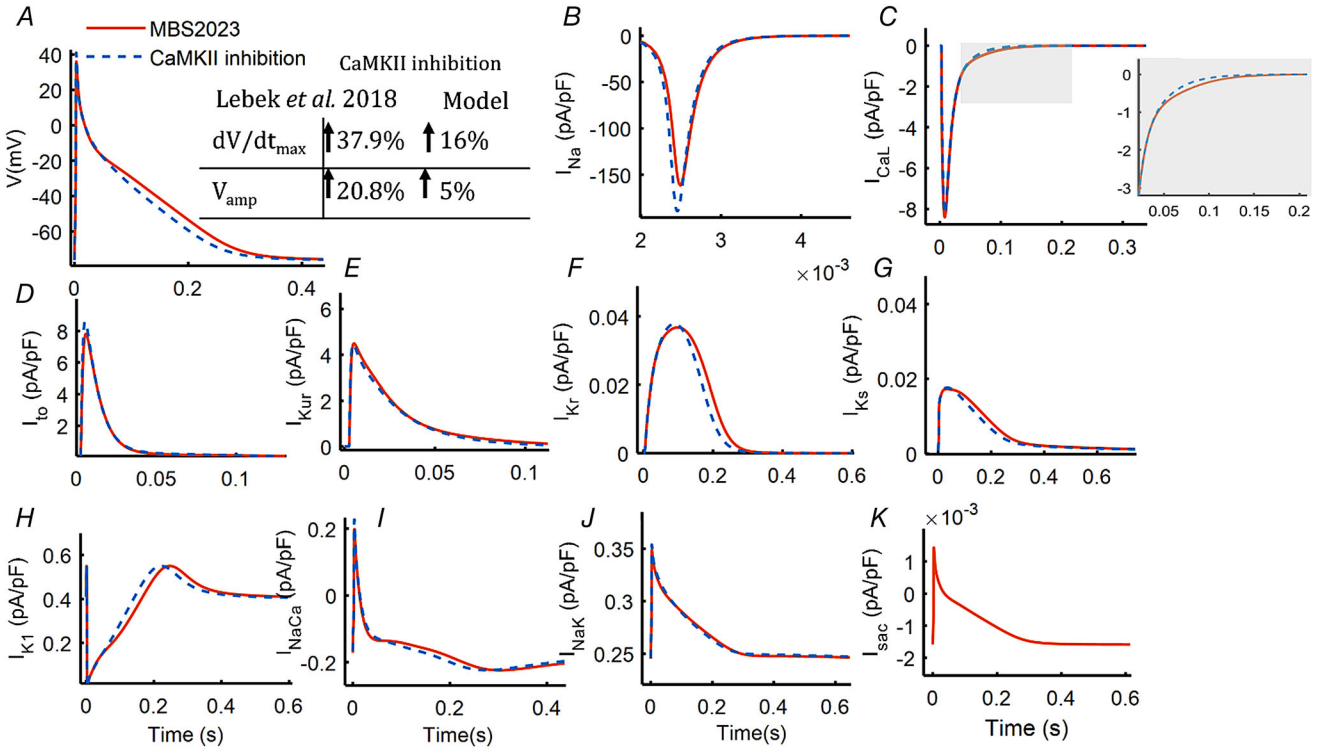

Figure A3. Steady-state human atrial AP, major membrane currents at 1 Hz basal frequency in comparison with CaMKII inhibition (blue dashed line) in MBS2023 (red continuous line)
A shows the AP morphology for MBS2023, table in the inset illustrates relative percentage change in V_{amp} and dV/dt_{max} from Lebek et al. (2018) in comparison to the model output. *B* and *C* show the fast I_{Na} and the I_{CaL} current with magnified plateau region of I_{CaL} in the inset. *D* and *E* show the phase 1 repolarizing currents I_{to} and I_{Kur}. *F*, *G* and *H* show I_K currents for phase 2 repolarization, i.e. I_{Kr}, I_{Ks}, and I_{K1}. *I* shows the stretch activated current I_{sac}. *J* and *K* represent the exchanger I_{NaCa} and the pump currents I_{NaK}. [Colour figure can be viewed at wileyonlinelibrary.com]

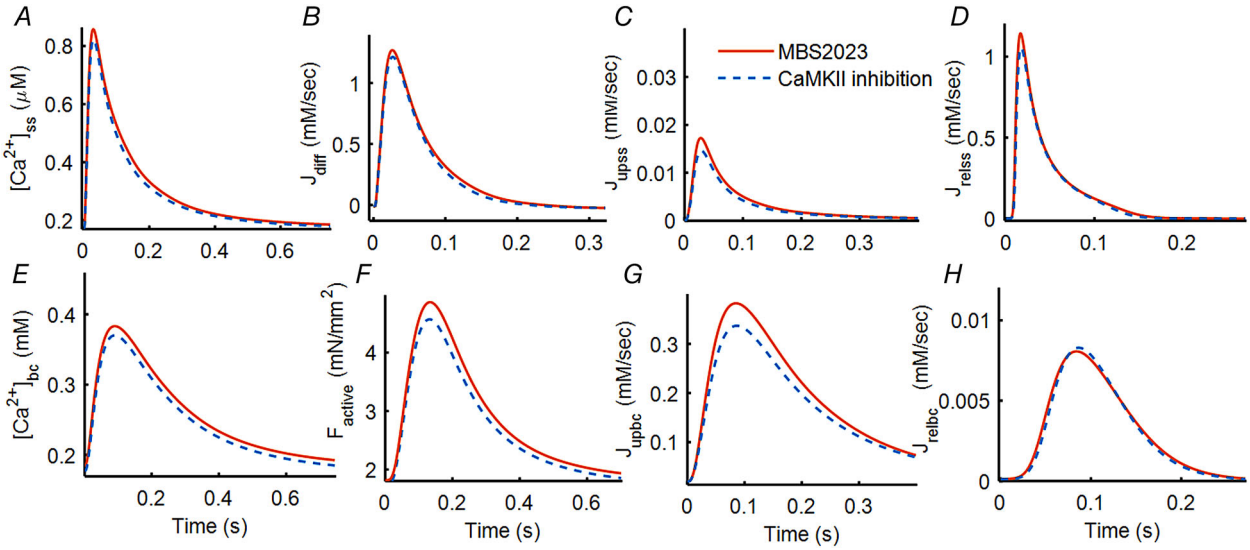

Figure A4. Ca^{2+} handling in MBS2023 model (red continuous line) in comparison with CaMKII inhibition (blue dashed line)
A, Ca^{2+} transient in the ss compartment. *B*, diffusion from ss to bc (J_{diff}). *C*, uptake flux via SERCA pump (J_{upss}). *D*, release flux (J_{relss}). *E*, slow and smaller Ca^{2+}-transient in the bc. *F*, F_{active} produced. *G*, uptake flux (J_{upbc}). *H*, small release flux (J_{relbc}). [Colour figure can be viewed at wileyonlinelibrary.com]

Non-selective stretch activated current

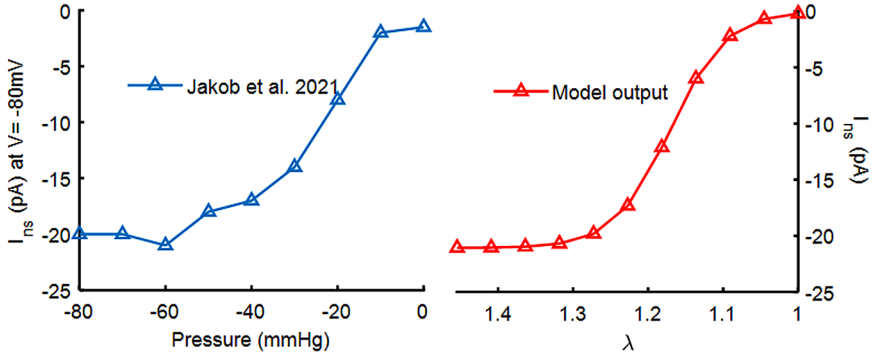

Figure A5. Validation of non-selective stretch activated current
Non-selective cation ion stretch activated current (I_{ns}) (model output in red on right) validated against the average-currents for all negative pipette pressures tested (from 0 to −80 mmHg) for 110 cells obtained from Jakob et al. (2021) (in blue on the right). [Colour figure can be viewed at wileyonlinelibrary.com]

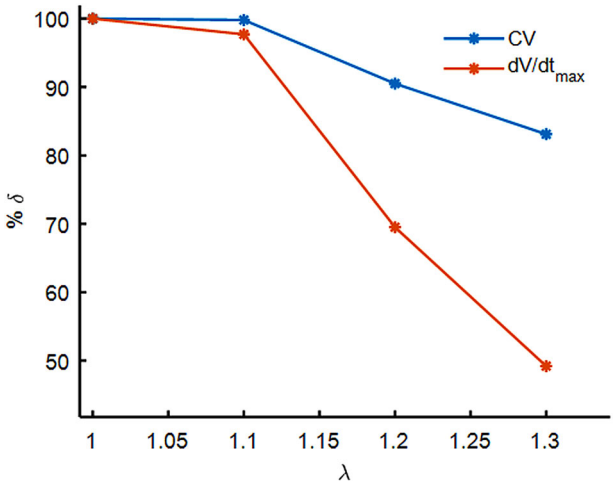

Figure A6. Shortening effect of stretch ratio λ on cell level parameters
The maximal shortening velocity (dV/dt_{max}) is shown in red and the tissue level parameter, the conduction velocity (CV) is shown in blue. The 1D-discrete tissue level simulation was carried out by connecting 40 cells, with gap junctional resistance (R_{gap}) 1.5 MΩ, for 10 beats using stimulation current of 5.06 nA. The CV was calculated based on the propagation time between cell number 8 and cell number 16. [Colour figure can be viewed at wileyonlinelibrary.com]

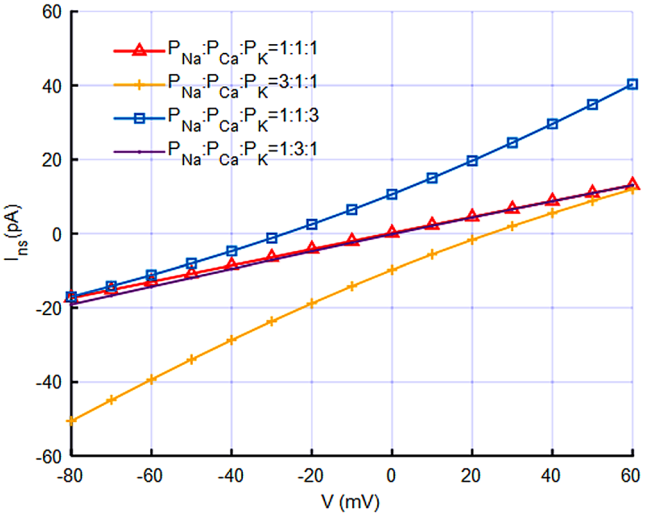

Figure A7. *I-V* plot for non-selective stretch activated current I_{ns} for λ = 1.1
Shown are plots for equal permeability ratio (red triangles), P_{Na} increased 3 times (yellow crosses), P_K increased 3 times (blue squares), and P_{Ca} increased by 3 times (purple dots). [Colour figure can be viewed at wileyonlinelibrary.com]

Comparison with in-silico models

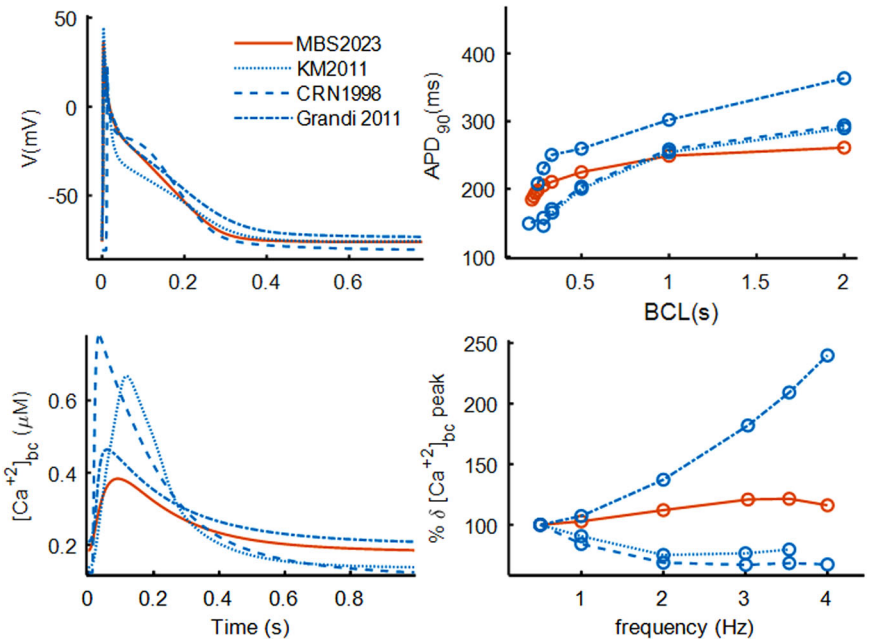

Figure A8. Comparison of human atrial computational models characteristics with MBS2023 for basic cycle lengths ranging from 2 to 0.25 s
The Courtemanche (CRN) 1998 model is shown in blue dashed lines, the Grandi, 2011 model in blue dotted-dashed lines, and the Koivumaki (KM) 2011 model in blue dotted lines. The MBS2023 model is shown in red continuous lines. Action potential (AP) morphology is shown in the top left panel, AP duration at 90% of repolarization (APD_{90}) rate adaptation in the top right panel, Ca^{2+} transient (CaT) time course in the bottom left panel, and rate dependency of percentage change in CaT (%δCaT) in the bottom right panel. KM2011 demonstrated an irregular waveform at 4 Hz, hence its simulation value is not shown in the top and bottom right panels. [Colour figure can be viewed at wileyonlinelibrary.com]

Effect of non-selective (I_{ns}) and potassium-selective (I_{K0}) cation currents on MBS2023

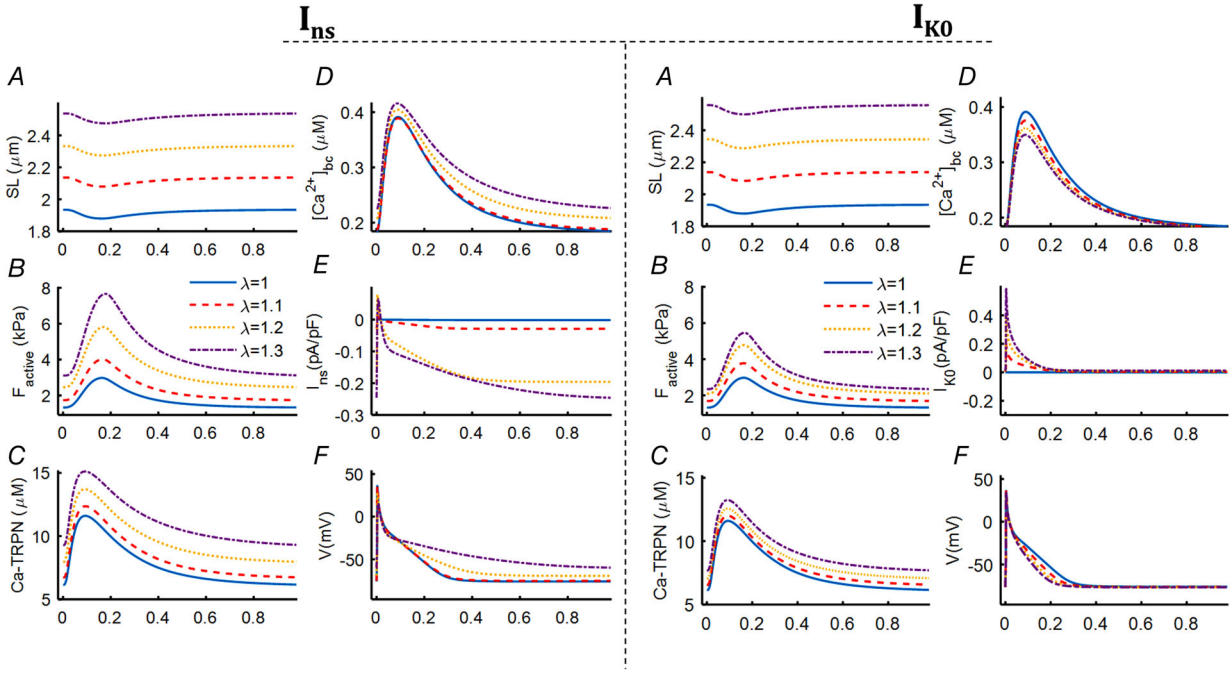

Figure A9. MBS2023 model characteristics for stretch variations using non-selective and selective cations current, I_{ns} (left panels) and I_{K0} (right panels), respectively
Stretch is varied by increasing preload effect, i.e. λ from 1 (blue continuous line), 1.1 (red dashed lines), 1.2 (yellow dashed line), and 1.3 (purple dotted-dashed line). *A*, the increasing length of contractile element (l_{CE}). *B*, active contractile force (F_{active}). *C*, the concentration of Ca^{2+} bound to troponin (TRPN). *D*, Ca^{2+} transient in bulk cytoplasm (bc). *E*, I_{ns} (left) and I_{K0} (right) variation with stretch. *F*, the action potential (AP). [Colour figure can be viewed at wileyonlinelibrary.com]

Effect of increased conductance of I_{ns} current on MBS2023

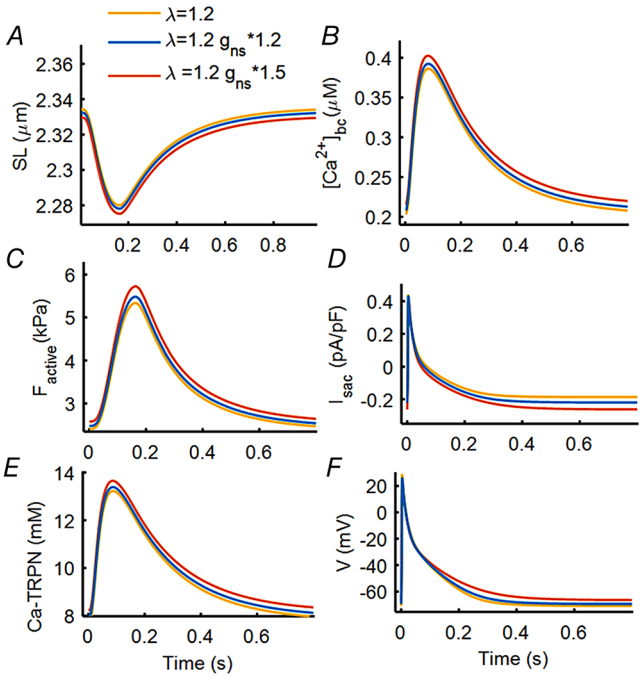

Figure A10. Increased conductance g_{ns} of I_{ns} current for λ = 1.2 response of model MBS2023
Basal state of the model is in yellow, 20% increase in g_{ns} is in blue, and 50% increase in g_{ns} is in red. *A*, length of contractile element (l_{CE}). *B*, F_{active}. *C*, concentration of Ca^{2+} bound to TRPN. *D*, Ca^{2+} transient in the bulk cytosol. *E*, increasing I_{sac} current. *F*, the action potential. [Colour figure can be viewed at wileyonlinelibrary.com]

Appendix 3: Tables data references and model parameters

Table A1. References used for cell capacitances in experimental data for human atrial myocytes

Reference	Mean (pF)	SD	*N*
(Voigt et al., 2012)	114.8	33.2	26
(Wettwer et al., 2004)	101	35	29
(Gulais et al., 2004)	99.4	9.5	16
(Dobrev et al., 2001)	92	65.7	30
(Voigt et al., 2014)	113.6	36	35
(Voigt et al., 2010)	94		
(Dobrev et al., 2002)	84	32.9	68
(Fermini et al., 1992)	73.7	24.3	10
(Fakuade et al., 2021)	95.97	51.1	78
(Wang et al., 1993)	66.1	19.2	34
(Kamkin et al., 2003)	72.4	6.4	14
(Schotten et al., 2002)	72	3	167
(Li et al., 1997)	67	35.4	35
(Van Wagoner et al., 1999)	67.6	26.8	86
(Madsen et al., 2004)	58	7.8	16
(Giles & Imaizumi 1988)	54.3	5.87	5
(Nygren et al., 1998)	51.9	3.5	52
(Wang et al., 1999)	29.6	1.8	

Table A2. Human atrial experimental data used for calibration of contraction parameters in the Electro-mechanical model

Reference	Tissue preparation	Biomarker	Frequency dependent Biomarkers
(Schotten et al., 2002)	Muscle strips obtained from right atrial appendages from patients of mitral valve surgery at 1 Hz, 37°C ($n = 31$)	F_{max}, $rt_{90Factive}$	F_{max}, $rt_{90Factive}$
(Schwinger et al., 1993)	Right atrial trabeculae from patients who underwent aortocoronary bypass operations at 1 Hz, 37°C ($n = 9$)	F_{max}	F_{max}
(Sossalla et al., 2010)	Thin right atrial trabeculae were micro-dissected ($n = 79$)	F_{max}, $ttp_{Factive}$, $rt_{50Factive}$, $rt_{90Factive}$	F_{max}, $ttp_{Factive}$, $rt_{50Factive}$, $rt_{90Factive}$
(L S. Maier et al., 2000)	Muscle strips from right atrial trabeculae obtained from patients undergoing aortocoronary bypass operation at 37°C ($n = 15$)	F_{max}, $TT_{Factive}$, $ttp_{Factive}$, $rt_{50Factive}$, $rt_{90Factive}$, CaT_{max}	F_{max}, CaT_{max}
(Flesch et al., 1997)	Isolated electrically driven human right atrial trabecula from non-failing hearts at 1 Hz, 37°C ($n = 15$)	$ttp_{Factive}$, $rt_{50Factive}$	
(Brixius et al., 1997)	Right atrial tissue from patients having aortocoronary bypass surgery ($n = 19$)	$ttp_{Factive}$, $rt_{50Factive}$, CaT_{max}	
(Schotten et al., 2007)	Muscle strip preparations from atrial trabeculae obtained from right atrial appendages at 1 Hz, 37°C ($n = 14$)	F_{max}	
(Brixius et al., 1999)	Auricular trabeculae were selected from right atrial tissue. Using Fura-2 ratio method for Ca transient and force in muscle strips at 37°C, 1 Hz	F_{max}, F_{min}, $ttp_{Factive}$, $rt_{50Factive}$, CaT_{max}, CaT_{min}, $ttp_{CaT,}$ rt_{50CaT}	F_{max}, F_{min}, $ttp_{Factive}$, $rt_{50Factive}$, CaT_{max}, CaT_{min}, $ttp_{CaT,}$ rt_{50CaT}
(Voigt et al., 2012)	Human atrial myocytes isolated from right atrial appendage at 37°C for 40 myocytes extracted from 20 patients	$CaT_{min,}$ CaT_{sys}, CaT_{amp}, τ	
(Voigt et al., 2014)	Human atrial appendages from 73 patients were isolated at 37°C	$CaT_{min,}$ CaT_{sys}, CaT_{amp}, τ	
(Heijman et al., 2020)	71 out of 149 RA-appendages were subject to cardiomyocytes isolation at 37°C	$CaT_{min,}$ CaT_{sys}, CaT_{amp}, τ	
(Grandi et al., 2011)	Atrial myocytes extracted from right atrial appendages were isolated using enzymatic dissociation at 37°C	$CaT_{min,}$ CaT_{sys}, CaT_{amp}	
(Fakuade et al., 2021)	Myocytes ($n = 78$) were isolated from 38 patients extracted from right atrial appendages	$CaT_{min,}$ CaT_{sys}, CaT_{amp}, τ	

F_{max}: peak tension; F_{min}: diastolic tension; $ttp_{Factive}$: time to F_{max}; $TT_{Factive}$: twitch time; $rt_{50Factive}$, $rt_{90Factive}$: relaxation time at 50% and 90% of F_{max}; CaT_{max}: calcium transient peak; CaT_{min}: calcium transient diastolic; CaT_{amp}: calcium transient amplitude; rt_{50CaT}: relaxation time at 50% of CaT_{max}; ttp_{CaT}: time to CaT_{max}; τ: decay time.

Table A3. Contraction module calibration based on biomarkers from human atrial experimental data

Parameters	Calibrated data	RDQ2020 calibration
Troponin sensitivity (k_{d0}) (mM)	1.4e-3	0.3e-3
Troponin dissociation rate (k_{off}) (s^{-1})	197.6	100
Cooperativity factor (γ) (-)	13.43	12
r_0 (s^{-1})	55.5	134.31
α (-)	22.2	25.184
$\mu_{f_p}^0$ (s^{-1})	13.5	32.653
$\mu_{f_p}^1$ (s^{-1})	0.304	0.778
a_{XB} (kPa)	52.89e3	22.894e3

Table A4. Human atrial *in-vitro* data used for evaluation of action potential biomarkers

Reference	Experimental protocols	Biomarkers	Frequency dependent biomarkers
(Bosch et al., 1999)	Whole cell voltage clamp technique was used to record AP from rod shaped cells of the RA appendages at 36°C	APD_{90}	APD_{90}
(Van Wagoner et al., 1999)	Whole cell patch clamp technique was used to record AP from isolated atrial myocytes at 35°C	APD_{90}, APD_{50}	APD_{90}, APD_{50}
Dobrev et al., 2002	Atrial myocytes were recorded using patch electrodes at 37°C	APD_{90}, APD_{50}, RMP	APD_{90}
(Dawodu et al., 1996)	RA trabeculae were simulated with intracellular microelectrode technique to record APs at 31°C (Type 3 morphology data only were considered)	APD_{90}, APD_{50}, APD_{30}, RMP, dV/dt_{max}, APA	RMP, dV/dt_{max}
(Lagrutta et al., 2006)	Microelectrode technique was used to measure action potential duration from human atrial myocytes at 35°C.	APD_{90}, APD_{50}, RMP, dV/dt_{max}, APA	
(Wang et al., 1990)	Microelectrode technique was used to measure AP characteristics from atrial strips obtained from right atrial appendage at 36°C	RMP, dV/dt_{max}, APA	
(Wettwer et al., 2004)	Microelectrode technique was used in right atrial trabeculae	RMP	
(Dobrev et al., 2001)	Microelectrode technique used to measure the APs from right atrial trabeculae at 37°C	APD_{50}, RMP	
(Workman et al., 2003)	Whole cell patch clamp technique was used to record the APs at 35–37°C	APA	
(Ford et al., 2016)	Sharp microelectrode was used to measure action potentials from small pieces of RAA at 36°C and basal frequency of 1Hz	APD_{90}, APD_{50}, APD_{20}, PLT_{20}, RMP, dV/dt_{max}, APA, ERP	APD_{90}, APD_{50}, APD_{20}, PLT_{20}, RMP, dV/dt_{max}, APA, ERP

Table A5. Modified parameter values in MBS2023

A. Ionic current related parameters			
Parameter	MBS2023	KM2011	Motivation
g_{Na} (nS)	350	$P_{Na} = 0.00182$ nL s^{-1}	Reformulated according to new experimental data as described in (Skibsbye et al., 2016)
g_{CaL} (nS)	14.5	25.3125	To avoid irregular reactivation of I_{CaL} current at the lower frequency of 0.5 Hz
g_{Kur} (nS)	2.35	2.447	To achieve an APD_{50} more inline with the experimental bound as shown in Fig. 4*A*
g_{K1} (nS)	3.44	3.44	-
g_{to} (nS)	8.175	8.175	-
g_{NaCa} (nS)	0.0083	0.0084 (pA/(mmol/L)^4)	As suggested by Skibsbye et al., 2016
g_{Cab} (nS)	0.085	0.0952	
k_{Ca} (mM)	0.6e-3	1e-3	
B. CaMKII related parameters			
$CaMK_0$ (-)	0.05		
K_{mCaM} (mM)	0.0015		
K_{mCaMK} (-)	0.15		
α_{CaMK} (s^{-1})	50		
β_{CaMK} (s^{-1})	0.68		
C. Stretch activated current parameters			
K_{ns} (-)	100		
α_{ns} (-)	30		
g_{ns} (nS)	0.461e-6		
f_{CE} (kPa)	100		
f_{PE} (kPa)	0.006		
f_{SE} (kPa)	2.8		
k_{SE} (μm^{-1})	14.6		
k_{PE} (μm^{-1})	14.6		

References

Barral, Y. S. H., Shuttleworth, J. G., Clerx, M., Whittaker, D. G., Wang, K., Polonchuk, L., Gavaghan, D. J., & Mirams, G. R. (2022). A parameter representing missing charge should be considered when calibrating action potential models. *Frontiers in Physiology*, **13**, 879035.

Bartolucci, C., Forouzandehmehr, M., Severi, S., & Paci, M. (2022). A novel in silico electromechanical model of human ventricular cardiomyocyte. *Frontiers in Physiology*, **13**, 906146.

Bers, D. M., & Grandi, E. (2009). CaMKII regulation of cardiac ion channels. *Journal of Cardiovascular Pharmacology*, **54**(3), 180.

Blatter, L. A. (2017). The intricacies of atrial calcium cycling during excitation-contraction coupling. *Journal of General Physiology*, **149**(9), 857–865.

Blatter, L. A., Kockskämper, J., Sheehan, K. A., Zima, A. V., Hüser, J., & Lipsius, S. L. (2003). Local calcium gradients during excitation–contraction coupling and alternans in atrial myocytes. *The Journal of Physiology*, **546**(1), 19–31.

Bode, F., Katchman, A., Woosley, R. L., & Franz, M. R. (2000). Gadolinium decreases stretch-induced vulnerability to atrial fibrillation. *Circulation*, **101**(18), 2200–2205.

Bokník, P., Unkel, C., Kirchhefer, U., Kleideiter, U., Klein-Wiele, O., Knapp, J., Linck, B., Lüss, H., Ulrich Müller, F., Schmitz, W., & Vahlensieck, U. (1999). Regional expression of phospholamban in the human heart. *Cardiovascular Research*, **43**(1), 67–76.

Bootman, M. D., Higazi, D. R., Coombes, S., & Roderick, H. L. (2006). Calcium signalling during excitation-contraction coupling in mammalian atrial myocytes. *Journal of Cell Science*, **119**(19), 3915–3925.

Bootman, M. D., Smyrnias, I., Thul, R., Coombes, S., & Roderick, H. L. (2011). Atrial cardiomyocyte calcium signalling. *Biochimica et Biophysica Acta (BBA)-Molecular Cell Research*, **1813**(5), 922–934.

Bosch, R. F., Zeng, X., Grammer, J. B., Popovic, K., Mewis, C., & Kühlkamp, V. (1999). Ionic mechanisms of electrical remodeling in human atrial fibrillation. *Cardiovascular Research*, **44**(1), 121–131.

Brixius, K., Pietsch, M., & Schwinger, R. H. G. (1999). The intracellular Ca^{2+}-homeostasis influences the frequency-dependent force-generation in man. *Basic Research in Cardiology*, **94**(3), 152–158.

Brixius, K., Pietsch, M., Hoischen, S., Müller-Ehmsen, J., & Schwinger, R. H. (1997). Effect of inotropic interventions on contraction and Ca^{2+} transients in the human heart. *Journal of Applied Physiology*, **83**(2), 652–660.

Brocklehurst, P., Adeniran, I., Yang, D., Sheng, Y., Zhang, H., & Ye, J. (2015). A 2D electromechanical model of human atrial tissue using the discrete element method. *BioMed Research International*, **2015**, 854953.

Calaghan, S. C., & White, E. (1999). The role of calcium in the response of cardiac muscle to stretch. *Progress in Biophysics and Molecular Biology*, **71**(1), 59–90.

Cherry, E. M., Hastings, H. M., & Evans, S. J. (2008). Dynamics of human atrial cell models: Restitution, memory, and intracellular calcium dynamics in single cells. *Progress in Biophysics and Molecular Biology*, **98**(1), 24–37.

Christ, T., Boknik, P., Wohrl, S., Wettwer, E., Graf, E. M., Bosch, R. F., Knaut, M., Schmitz, W., Ravens, U., & Dobrev, D. (2004). L-type Ca2+ current downregulation in chronic human atrial fibrillation is associated with increased activity of protein phosphatases. *Circulation*, **110**(17), 2651–2657.

Colman, M. A., Aslanidi, O. V., Kharche, S., Boyett, M. R., Garratt, C., Hancox, J. C., & Zhang, H. (2013). Pro-arrhythmogenic effects of atrial fibrillation-induced electrical remodelling: Insights from the three-dimensional virtual human atria. *The Journal of Physiology*, **591**(17), 4249–4272.

Courtemanche, M., Ramirez, R. J., & Nattel, S. (1998). Ionic mechanisms underlying human atrial action potential properties: Insights from a mathematical model. *American Journal of Physiology-Heart and Circulatory Physiology*, **275**(1), H301–H321.

Dawodu, A. A., Monti, F., Iwashiro, K., Schiariti, M., Chiavarelli, R., & Puddu, P. E. (1996). The shape of human atrial action potential accounts for different frequency-related changes in vitro. *International Journal of Cardiology*, **54**(3), 237–249.

Decher, N., Kumar, P., Gonzalez, T., Pirard, B., & Sanguinetti, M. C. (2006). Binding site of a novel Kv1. 5 blocker: a "foot in the door" against atrial fibrillation. *Molecular Pharmacology*, **70**(4), 1204–1211.

Díaz, M. E., O'neill, S. C., & Eisner, D. A. (2004). Sarcoplasmic reticulum calcium content fluctuation is the key to cardiac alternans. *Circulation Research*, **94**(5), 650–656.

Dobrev, D., Wettwer, E., Kortner, A., Knaut, M., Schüler, S., & Ravens, U. (2002). Human inward rectifier potassium channels in chronic and postoperative atrial fibrillation. *Cardiovascular Research*, **54**(2), 397–404.

Dobrev, D., Graf, E., Wettwer, E., Himmel, H. M., Hala, O., Doerfel, C., Christ, T., Schuler, S., & Ravens, U. (2001). Molecular basis of downregulation of G-protein–coupled inward rectifying K^+ current ($I_{K,\,ACh}$) in chronic human atrial fibrillation: Decrease in Girk4 mRNA correlates with reduced $I_{K,\,ACh}$ and muscarinic receptor–mediated shortening of action potentials. *Circulation*, **104**(21), 2551–2557.

Dössel, O., Krueger, M. W., Weber, F. M., Wilhelms, M., & Seemann, G. (2012). Computational modeling of the human atrial anatomy and electrophysiology. *Medical & Biological Engineering & Computing*, **50**(8), 773–799.

Fabiato, A. (1983). Calcium-induced release of calcium from the cardiac sarcoplasmic reticulum. *American Journal of Physiology-Cell Physiology*, **245**(1), C1–C14.

Fakuade, F. E., Steckmeister, V., Seibertz, F., Gronwald, J., Kestel, S., Menzel, J., Pronto, J. R. D., Taha, K., Haghighi, F., Kensah, G., & Pearman, C. M. (2021). Altered atrial cytosolic calcium handling contributes to the development of postoperative atrial fibrillation. *Cardiovascular Research*, **117**(7), 1790–1801.

Feng, J., Yue, L., Wang, Z., & Nattel, S. (1998). Ionic mechanisms of regional action potential heterogeneity in the canine right atrium. *Circulation Research*, **83**(5), 541–551.

Fermini, B. E. R. N. A. R. D., Wang, Z. H. I. G. U. O., Duan, D. A. Y. U. E., & Nattel, S. T. A. N. L. E. Y. (1992). Differences in rate dependence of transient outward current in rabbit and human atrium. *American Journal of Physiology-Heart and Circulatory Physiology*, **263**(6), H1747–H1754.

Flesch, M., Kilter, H., Cremers, B., Lenz, O., Südkamp, M., Kuhn-Regnier, F., & Böhm, M. (1997). Acute effects of nitric oxide and cyclic GMP on human myocardial contractility. *Journal of Pharmacology and Experimental Therapeutics*, **281**(3), 1340–1349.

Ford, J., Milnes, J., El Haou, S., Wettwer, E., Loose, S., Matschke, K., Tyl, B., Round, P., & Ravens, U. (2016). The positive frequency-dependent electrophysiological effects of the I_{Kur} inhibitor XEN-D0103 are desirable for the treatment of atrial fibrillation. *Heart Rhythm*, **13**(2), 555–564.

Forouzandehmehr, M., Koivumäki, J. T., Hyttinen, J., & Paci, M. (2021). A mathematical model of hiPSC cardiomyocytes electromechanics. *Physiological Reports*, **9**(22), e15124.

Giles, W. R., & Imaizumi, Y. (1988). Comparison of potassium currents in rabbit atrial and ventricular cells. *The Journal of Physiology*, **405**(1), 123–145.

Grandi, E., Pandit, S. V., Voigt, N., Workman, A. J., Dobrev, D., Jalife, J., & Bers, D. M. (2011). Human atrial action potential and Ca2+ model: sinus rhythm and chronic atrial fibrillation. *Circulation Research*, **109**(9), 1055–1066.

Harrison, S. M., & Boyett, M. R. (1995). The role of the Na (+)-Ca^{2+} exchanger in the rate-dependent increase in contraction in guinea-pig ventricular myocytes. *The Journal of Physiology*, **482**(3), 555–566.

Hatem, S. N., Benardeau, A., Rucker-Martin, C., Marty, I., de Chamisso, P., Villaz, M., & Mercadier, J. J. (1997). Different compartments of sarcoplasmic reticulum participate in the excitation-contraction coupling process in human atrial myocytes. *Circulation Research*, **80**(3), 345–353.

Heijman, J., Muna, A. P., Veleva, T., Molina, C. E., Sutanto, H., Tekook, M., Wang, Q., Abu-Taha, I. H., Gorka, M., Künzel, S., & El-Armouche, A. (2020). Atrial myocyte NLRP3/CaMKII nexus forms a substrate for postoperative atrial fibrillation. *Circulation Research*, **127**(8), 1036–1055.

Heijman, J., Sutanto, H., Crijns, H. J., Nattel, S., & Trayanova, N. A. (2021). Computational models of atrial fibrillation: Achievements, challenges, and perspectives for improving clinical care. *Cardiovascular Research*, **117**(7), 1682–1699.

Hove-Madsen, L., Llach, A., Bayes-Genís, A., Roura, S., Font, E. R., Arís, A., & Cinca, J. (2004). Atrial fibrillation is associated with increased spontaneous calcium release from the sarcoplasmic reticulum in human atrial myocytes. *Circulation*, **110**(11), 1358–1363.

Hüser, J., Lipsius, S. L., & Blatter, L. A. (1996). Calcium gradients during excitation-contraction coupling in cat atrial myocytes. *The Journal of Physiology*, **494**(3), 641–651.

Hüser, J., Wang, Y. G., Sheehan, K. A., Cifuentes, F., Lipsius, S. L., & Blatter, L. A. (2000). Functional coupling between glycolysis and excitation—contraction coupling underlies alternans in cat heart cells. *The Journal of Physiology*, **524**(3), 795–806.

Jakob, D., Klesen, A., Allegrini, B., Darkow, E., Aria, D., Emig, R., Chica, A. S., Rog-Zielinska, E. A., Guth, T., Beyersdorf, F., & Kari, F. A. (2021). Piezo1 and BKCa channels in human atrial fibroblasts: Interplay and remodelling in atrial fibrillation. *Journal of Molecular and Cellular Cardiology*, **158**, 49–62.

Ji, Y. C., Gray R. A., & Fenton . H. (2015). Implementation of contraction to electrophysiological ventricular myocyte models, and their quantitative characterization via post-extrasystolic potentiation. *PLoS ONE*, **10**(8), e0135699.

Kamkin, A., Kiseleva, I., Wagner, K. D., Bohm, J., Theres, H., Günther, J., & Scholz, H. (2003). Characterization of stretch-activated ion currents in isolated atrial myocytes from human hearts. *Pflügers Archiv*, **446**(3), 339–346.

Kim, D. (1993). Novel cation-selective mechanosensitive ion channel in the atrial cell membrane. *Circulation Research*, **72**(1), 225–231.

Kohl, P., & Sachs, F. (2001). Mechanoelectric feedback in cardiac cells. Philosophical Transactions of the Royal Society of London. Series A: *Mathematical, Physical and Engineering Sciences*, **359**(1783), 1173–1185.

Koivumäki, J. T., Korhonen, T., & Tavi, P. (2011). Impact of sarcoplasmic reticulum calcium release on calcium dynamics and action potential morphology in human atrial myocytes: A computational study. *PLoS Computational Biology*, **7**(1), e1001067.

Koivumäki, J. T., Seemann, G., Maleckar, M. M., & Tavi, P. (2014). In silico screening of the key cellular remodeling targets in chronic atrial fibrillation. *PLoS Computational Biology*, **10**(5), e1003620.

Koivumäki, J. T., Takalo, J., Korhonen, T., Tavi, P., & Weckström, M. (2009). Modelling sarcoplasmic reticulum calcium ATPase and its regulation in cardiac myocytes. *Philosophical Transactions of the Royal Society A: Mathematical, Physical and Engineering Sciences*, **367**(1896), 2181–2202.

Kuijpers, N. H., Eikelder ten, H. M., Bovendeerd, P. H., Verheule, S., Arts, T., & Hilbers, P. A. (2007). Mechano-electric feedback leads to conduction slowing and block in acutely dilated atria: A modeling study of cardiac electromechanics. *American Journal of Physiology-Heart and Circulatory Physiology*, **292**(6), H2832–H2853.

Lagrutta, A., Wang, J., Fermini, B., & Salata, J. J. (2006). Novel, potent inhibitors of human Kv1. 5 K+ channels and ultrarapidly activating delayed rectifier potassium current. *Journal of Pharmacology and Experimental Therapeutics*, **317**(3), 1054–1063.

Land, S., & Niederer, S. A. (2018). Influence of atrial contraction dynamics on cardiac function. *International Journal for Numerical Methods in Biomedical Engineering*, **34**(3), e2931.

Lebek, S., Plößl, A., Baier, M., Mustroph, J., Tarnowski, D., Lücht, C. M., Schopka, S., Flörchinger, B., Schmid, C., Zausig, Y., & Pagratis, N. (2018). The novel CaMKII inhibitor GS-680 reduces diastolic SR Ca leak and prevents CaMKII-dependent pro-arrhythmic activity. *Journal of Molecular and Cellular Cardiology*, **118**, 159–168.

Lee, Y., Cansız, B., & Kaliske, M. (2022). Computational modelling of mechano-electric feedback and its arrhythmogenic effects in human ventricular models. *Computer Methods in Biomechanics and Biomedical Engineering*, **25**(15), 1767–1783.

Li, G. R., & Nattel, S. T. A. N. L. E. Y. (1997). Properties of human atrial ICa at physiological temperatures and relevance to action potential. *American Journal of Physiology-Heart and Circulatory Physiology*, **272**(1), H227–H235.

Li, G. R., Wang, H. B., Qin, G. W., Jin, M. W., Tang, Q., Sun, H. Y., Du, X. L., Deng, X. L., Zhang, X. H., Chen, J. B., & Chen, L. (2008). Acacetin, a natural flavone, selectively inhibits human atrial repolarization potassium currents and prevents atrial fibrillation in dogs. *Circulation*, **117**(19), 2449–2457.

Llach, A., Molina, C. E., Fernandes, J., Padró, J., Cinca, J., & Hove-Madsen, L. (2011). Sarcoplasmic reticulum and L-type Ca^{2+} channel activity regulate the beat-to-beat stability of calcium handling in human atrial myocytes. *The Journal of Physiology*, **589**(13), 3247–3262.

Lookin, O., Butova, X., & Protsenko, Y. (2021). The role of pacing rate in the modulation of mechano-induced immediate and delayed changes in the force and Ca-transient of cardiac muscle. *Progress in Biophysics and Molecular Biology*, **159**, 34–45.

Maier, L. S., Barckhausen, P., Weisser, J., Aleksic, I., Baryalei, M., & Pieske, B. (2000). Ca^{2+} handling in isolated human atrial myocardium. *American Journal of Physiology-Heart and Circulatory Physiology*, **279**(3), H952–H958.

Margara, F., Wang, Z. J., Levrero-Florencio, F., Santiago, A., Vázquez, M., Bueno-Orovio, A., & Rodriguez, B. (2021). In-silico human electro-mechanical ventricular modelling and simulation for drug-induced pro-arrhythmia and inotropic risk assessment. *Progress in Biophysics and Molecular Biology*, **159**, 58–74.

Mazhar, F., Regazzoni, F., Bartolucci, C., Corsi, C., Dedè, L., Quarteroni, A., & Severi, S. (2021), Electro-mechanical coupling in human atrial cardiomyocytes: Model development and analysis of inotropic interventions. In *2021 Computing in Cardiology (CinC)* (Vol., 48, 1–4). IEEE.

Michailova, A., DelPrincipe, F., Egger, M., & Niggli, E. (2002). Spatiotemporal features of Ca^{2+} buffering and diffusion in atrial cardiac myocytes with inhibited sarcoplasmic reticulum. *Biophysical Journal*, **83**(6), 3134–3151.

Morano, I., Arndt, H., Gärtner, C., & Rüegg, J. C. (1988). Skinned fibers of human atrium and ventricle: Myosin isoenzymes and contractility. *Circulation Research*, **62**(3), 632–639.

Morotti, S., Liu, C., Hegyi, B., Ni, H., Fogli Iseppe, A., Wang, L., Pritoni, M., Ripplinger, C. M., Bers, D. M., Edwards, A. G., & Grandi, E. (2021). Quantitative cross-species translators of cardiac myocyte electrophysiology: Model training, experimental validation, and applications. *Science Advances*, **7**(47), eabg0927.

Narayan, S. M., Franz, M. R., Clopton, P., Pruvot, E. J., & Krummen, D. E. (2011). Repolarization alternans reveals vulnerability to human atrial fibrillation. *Circulation*, **123**(25), 2922–2930.

Narolska, N. A., Van Loon, R. B., Boontje, N. M., Zaremba, R., Penas, S. E., Russell, J., Spiegelenberg, S. R., Huybregts, M. A. J. M., Visser, F. C., de Jong, J. W., & van der Velden, J. (2005). Myocardial contraction is 5-fold more economical in ventricular than in atrial human tissue. *Cardiovascular Research*, **65**(1), 221–229.

Nazir, S. A., & Lab, M. J. (1996). Mechanoelectric feedback in the atrium of the isolated guinea-pig heart. *Cardiovascular Research*, **32**(1), 112–119.

Neef, S., Dybkova, N., Sossalla, S., Ort, K. R., Fluschnik, N., Neumann, K., Seipelt, R., Schöndube, F. A., Hasenfuss, G., & Maier, L. S. (2010). CaMKII-dependent diastolic SR Ca2+ leak and elevated diastolic Ca2+ levels in right atrial myocardium of patients with atrial fibrillation. *Circulation Research*, **106**(6), 1134–1144.

Neves, J. S., Leite-Moreira, A. M., Neiva-Sousa, M., Almeida-Coelho, J., Castro-Ferreira, R., & Leite-Moreira, A. F. (2016). Acute myocardial response to stretch: What we (don't) know. *Frontiers in Physiology*, **6**, 408.

Ni, H., Morotti, S., Zhang, X., Dobrev, D., & Grandi, E. (2023). Integrative human atrial modeling unravels interactive PKA and CaMKII signaling as key determinant of atrial arrhythmogenesis. *Cardiovascular Research*. https://doi.org/10.1093/cvr/cvad118

Niederer, S. A., & Smith, N. P. (2007). A mathematical model of the slow force response to stretch in rat ventricular myocytes. *Biophysical Journal*, **92**(11), 4030–4044.

Niederer, S. A., Campbell, K. S., & Campbell, S. G. (2019). A short history of the development of mathematical models of cardiac mechanics. *Journal of Molecular and Cellular Cardiology*, **127**, 11–19.

Nygren, A., Fiset, C., Firek, L., Clark, J. W., Lindblad, D. S., Clark, R. B., & Giles, W. R. (1998). Mathematical model of an adult human atrial cell: The role of K+ currents in repolarization. *Circulation Research*, **82**(1), 63–81.

O'Hara, T., Virág, L., Varró, A., & Rudy, Y. (2011). Simulation of the undiseased human cardiac ventricular action potential: model formulation and experimental validation. *PLoS Computational Biology*, **7**(5), e1002061.

Peyronnet, R., Nerbonne, J. M., & Kohl, P. (2016). Cardiac mechano-gated ion channels and arrhythmias. *Circulation Research*, **118**(2), 311–329.

Pfeiffer, E. R., Tangney, J. R., Omens, J. H., & McCulloch, A. D. (2014). Biomechanics of cardiac electromechanical coupling and mechanoelectric feedback. *Journal of Biomechanical Engineering*, **136**(2), 021007.

Picht, E., DeSantiago, J., Blatter, L. A., & Bers, D. M. (2006). Cardiac alternans do not rely on diastolic sarcoplasmic reticulum calcium content fluctuations. *Circulation Research*, **99**(7), 740–748.

Piroddi, N., Belus, A., Scellini, B., Tesi, C., Giunti, G., Cerbai, E., Mugelli, A., & Poggesi, C. (2007). Tension generation and relaxation in single myofibrils from human atrial and ventricular myocardium. *Pflügers Archiv-European Journal of Physiology*, **454**(1), 63–73.

Quinn, T. A., & Kohl, P. (2021). Cardiac mechano-electric coupling: acute effects of mechanical stimulation on heart rate and rhythm. *Physiological Reviews*, **101**(1), 37–92.

Ravelli, F., Masè, M., Del Greco, M., Marini, M., & Disertori, M. (2011). Acute atrial dilatation slows conduction and increases AF vulnerability in the human atrium. *Journal of Cardiovascular Electrophysiology*, **22**(4), 394–401.

Ravens, U. (2003). Mechano-electric feedback and arrhythmias. *Progress in Biophysics and Molecular Biology*, **82**(1–3), 255–266.

Regazzoni, F., Dedè, L., & Quarteroni, A. (2020). Biophysically detailed mathematical models of multiscale cardiac active mechanics. *PLoS Computational Biology*, **16**(10), e1008294.

Regazzoni, F., Dedè, L., & Quarteroni, A. (2021). Active force generation in cardiac muscle cells: Mathematical modeling and numerical simulation of the actin-myosin interaction. *Vietnam Journal of Mathematics*, **49**(1), 87–118.

Reiser, P. J., Portman, M. A., Ning, X. H., & Moravec, C. S. (2001). Human cardiac myosin heavy chain isoforms in fetal and failing adult atria and ventricles. *American Journal of Physiology-Heart and Circulatory Physiology*, **280**(4), H1814–H1820.

Rice, J. J., Winslow, R. L., & Hunter, W. C. (1999). Comparison of putative cooperative mechanisms in cardiac muscle: Length dependence and dynamic responses. *American Journal of Physiology-Heart and Circulatory Physiology*, **276**(5), H1734–H1754.

Richards, M. A., Clarke, J. D., Saravanan, P., Voigt, N., Dobrev, D., Eisner, D. A., Trafford, A. W., & Dibb, K. M. (2011). Transverse tubules are a common feature in large mammalian atrial myocytes including human. *American Journal of Physiology-Heart and Circulatory Physiology*, **301**(5), H1996–H2005.

Robertson, S. P., Johnson J. D., & Potter J. D. (1981). The time-course of Ca^{2+} exchange with calmodulin, troponin, parvalbumin, and myosin in response to transient increases in Ca^{2+}. *Biophysical Journal*, **34**(3), 559–569.

Sadredini, M., Haugsten Hansen, M., Frisk, M., Louch, W. E., Lehnart, S. E., Sjaastad, I., & Stokke, M. K. (2021). CaMKII inhibition has dual effects on spontaneous Ca^{2+} release and Ca^{2+} alternans in ventricular cardiomyocytes from mice with a gain-of-function RyR2 mutation. *American Journal of Physiology-Heart and Circulatory Physiology*, **321**(2), H446–H460.

Schotten, U., de Haan, S., Verheule, S., Harks, E. G., Frechen, D., Bodewig, E., Greiser, M., Ram, R., Maessen, J., Kelm, M., & Allessie, M. (2007). Blockade of atrial-specific K+-currents increases atrial but not ventricular contractility by enhancing reverse mode Na+/Ca^{2+}-exchange. *Cardiovascular Research*, **73**(1), 37–47.

Schotten, U., Greiser, M., Benke, D., Buerkel, K., Ehrenteidt, B., Stellbrink, C., Vazquez-Jimenez, J. F., Schoendube, F., Hanrath, P., & Allessie, M. (2002). Atrial fibrillation-induced atrial contractile dysfunction: A tachycardiomyopathy of a different sort. *Cardiovascular Research*, **53**(1), 192–201.

Schwinger, R. H., Böhm, M., Koch, A., Uhlmann, R., Überfuhr, P., Kreuzer, E., Reichart, B., & Erdmann, E. (1993). Force-frequency-relation in human atrial and ventricular myocardium. In *Cellular Function and Metabolism* (73–78). Springer, Boston, MA.

Shannon, T. R., Ginsburg, K. S., & Bers, D. M. (2000). Reverse mode of the sarcoplasmic reticulum calcium pump and load-dependent cytosolic calcium decline in voltage-clamped cardiac ventricular myocytes. *Biophysical Journal*, **78**(1), 322–333.

Shkryl, V. M., Maxwell, J. T., Domeier, T. L., & Blatter, L. A. (2012). Refractoriness of sarcoplasmic reticulum Ca^{2+} release determines Ca^{2+} alternans in atrial myocytes. *American Journal of Physiology-Heart and Circulatory Physiology*, **302**(11), H2310–H2320.

Skibsbye, L., Jespersen, T., Christ, T., Maleckar, M. M., van den Brink, J., Tavi, P., & Koivumäki, J. T. (2016). Refractoriness in human atria: Time and voltage dependence of sodium channel availability. *Journal of Molecular and Cellular Cardiology*, **101**, 26–34.

Smith, G. L., & Eisner, D. A. (2019). Calcium buffering in the heart in health and disease. *Circulation*, **139**(20), 2358–2371.

Solovyova, O., Katsnelson, L., Guriev, S., Nikitina, L., Protsenko, Y., Routkevitch, S., & Markhasin, V. (2002). Mechanical inhomogeneity of myocardium studied in parallel and serial cardiac muscle duplexes: Experiments and models. *Chaos, Solitons and Fractals*, **13**(8), 1685–1711.

Soltis, A. R., & Saucerman, J. J. (2010). Synergy between CaMKII substrates and β-adrenergic signaling in regulation of cardiac myocyte Ca^{2+} handling. *Biophysical Journal*, **99**(7), 2038–2047.

Sossalla, S., Kallmeyer, B., Wagner, S., Mazur, M., Maurer, U., Toischer, K., Schmitto, J. D., Seipelt, R., Schöndube, F. A., Hasenfuss, G., & Belardinelli, L. (2010). Altered Na+ currents in atrial fibrillation: Effects of ranolazine on arrhythmias and contractility in human atrial myocardium. *Journal of the American College of Cardiology*, **55**(21), 2330–2342.

Stern, M. D., Song, L. S., Cheng, H., Sham, J. S., Yang, H. T., Boheler, K. R., & Ríos, E. (1999). Local control models of cardiac excitation–contraction coupling: A possible role for allosteric interactions between ryanodine receptors. *The Journal of General Physiology*, **113**(3), 469–489.

Sutanto, H., & Heijman, J. (2022). Integrative computational modeling of cardiomyocyte calcium handling and cardiac arrhythmias: Current status and future challenges. *Cells*, **11**(7), 1090.

Sutanto, H., Lyon, A., Lumens, J., Schotten, U., Dobrev, D., & Heijman, J. (2020). Cardiomyocyte calcium handling in health and disease: Insights from in vitro and in silico studies. *Progress in Biophysics and Molecular Biology*, **157**, 54–75.

Taggart, P., & Sutton, P. M. (1999). Cardiac mechano-electric feedback in man: Clinical relevance. *Progress in Biophysics and Molecular Biology*, **71**(1), 139–154.

Tanaami, T., Ishida, H., Seguchi, H., Hirota, Y., Kadono, T., Genka, C., Nakazawa, H., & Barry, W. H. (2005). Difference in propagation of Ca^{2+} release in atrial and ventricular myocytes. *The Japanese Journal of Physiology*, **55**(2), 81–91.

Tavi, P., Han, C., & Weckström, M. (1998). Mechanisms of stretch-induced changes in [Ca^{2+}]i in rat atrial myocytes: Role of increased troponin C affinity and stretch-activated ion channels. *Circulation Research*, **83**(11), 1165–1177.

Tavi, P., Laine, M., & Weckström, M. (1996). Effect of gadolinium on stretch-induced changes in contraction and intracellularly recorded action-and afterpotentials of rat isolated atrium. *British Journal of Pharmacology*, **118**(2), 407–413.

Tessier, S., Karczewski, P., Krause, E. G., Pansard, Y., Acar, C., Lang-Lazdunski, M., Mercadier, J. J., & Hatem, S. N. (1999). Regulation of the transient outward K+ current by Ca^{2+}/calmodulin-dependent protein kinases II in human atrial myocytes. *Circulation Research*, **85**(9), 810–819.

Timmermann, V., Dejgaard, L. A., Haugaa, K. H., Edwards, A. G., Sundnes, J., McCulloch, A. D., & Wall, S. T. (2017). An integrative appraisal of mechano-electric feedback mechanisms in the heart. *Progress in Biophysics and Molecular Biology*, **130**(Pt B), 404–417.

Tsai, C. T., Chiang, F. T., Tseng, C. D., Yu, C. C., Wang, Y. C., Lai, L. P., Hwang, J. J., & Lin, J. L. (2011). Mechanical stretch of atrial myocyte monolayer decreases sarcoplasmic reticulum calcium adenosine triphosphatase expression and increases susceptibility to repolarization alternans. *Journal of the American College of Cardiology*, **58**(20), 2106–2115.

Trayanova, N. A., & Rice, J. J. (2011). Cardiac electromechanical models: From cell to organ. *Frontiers in Physiology*, **2**, 43.

Vagos, M., van Herck, I. G., Sundnes, J., Arevalo, H. J., Edwards, A. G., & Koivumäki, J. T. (2018). Computational modeling of electrophysiology and pharmacotherapy of atrial fibrillation: Recent advances and future challenges. *Frontiers in Physiology*, **9**, 1221.

Van Wagoner, D. R., Pond, A. L., Lamorgese, M., Rossie, S. S., McCarthy, P. M., & Nerbonne, J. M. (1999). Atrial L-type Ca2+ currents and human atrial fibrillation. *Circulation Research*, **85**(5), 428–436.

Varela, M., Roy, A., & Lee, J. (2021). A survey of pathways for mechano-electric coupling in the Atria. *Progress in Biophysics and Molecular Biology*, **159**, 136–145.

Verdonck, F., Mubagwa, K., & Sipido, K. R. (2004). [Na^+] in the subsarcolemmal 'fuzzy'space and modulation of $[Ca^{2+}]_i$ and contraction in cardiac myocytes. *Cell Calcium*, **35**(6), 603–612.

Voigt, N., Heijman, J., Wang, Q., Chiang, D. Y., Li, N., Karck, M., Wehrens, X. H., Nattel, S., & Dobrev, D. (2014). Cellular and molecular mechanisms of atrial arrhythmogenesis in patients with paroxysmal atrial fibrillation. *Circulation*, **129**(2), 145–156.

Voigt, N., Li, N., Wang, Q., Wang, W., Trafford, A. W., Abu-Taha, I., Sun, Q., Wieland, T., Ravens, U., Nattel, S., & Wehrens, X. H. (2012). Enhanced sarcoplasmic reticulum Ca^{2+} leak and increased Na^+-Ca^{2+} exchanger function underlie delayed afterdepolarizations in patients with chronic atrial fibrillation. *Circulation*, **125**(17), 2059–2070.

Voigt, N., Trafford, A. W., Wang, Q., Wehrens, X., Ravens, U., & Dobrev, D. (2010). Sarcoplasmic reticulum calcium leak and enhanced NCX increase occurrence of delayed afterdepolarisations in atrial myocytes from patients with chronic atrial fibrillation.

Walden, A. P., Dibb, K. M., & Trafford, A. W. (2009). Differences in intracellular calcium homeostasis between atrial and ventricular myocytes. *Journal of Molecular and Cellular Cardiology*, **46**(4), 463–473.

Wang, G. X., Schmied, R., Ebner, F., & Korth, M. (1993). Intracellular sodium activity and its regulation in guinea-pig atrial myocardium. *The Journal of Physiology*, **465**(1), 73–84.

Wang, Z. G., Pelletier, L. C., Talajic, M., & Nattel, S. (1990). Effects of flecainide and quinidine on human atrial action potentials. Role of rate-dependence and comparison with guinea pig, rabbit, and dog tissues. *Circulation*, **82**(1), 274–283.

Wang, Z., Feng, J., Shi, H., Pond, A., Nerbonne, J. M., & Nattel, S. (1999). Potential molecular basis of different physiological properties of the transient outward K+ current in rabbit and human atrial myocytes. *Circulation Research*, **84**(5), 551–561.

Wettwer, E., Hála, O., Christ, T., Heubach, J. F., Dobrev, D., Knaut, M., Varró, A., & Ravens, U. (2004). Role of I Kur in controlling action potential shape and contractility in the human atrium: Influence of chronic atrial fibrillation. *Circulation*, **110**(16), 2299–2306.

Wilhelms, M., Hettmann, H., Maleckar, M. M., Koivumäki, J. T., Dössel, O., & Seemann, G. (2013). Benchmarking electrophysiological models of human atrial myocytes. *Frontiers in Physiology*, **3**, 487.

Workman, A. J., Kane, K. A., & Rankin, A. C. (2003). Characterisation of the Na, K pump current in atrial cells from patients with and without chronic atrial fibrillation. *Cardiovascular Research*, **59**(3), 593–602.

Xie, L. H., Sato, D., Garfinkel, A., Qu, Z., & Weiss, J. N. (2008). Intracellular Ca alternans: Coordinated regulation by sarcoplasmic reticulum release, uptake, and leak. *Biophysical Journal*, **95**(6), 3100–3110.

Zhan, H., & Xia, L. (2013). Excitation-contraction coupling between human atrial myocytes with fibroblasts and stretch activated channel current: A simulation study. *Computational and Mathematical Methods in Medicine*, **2013**, 238676.

Zhan, H., Zhang, J., Jiao, A., & Wang, Q. (2019). Stretch-activated current in human atrial myocytes and Na+ current and mechano-gated channels' current in myofibroblasts alter myocyte mechanical behavior: A computational study. *Biomedical Engineering Online*, **18**(1), 1–15.

Zhang, S., Li, Q., Zhou, L., Wang, K., & Zhang, H. (2015), September. Development of a novel Markov chain model for oxidative-dependent CaMKIIδ activation. In *2015 Computing in Cardiology Conference (CinC)* (pp. 881–884). IEEE.

Zhao, N., Li, Q., Sui, H., & Zhang, H. (2020). Role of oxidation-dependent CaMKII activation in the genesis of abnormal action potentials in atrial cardiomyocytes: A simulation study. *BioMed Research International*, **2020**, 1597012.

Zile, M. A., & Trayanova, N. A. (2018). Increased thin filament activation enhances alternans in human chronic atrial fibrillation. *American Journal of Physiology-Heart and Circulatory Physiology*, **315**(5), H1453–H1462.

Additional information

Data availability statement

The original contributions presented in the study are included in the article; further inquiries can be directed to the corresponding author.

Competing interests

The authors declare that the research was conducted in the absence of any commercial or financial relationships that could be construed as a potential conflict of interest.

Author contributions

S.S. was responsible for the study conception. F.M. and S.S. were responsible for the study design. FM was responsible for simulations. F.M., C.B. and S.S. were responsible for data analysis. F.M., C.B., M.P. and S.S. were responsible for data interpretation. F.M., C.B. and S.S. were responsible for writing the manuscript. F.M., C.B., F.R., M.P., L.D., A.Q., C.C. and S.S. were responsible for the final approval of the manuscript submitted for publication. All authors agree to be accountable for all aspects of the work. All persons designated as authors qualify for authorship, and all those who qualify for authorship are listed.

Funding

This work was supported by the Italian Ministry of University and Research (MIUR) within the PRIN 2017 project 'Modelling

the heart across the scales: from cardiac cells to the whole organ' Grant Registration number (2017AXL54F). C.B. and S.S. have received funding from the European Union - NextGenerationEU through the Italian Ministry of University and Research under PNRR - M4C2-I1.3 Project PR_00000019 "HEAL ITALIA" to S.S. CUP J33C22002920006. The views and opnions expressed are those of the authors only and do not necessarily reflect those of the European Union or the European Comission. Neither the European Union nor the European Comission can be held responsible for them. F.R. and L.D. are the members of the INdAM group GNCS (National Group for the Scientific Computing).

Acknowledgements

The authors thank Jussi Koivumäki for sharing the code of his model and for useful advice about the initial choices on the structure of the AP model.

Keywords

Ca^{2+}-handling, cardiomechanics, computational modelling, contractility, coupling, human atrial cells, rate adaptation, stretch activated currents

Supporting information

Additional supporting information can be found online in the Supporting Information section at the end of the HTML view of the article. Supporting information files available:

Statistical Summary Document
Peer Review History